Alma Mater Studiorum – Università di Bologna

Dipartimento di Fisica e Astronomia
Corso di Laurea magistrale in Astrofisica e Cosmologia

Gas rotation and dark matter halo shape in cool-core clusters of galaxies

Tesi di laurea

Presentata da:
Tommaso Bartalesi

Relatore:
Prof. Carlo Nipoti

Correlatore:
Dott. Stefano Ettori

Anno accademico 2021-2022

Abstract

In the context of the study of galaxy clusters it is usual to assume that the intracluster medium (ICM) is static into a spherical dark matter (DM) halo. However, there are observational (and theoretical) pieces of evidence that the estimates of mass under the assumption of hydrostatic equilibrium are biased low with respect to the "true" mass as traced, e.g., by gravitational lensing. Moreover, on the basis of the cosmological N-body DM-only and hydrodynamical simulations there is a clear evidence that the assumptions of spherically symmetric halo and of hydrostatic equilibrium of the ICM are not always justified. One way to detect these departures from hydrostatic equilibrium in the ICM is through the detection of bulk motions. However, the low energy resolution of available X-ray instruments does not allow for this detection via the Doppler shift of the emission lines centroids in the X-ray spectra. In this work, we build polytropic models of the ICM in cool-core clusters: we explore different kinematic conditions of the ICM (in particular, the rotation) and/or different shapes of halos, while preserving the predicted regularity of internal structure of halos (the Navarro-Frenk-White profile and mass-concentration relation) and the universality of observed thermodynamic profiles of the ICM. Then, from these models, we reconstruct the main photometric and spectroscopic observables to test the current photometric upper limits on the rotation speed and to probe the future perspectives via mock observations with the spectrometer RESOLVE on board of XRISM. We conclude that our models predict rotation of 400-500 km/s that do not violate the available observational proxies (*i.e.* the thermodynamic profiles, shape of iso-surface brightness contours and broadening of X-ray emitting lines), leaving some room in real clusters for possible rotation within 500 km/s, which could be detected with future facilities.

Contents

Riassunto della tesi

Le ossservazioni in banda X degli ammasi di galassie sono spesso interpretate assumendo che il mezzo intracluster (ICM) sia statico e l'alone di materia oscura (DM) sferico. Tuttavia, entrambe le assunzioni non sono sempre giustificate: da un lato, le simulazioni numeriche con sola DM, che modellano la crescita delle perturbazioni nel contesto cosmologico, hanno mostrato la presenza di schiacciamento significativo nella maggioranza degli aloni (e.g. Allgood et al. 2006); dall'altro lato, le simulazioni idrodinamiche hanno rivelato la presenza di rotazione significativa dell'ICM (e.g. Nagai et al. 2013). Il miglior metodo per rilevare la rotazione negli ammassi è lo spostamento delle righe di emissione negli spettri X, ma gli spettrografi X attualmente disponibili non raggiungono delle risoluzioni in energia sufficienti a misurare tale spostamento o a escluderlo; tuttavia, tali misurazioni potrebbero essere possibili con gli strumenti X di nuova generazione [ad esempio, RESOLVE su XRISM (`https://xrism.isas.jaxa.jp/en/`)]. Al tempo stesso, la massa degli ammassi di galassie stimata dalle osservazioni X dell'ICM sotto l'assunzione di equilibrio idrostatico risulta sottostimata di $\lesssim 30\%$ (e.g. Pratt et al. 2019) se confrontata alla massa "vera" tracciata, e.g., dal lensing gravitazionale. Tale differenza può essere spiegata dalla presenza della rotazione dell'ICM, che altera l'assunzione di equilibrio idrostatico (vedi Fang et al. 2009). Inoltre, la rotazione dell'ICM combinata con deboli campi magnetici dà vita a modi instabili del plasma (Nipoti et al. 2015), in grado di riscaldare l'ICM tramite dissipazione turbolenta e, quindi, di contribuire a fermare i cooling flows negli ammassi.
La prima parte di questa tesi propone modelli realistici di tipici ammassi cool-core massivi, che includono anche la rotazione o lo schiacciamento dell'alone di DM. Il Capitolo 1 è dedicato alla costruzione di 3 modelli di aloni di forma differente, che rispettino le principali previsioni delle simulazioni cosmologiche con sola DM (vedi Dutton & Macciò 2014). Nel Capitolo 2 presentiamo 3 modelli statici e 3 rotanti dell'ICM all'interno degli aloni del Capitolo 1: per verificare quanto effettivamente questi modelli siano realistici li confrontiamo con i profili termodinamici di Ghirardini et al. (2019) rappresentativi di un campione di ammassi "cool core", cioè con temperatura dell'ICM che decresce verso il centro. Da questo confronto, concludiamo che è possibile costruire distribuzioni di ICM realistiche immerse in un alone non necessariamente sferico in presenza di rotazione di $\lesssim 500\,\mathrm{km/s}$.
Nella seconda parte della tesi (Capitolo 3), testiamo i vincoli attuali sulla rotazione e sondiamo le prospettive future nei raggi X, ricostruendo i principali osservabili fotometrici e spettroscopici dai nostri modelli. Sebbene le morfologie della brillanza superficiale dei nostri modelli siano ampiamente consistenti con quelle osservate (e.g. Campitiello et al. 2022), non è possibile porre vincoli forti sulla rotazione dell'ICM. Infine, nel Capitolo 3, verifichiamo che lo spettrometro RESOLVE sia in grado di rivelare la rotazione dei nostri modelli dell'ICM per velocità lungo la linea di vista $\gtrsim 300\,\mathrm{km/s}$, persino in presenza di velocità turbolenta di $\lesssim 400\,\mathrm{km/s}$.
Da questo lavoro concludiamo che negli ammassi reali c'è possibilità di rotazione di $\lesssim 500\,\mathrm{km/s}$, che potrebbe essere misurata dagli strumenti futuri. La possibilità che la rotazione dell'ICM sia $\simeq 500\,\mathrm{km/s}$ acquisce una grande rilevanza non solo per apprezzare uno dei fenomeni fisici che plasmano la distribuzione dei barioni negli ammassi e regolano il loro bilancio energetico

tramite instabilità magnetorotazionale, ma anche per stimare accuratamente la massa degli ammassi, usati come traccianti cosmologici.

Introduction

Galaxy clusters are the largest gravitationally bound structures in the Universe. According to the **bottom-up** framework of structure hierarchical formation, the primordial small density perturbations grow via gravitational instability up to form the massive bound structures, known as dark matter (DM) halos. The pristine gas falls into the potential well of DM halos, formed in the intersections of cosmic filaments, and is heated via strong shocks up to nearly the halo virial temperature.

Dynamical evolution of the plasma in cool-core clusters. In the most massive DM halos (those of galaxy clusters) the gas accumulates to form the fully ionised plasma $\sim$ 5-10 keV, which we observe today: the intracluster medium (ICM). While the DM is subject only to the gravitational interactions, the baryons also undergo radiative processes. The high temperatures of the ICM and the lack of other extended emitting sources in the sky favour the observations of thermal emission of the ICM in the **X-ray band**. At the same time, when triggering the radiative processes, in the inner region of a galaxy cluster ($\sim$ 100 kpc, known as the **core**) the ICM is usually sufficiently dense to cool significantly: here the cooling time [roughly $t_{cool} := E/(dE/dt) \propto T^{1/2}/n_e$ (for Breemstrahlung), with E the internal energy of gas, n_e the number density of electrons and T their temperature] is shorter than Hubble's time t_H ($\sim$ 10 Gyr). The radiative cooling is expected to drive the monolithic collapse of the plasma in the core, which undergoes a **top-down condensation cascade** to dense warm (ionised) gas ($\sim$ 10^4-10^5 K) and, eventually, to cold (molecular) gas ($\lesssim$ 100 K). There is evidence for this thermal cascade (see *McNamara & Nulsen 2012* for a review): for instance, the observed multiphase structure of gas (*e.g. McDonald et al. 2012* and references therein) and the observed relation between molecular gas (traced usually via CO emission lines) and Hα emission (*e.g. Ho et al. 2009* and references therein). This radiatively cooling gas, following a filamentary-shaped cooling flow, likely rains toward the central brightest cluster galaxy (BCG), where this gas reaches sufficiently low temperature to be converted into stars or to be accreted by the central supermassive black hole (SMBH). The observed relation between the star formation rate (SFR) of BCGs and the cooling rate in mass ($\dot{M}_{cool}$) of the ICM (*e.g. McDonald et al. 2011, O'Dea et al. 2008* and references therein) proves indeed that the BCG (with its SMBH) and the ICM in the core are not separate elements of the cluster. However, the aforementioned and further signatures of an efficient radiative cooling of the ICM [such as the cusp of surface brightness (*e.g. Vikhlinin et al. 2006* and references therein) and a significant decrease of entropy profile (*e.g. McDonald et al. 2013* and references therein)] are detected only in a part of entire population, known as **cool-core clusters** (while, the remaining clusters are known as non-cool-core). In this work, we focus on cool-core clusters. Despite a substantial evidence of a moderate cooling flow, roughly constant in time-averaged sense for $\sim$ 10 Gyr (*e.g. McDonald et al. 2013* and references therein), the SFR and $\dot{M}_{cool}$ averaged over a long time ($\sim$ 5-8 Gyr) are not as

high as expected on the basis of standard cooling flow model (the observed SFR and $\dot{M}_{cool}$ are usually $\sim 1/10$ of those predicted; *e.g. O'Dea et al. 2008* and references therein). This tension is known as **cooling-flow problem**: the ICM appears in the multiwavelength observations **globally stable, but locally thermally unstable** in the very central regions (*e.g. McCourt et al. 2012, Gaspari et al. 2012*; see also *Section 2.2.1*). At first sight the cooling flow problem might have a simple solution: the presence of a heating mechanism responsible for halting the cooling flows and for preventing the monolithic collapse of the ICM in the core. However, this assumed mechanism could overheat the ICM preventing the local condensations typically observed in cool-core clusters (see above). In short, solving the cooling flow problem means to avoid at the same time overcooling and overheating of the ICM, preserving the structure and the thermodynamics of the ICM in the core for $\sim 10\,\mathrm{Gyr}$.
In the multiwavelength observations of clusters and massive galaxy groups there are two clear signatures: the radio emission in the core (*e.g. Carilli et al. 1994*), which traces the **radio-mode feedback** (see *Hlavacek-Larrondo et al. 2022* for a review) from the active galactic nucleus (AGN), and the **X-ray cavities**, filled with a thermal dilute plasma of temperature much higher than the halo virial temperature ($\gtrsim 20\,\mathrm{keV}$; *McNamara & Nulsen 2012*) or with relativistic particles in local pressure equilibrium with the surrounding ICM (*e.g. Carilli et al. 1994*). An observed scaling relation between cavity power and radio luminosity (*e.g. Bîrzan et al. 2008*) and the fact that in most cool-core clusters the positions of X-ray cavities closely match those of radio jets support the scenario, where the X-ray cavities and its plasma are inflated and heated via strong shocks by AGN relativistic jets up to $\gtrsim 20\,\mathrm{keV}$ or relativistic regime (*e.g. Sarazin et al. 1995, Carilli et al. 1994*; see *McNamara & Nulsen 2012* for a review). From the X-ray observations there is a clear evidence for a relation between the X-ray luminosity of the core and the cavity power (*e.g. Rafferty et al. 2006*), which spans seven decades in X-ray luminosity (from massive galaxies $\sim 10^{38}\,\mathrm{erg/s}$ to massive clusters $\sim 10^{45}\,\mathrm{erg/s}$): this cavity power-luminosity relation follows on average a line of equality between heating and radiative cooling. As consequence of the combination of these relations, the radio-mode AGN feedback provides the energy requested to offset the radiative cooling of the ICM. Moreover, given that the cavity power-luminosity relation spans a wide range of luminosity, the AGN-driven heating is not an *ad-hoc* mechanism to offset the radiative cooling only in massive clusters, but takes part of a **self-regulated mechanism**, in which the radiative cooling and the subsequent gas condensation in the core trigger the radio-mode AGN feedback via the accretion onto the BCG and central SMBH and, then, the AGN jets reheat via the X-ray cavities the ICM in the core up to nearly the halo virial temperature. On the basis of the previous considerations, the radio-mode AGN feedback from the BCG is believed to be the ideal candidate for preventing **in time-averaged sense** the monolithic collapse of the ICM in the core (*e.g. McNamara & Nulsen 2012, Rasia et al. 2015*) and, at the same time, for allowing for local condensations, even if the dynamical process, which transfers energy from the X-ray cavities to the ICM in the form of thermal energy, is still largely unknown. Can the radio-mode AGN feedback be entirely responsible for heating the ICM? Are there complementary mechanisms able to contribute significantly to the energetic budget of the ICM? These are important questions in the understanding of the thermodynamics of the ICM in the cool cores of galaxy clusters.
In this work, we study configurations of ICM in equilibrium within the DM halo. Assuming that cooling is balanced by an *ad-hoc* heating mechanism in a time-averaged sense, the configurations of the ICM represent the starting points to follow the local and global time evolution of the ICM subject to local perturbations. Recent results of linear-stability analysis and of magnetohydrodynamic (MHD) simulations show that the onset of local perturbations in a plasma affected by the combination of radiative cooling, of weak magnetic fields and of anisotropic heat conduction is the cause of serveral *local MHD instabilities* (*e.g. Nipoti & Posti 2013*, *Binney et al. 2009* and references therein). Nevertheless, *McCourt et al. (2012)* proves

that both in the linear and non-linear regimes no significant condensation of the ICM occurs, if the instability timescale is much longer than the dynamical time ($t_{dyn} := (2r/g(r))^{1/2}$, where $g(r)$ is the intensity of gravitational field and r is the radial spherical coordinate, under the assumption of spherical symmetry of gravitational field). The presence of a significant rotation of the ICM (expected from hydrodynamical simulations; *e.g. Nagai et al. 2013* and references threin) combined with a weak magnetic field leads to the formation of **magnetorotational monotonically unstable modes** in timescales as short as few dynamical times of the system (*Nipoti et al. 2015*). Consequently, the magnetorotational instability (MRI) can play an important role in the time evolution of the ICM: the MRI can drive potentially to a significant turbulent heating, which is belived to be an efficient mechanism to halt cooling flows within galaxy clusters. Following the non-linear evolution of magnetorotational unstable modes, future works could estimate the contribution of this turbulent heating to the energetic budget of rotating ICM.

Regularity of the thermodynamic properties of the ICM. In a gravitationally bound system the **halo virial temperature** (T_{vir}) is a proxy of the depth of the potential well (measured from the virial, **dynamical mass** M_{vir}): for a halo that follows the singular isothermal sphere, from the Virial Theorem (*Cimatti et al. 2019*)

$$T_{vir} = \frac{\mu m_p}{2^{4/3} k_B} (G M_{vir})^{2/3} \left[\Delta_c(z) H^2(z)\right]^{2/3},$$

where μ, m_p, k_B and $H(z)$ are the mean molecular weight, the mass of a proton, Boltzmann's Constant and Hubble's Parameter (see below), respectively (see *Section 2.1.1* for details on this Eq.). The concept of halo virial temperature is a prediction on the thermodynamic behavior of galaxy clusters, in particular. If the temperature of a gas in hydrostatic equilibrium is close to T_{vir}, we directly infer the dynamical mass of system from its temperature: this prediction thus is an useful tool to rapidly estimate with a good accuracy the mass. While the stars are the most significant contribution to the total baryonic mass of galaxies, the dominant baryonic mass component of massive galaxy clusters consists of a high-energy plasma, which is usually believed to be largely in hydrostatic equilibrium close to the halo virial temperature. So, when dealing with large surveys of massive clusters, this relation is widely used to infer their mass. To make these estimates easier, the temperature of the ICM is usually linked to X-ray or microwave observables (known as **mass proxies**) such as the X-ray luminosity or the electron pressure, respectively (see *Voit 2005*). However, a deviation from the virial relation is observed (see *Section 3.2.3*; *e.g. Reichert et al. 2011* and references therein): the departure from hydrostatic equilibrium of the ICM (see below) and the interplay between radiative cooling and feedback-driven heating are usually believed to be the cause of this deviation (*e.g. Kravtsov & Borgani 2012*).

There are theoretical predictions on how the thermodynamic quantities vary with the distance from the center of the potential well. From DM-only simulations, which model the growth of halos from the small primordial density perturbations up to the present-day structures, *Allgood et al. (2006)* detected the flattening of most present-day halos as a relic of past major mergers and found the redshift evolution of axial ratio of the halos. Despite the variety of shapes of halos (*e.g. Allgood et al. 2006*) and the inhomogeneities among their merging trees, their spherically averaged density profiles are well reproduced by an universal profile (*e.g. Navarro et al. 1996, Dutton & Macciò 2014*): the Navarro-Frenk-White (NFW) profile (*Navarro et al. 1996*).

In agreement with the predictions based on the assumptions of shock-heating and of hydrostatic equilibrium, even in the non-radiative N-body hydrodynamical simulations the profiles of the thermodynamic quantities of the ICM are universal (*e.g. Nagai et al. 2007a*). In presence of

radiative processes is the balance between radiative cooling and radio mode AGN feedback sufficient to preserve the universality of the thermodynamic profile of the ICM? To answer this important question, given the difficulty to cover via hydrodynamical simulations with a sufficient resolution the entire cluster (from the scale of central AGN $\sim$ 1-10 pc up to the virial radius $\sim$ 1 Mpc), we rely primarily on the observations. Recently a remarkable effort has been made to clean from impurities (like the clumpiness of ICM) the X-ray surface brightness profiles of the ICM and to improve the accuracy in the measure of the distortion of cosmic microwave background (CMB) spectrum (known as Sunyaev-Zel'dovich effect, SZE; *Sunyaev & Zeldovich 1972*), detectable at microwave wavelengths. From several works based on microwave and/or X-ray informations over the last decades there is clear evidence for a **regularity** among the thermodynamic profiles of the ICM outside the core (*e.g. Vikhlinin et al. 2006, Ghirardini et al. 2019* and references therein). Galaxy clusters in the central and outer regions thus are a homogeneous population, however they show a variety of thermodynamic behaviors in the cores, depending on the presence and prominence of cool cores. Ongoing observational campaigns were launched to study the thermodynamics of the ICM (*e.g.* CHEX-MATE Project; `http://xmm-heritage.oas.inaf.it/`): in particular, the cause of deviation from the virial scaling relations (likely the departure from hydrostatic equilibrium) and the influence of dynamical state of clusters on the thermodynamic behavior of the ICM.

Hydrostatic mass bias: a limit for the use of galaxy clusters as cosmological probes. Galaxy clusters are highly important test sites for cosmology (see *Voit 2005, Pratt et al. 2019* for reviews). The measurement of mass profile of any galaxy cluster is a powerful tool to test the predictions of cold dark matter paradigm on the internal structure of DM halos: primarily, the concentration-mass relation (see *Section 1.3*; *e.g. Ettori et al. 2010, Dutton & Macciò 2014*). Mostly, galaxy clusters are being used to constrain the cosmological density parameters: recovering the mass of a large sample of galaxy clusters at different redshifts, we trace the **time evolution of their mass function** (*Press & Schechter 1974*) and compare it to the theoretical predictions to constrain the geometry of the Universe (*i.e.* the overall density parameter Ω_0) and the contribution of any single component of the Universe to Ω_0 (*e.g. Vikhlinin et al. 2006*). Currently available telescopes are not able to observe the Early Universe, which developed the primordial perturbations. A way to infer informations on the power spectrum of initial density fluctuations (in particular, its normalization) is the observation of the Present-Day Universe: primarily, the mass function of galaxy clusters.
When dealing with large X-ray surveys of clusters, it is not possible to accurately measure individual masses for every object. The methods to constrain the cosmological parameters via cluster surveys thus rely on mass proxies, even though the deviation of scaling relations from the virial behavior forces us to empirically measure and calibrate them via X-ray observations. So, it is of great interest to accurately measure the mass of an as large as possible sample of galaxy clusters.
There are several methods to estimate the mass of galaxy clusters: two widely used approaches are based on X-ray and lensing observations. The X-ray measurement of the density and temperature profiles of the ICM provides one of the most reliable methods to determine the mass of galaxy clusters. However, the necessary thermodynamic profiles of the ICM to the reconstruction of mass profile, inferred from the X-ray observables via deprojection methods, are usually interpreted by assuming that the ICM is static (see *Ettori et al. 2013* for a review). Galaxy clusters, being the most massive structures of the Universe, are effective lenses, so the reconstruction of mass profile based on lensing observations is widely used (see *Meneghetti et al. 2010*). While the mass recovered via X-ray observations is underestimated in presence of significant large-scale bulk motions of the ICM (included the rotation or turbulence), the method

to reconstruct the mass of clusters via lensing observations is fully independent of the kinematics of the ICM (see *Pratt et al. 2019*). In general, there is a tension among these methods, known as **hydrostatic mass bias** in the sense that the mass estimated via lensing observations tends to be higher than the mass inferred from X-ray observations. One way to account for the typically found biases of $5-30\%$ of total mass in relaxed clusters (*e.g. Meneghetti et al. 2010*, *Pratt et al. 2019*) is to consider departures from hydostatic equilibrium, in the sense that additional contributions beyond the thermal pressure support partly the ICM in equilibrium in the potential well of clusters (see also *Section 2.3*).
In general, the ICM continuously undergoes external perturbations (induced by, e.g., mergers and matter accretion along cosmic filaments; *e.g. Nagai et al. 2013, Vazza et al. 2017*) and internal pertubations [due to, e.g., the feedback processes from stars and central AGN (*e.g. Gaspari et al. 2012*), motions of galaxies, MHD instability (see above and, e.g., *McCourt et al. 2011*)]. All these phenomena are able to trigger turbulence, rotation or streaming motions, which alter the hydrostatic equilibrium of the ICM. Over the last two decades, it has been studied how an additional pressure support from random turbulent motions of the ICM contributes to mass biases, when assuming the hydrostatic equilibrium (*e.g. Nagai et al. 2007b*). However, few works thus far accounted for the mass biases due to an additional support from rotation of the ICM (*e.g. Fang et al. 2009*, *Nipoti et al. 2015*).

Gas rotation in clusters: current upper limits and detectability with new generation facilities. Several features observed in some galaxy clusters [such as the detection of substructures (*e.g. Geller & Beers 1982*), non-Maxwellian galaxy velocity distributions (*e.g. Beers et al. 1990*) or the X-ray surface brightness distorsions (*e.g. Buote & Tsai 1995*)] are interpreted by *Sunyaev et al. (2003)* as the signatures of past mergers and accretion events. According to hydrodynamic simulations which model the bottom-up growth of structures, one of the possible consequences of merging and matter accretion is the rotation of the ICM in the outer regions of clusters (*e.g. Nagai et al. 2007b, Nagai et al. 2013*), if a significant part of angular momentum of two merging clusters is preserved. Furthermore, from a comparison between the results of non-radiative and radiative numerical hydrodynamical simulations *Lau et al. (2011)* concluded that the presence of a relatively efficient radiative cooling enhances the rotational support of the ICM in the cool cores of clusters (see also *Fang et al. 2009*).
The best method to detect the rotation speed is usually based on the **Doppler shift of the centroids of the emission lines** in the X-rays: for a typical speed of $\simeq 500\,\mathrm{km/s}$ *Sunyaev et al. 2003* estimated that the Doppler shift of an iron line at 6.7 eV would be $\simeq 10\,\mathrm{eV}$. This dectection requires high energy resolution (ΔE) of X-ray spectrometers: $\Delta E \lesssim 10\,\mathrm{eV}$ thus far was reached only by the X-ray Calorimeter Spectrometer ($\Delta E \simeq 5\,\mathrm{eV}$) on board of ASTRO-H (`https://heasarc.gsfc.nasa.gov/docs/hitomi/`) before losing its contact. The only spectrum of a galaxy cluster observed by ASTRO-H is that of the core of Perseus (relaxed) cluster, where thanks to the measurement of the non-thermal broadening of the emission lines (see *Section 3.2.1*) were found a line of sight velocity dispersion of $164 \pm 10\,\mathrm{km/s}$ (*Hitomi Collaboration et al. 2016*). This measurement is usually interpreted as a reference speed of the turbulence of the ICM. In the spectra of the entire cluster or of its core, the rotation of the ICM, together with the turbulence and the bulk motions of other nature, contributes to the broadening of emission lines, so it is hard to split these different components. Instead, in the spectra of a partial region of cluster, where the ICM is either approaching or receding, the rotation speed of the ICM produces only the shift of the emission line centroids from their rest-frame energies. Therefore there are more chances to detect the rotation of the ICM via a spatially resolved observation of a cluster partial region, but it requires a high angular resolution of X-ray spectrometers. In general, despite a sufficient angular resolution of current spectrometers, the lack

of a currently available X-ray instrument of sufficiently high energy resolution ($\Delta E \gtrsim 100\,\mathrm{eV}$ for current spectrometers) do not allow for this detection. Nevertheless, using CHANDRA (of $\Delta E \simeq 150\,\mathrm{eV}$; `https://www.nasa.gov/mission_pages/chandra/main/index.html`) data, *Liu & Tozzi (2019)* investigate via the Doppler shift of the centroids of the emission lines the possibility that the galaxy cluster *Abell 2107* rotates or undergoes a merging: even though they cannot exclude the merger scenario, assuming rotation on cylinders they found a maximum tangential speed of $1380 \pm 600\,\mathrm{km/s}$ at a radius of $\simeq 160\,\mathrm{kpc}$.
In the future, the X-ray instruments (bolometers) of new generation, such as RESOLVE on board of XRISM ($\Delta E \simeq 6\,\mathrm{eV}$; `https://xrism.isas.jaxa.jp/en/`) or the spectrometer X-IFU on ATHENA ($\Delta E \simeq 2.5\,\mathrm{eV}$; `https://www.the-athena-x-ray-observatory.eu/`), will depict a comprehensive overview of the kinematics of the ICM thanks to their higher energy resolutions (see, *e.g.*, *Roncarelli et al. 2018*): the high quality of X-ray spectra of new generation spectrometers allow us to measure the Doppler shifts and broadening of the emission lines with accuracy and precision comparable for RESOLVE to the calorimeter on board of ASTRO-H and with unprecedented accuracy and precision for X-IFU. XRISM is a X-ray space telescope built by japanese space agency, that will be active since 2023; XRISM will carry two instruments for studying the soft X-ray energy range, RESOLVE and XTEND, for each of which the satellite will have telescopes of focal length of 5.6 m: SXT-S (Soft X-ray Telescope for Spectrometer) and SXT-I (Soft X-ray Telescope for Imager), respectively. In particular, RESOLVE is a soft X-ray microcalorimeter developed by NASA (`https://www.nasa.gov/`). While, ATHENA is a future X-ray space telescope and is scheduled to be launched in 2035 by European Space Agency (ESA; `https://www.esa.int/`). Future works using RESOLVE or X-IFU data will sample the clusters with a significant rotation or turbulence to solve the problem of hydrostatic mass bias (*i.e.* the tension between mass estimators) and will estimate the average rotational and turbulent supports of the ICM that could be the cause of deviation of scaling relations from the virial behavior (see above and *Section 3.2.3*).
A promising direct probe for gas rotation in galaxy clusters in the future is the distorsion of the CMB spectrum due to the rotation of the ICM, known as the **rotational kinetic Sunyaev-Zel'dovich Effect** (rkSZE; *Cooray & Chen 2002*). The Inverse Compton scattering between the CMB photons and the free electrons of the ICM produces a distortion of CMB spectrum: measuring the shift of CMB signal from the wavelengths of rest-frame CMB means to estimate the total energy of electrons of the ICM (see *Mroczkowski et al. 2019* for a review). The microscopic random (thermal) motion of the ICM and the velocity of the entire cluster moving in the large-scale structure of the Universe (known as peculiar velocity) primarily contribute to the energetics of electrons in the CMB rest-frame, however a significant rotation of the ICM provides a non-negligible energy fraction (*e.g. Nagai et al. 2013* and references therein). Indeed, the non-null (in the CMB rest-frame) line of sight tangential speed of electrons produces an additional shift of CMB signal: a temperature increment for approaching ICM and a temperature decrement for receding ICM. When mapping the CMB in the plane of the sky, rkSZE induces a dipole-like distortion, which differs significantly from that due to the thermal motion of electrons (known as thermal Sunyaev-Zel'Dovich Effect, tSZE; *Sunyaev & Zeldovich 1972*) and from the monopole-like distortion related to the line of sight peculiar speed of cluster (known as kinetic Sunyaev-Zel'Dovich Effect, kSZE; *Sunyaev & Zeldovich 1980*). This signature favour the observations of rkSZE in real clusters, however few attempts thus far have been made to this end. Mock observations performed on clusters from high-resolution hydrodynamical simulations (*e.g. Baldi et al. 2018, Altamura et al. 2023*) demonstrate the significance and the detectability of the rkSZE, when comparing to the dominant distorsions of CMB spectrum, tSZE and kSZE.
For the sake of completeness, we report some results on the bulk motions and, in particular, rotation in galaxy clusters. If the ICM and member galaxies are both in equilibrium into the

potential well of halo, they likely follow the same rotation law. We thus trace the rotation of the ICM via the Doppler shift of the centroids of optical emitting lines of member galaxies: though few attempts (*e.g. Kalinkov et al. 2005*), the sparse and discrete sampling of member galaxies discourage the use of optical wavelengths to this end. Furthermore, over the last decade a remarkable effort has been made to provide new methods to measure in absence of an X-ray instrument of high energy resolution the bulk speeds of the ICM: primarily, the turbulent speed of the ICM (*e.g. Rebusco et al. 2005*, *Zhuravleva et al. 2012, Zhuravleva et al. 2022* and references therein), even if there were thus far few detections. In absence of direct detection of speed of the ICM, we report a possible upper limit on the rotation of the ICM provided by an indirect measurement: the speed of a merging cluster. Thanks to the detection of a bow shock, *Springel & Farrar 2007* measure the speed of a minor merger among galaxy clusters $\gtrsim 2500\,\mathrm{km/s}$. Assuming the rotation of the ICM as a consequence of merger (*e.g. Nagai et al. 2013*) and the tight conservation of angular momentum during this merging, $2500\,\mathrm{km/s}$ is interpreted as a reference upper limit on the peak of rotation speed of the ICM.

The targets of this work in the context of the study of the ICM. The predicted regularity of the internal strucuture of the halos (such as the universal spherically averaged density profile and the mass-concentration relation; see *Section 1.3.1*, *e.g. Navarro et al. 1996, Dutton & Macciò 2014* and references therein) and the observed regularity of the thermodynamic properties of the ICM (*e.g. Ghirardini et al. 2019* and references therein) are appreciable and important results obtained by independent works, but is there a self-consistent and comprehensive description of the properties of both dark and baryonic components in cool-core clusters? It is hard to find together these results in clusters from a N-body hydrodynamical high-resolution simulation, which models the bottom-up growth of density small perturbations up to form the present-day clusters. We thus rely on the combination of these results inferred from independent works.
In this work the physical engines, which shape the distribution of the ICM throughout the cluster, are the gravity of halo and the rotation of the ICM, if any. Assuming polytropic distributions, we explore the equilibrium of the ICM for a variety of the shapes of halos [expected from DM-only simulations (*e.g. Allgood et al. 2006*)] and for different kinematic conditions of the ICM [expected on the basis of the hydrodynamical simulations (*e.g. Nagai et al. 2007b, Nagai et al. 2013*), of the tension between mass estimators (*e.g. Pratt et al. 2019* and references therein) and of few measurements (*Liu & Tozzi 2019* and references therein)], while preserving the regularity of the thermodynamic properties of the ICM and of the internal structure of halos. We thus propose six realistic models of the ICM plus the DM that depict the two dominant mass components in a typical massive cool-core clusters as expected by unifying the results discussed in this Introduction.
Due to the high content of thermal energy of the ICM the works over the last decades consider the X-rays the most promising wavelengths to study the ICM and emphasized the prominent role, which could play the high quality X-ray spectra in the understanding of the kinematics of the ICM (*e.g. Sunyaev et al. 2003*). Moreover, a way to indirectly constrain the gas rotation (*e.g. Bianconi et al. 2013*) and the shape of halos (*e.g. Buote & Canizares 1992*) is through the morphology of X-ray surface brightness distribution. Assuming the spherical symmetry of halo to build realistic models of rotating ICM and using primarily the observed ellipticity profile as constraint on the rotation patterns, *Bianconi et al. (2013)* conclude that there is room for an ICM rotation of $\lesssim 600\,\mathrm{km/s}$ in real clusters. In this work, comparing the X-ray photometric observables reconstructed from our models of the ICM to currently available results, we discuss the limits and possibilities to constrain the rotation patterns on the basis of the morphology of X-ray surface brightness distribution of real clusters. Then, performing an analysis of mock

X-ray spectra we investigate one of possible applications of RESOLVE: measuring the gas rotation under different turbulent conditions of the ICM in real galaxy clusters. It means not only to appreciate the kinematic conditions of the ICM, but also to understand their role in shaping the thermodynamic properties of the ICM and, consequently, to control the mass biases in the use of clusters as cosmological probes.

This thesis is organised as follows. In *Chapter 1* we build the models of halos that shape the potential well, where the ICM is in equilibrium. In *Chapter 2* we present our static and rotating realistic models of the ICM. *Chapter 3* is devoted to the reconstruction of X-ray photometric observables and to the analysis of a collection of mock X-ray spectra constructed from our models of the ICM. While the intrinsic properties of the models of the ICM are fully analytic, their observables are numerical.
Thoughout this thesis we assume the concordance ΛCDM cosmological model, where the Hubble's constant is $H_0 = 70\,\mathrm{km/s/Mpc}$, the parameter of density of overall (baryonic plus dark) matter at redshift $z = 0$ $\Omega_{m,0} = 0.3$ and the parameter of density of cosmological constant at $z = 0$ $\Omega_{\Lambda,0} = 0.7$. The critical density of the Universe at redshift z is $\rho_{crit}(z) = 3H^2(z)/(8\pi G)$, where G is the universal constant of gravity, $H(z) = H_0 E^{1/2}(z)$ and $E(z) = \sqrt{\Omega_{\Lambda,0} + \Omega_{m,0}(1+z)^3}$.

Chapter 1

Flattened DM halos

Most mass of a galaxy cluster resides in DM particles (which we expect to have masses $\gtrsim$ GeV). To compute the gravitational potential of a large collection of DM particles, using the superposition principle we can add together the point-like potentials of all the DM particles, which compose a DM halo. It is not practicable numerically, despite the remarkable improvement of computer performance, since the number of DM particles, in a mass of $\sim 10^{15}\,\mathrm{M}_{\odot}$, is expected to be enormous. We thus rely on an analytic density-potential pair, which mimic in a time-averaged sense the density spatial distribution and, consequently, the potential of DM particles in a halo, respectively. The assumption of a negligible gravitational field of stars is not always justified in the innermost region of clusters, where the mass of BCG is comparable to dark component. Formally we can interpret the assumed density-potential pair as due to DM plus stars.
The difficulty to infer from the observations the morphology of DM halos suggests us to rely on N-body simulations. In cosmological DM-only simulations the spherically symmetric halos are rare (*e.g. Allgood et al. 2006*): one would not expect halos to be spherical if the relaxation time is longer than the time between mergers, if mass accretion onto DM halos is directional and/or if the infalling subhalos come along preferential direction (such as along a filament). During the formation of present-day halos the major mergers are frequent and ubiquitous: even if galaxy clusters are located in the intersections of cosmic filaments, where the infalling mass come from a fairly random direction, the shape of their DM halos likely reflects the last **major marger**. One way to account for the DM halo flattening is to go one step beyond the spherical approximation and to approximate the halos as homeoids. Despite the use of **homeoidal approximation**, it is hard to find analytic density-potential pairs. However, the universal density profile of DM halos (that is the NFW), obtained from DM-only simulations as average in spherical shells (*e.g. Navarro et al. 1996*), can be thought as a zero-order term of a homeoidal density distribution. We thus find an exact flattened density-potential pair via a **homeoidal expansion** (*Ciotti & Bertin 2005*) of NFW profile up to the first significant order in flattening.

This Chapter is organised as follows. The method to construct a flattened density-potential pair from a homeoidal expansion is described in *Section 1.1*, while the *Sections 1.2.1* and *1.2.3* are devoted to the application to the NFW (the profiles of the gravitational field are derived in *Section 1.2.4*). However, to avoid an unphysical density distribution we limit the flattening, as discussed in *Section 1.2.2*. In *Section 1.3* we present our models of halos that respect the main predictions on their internal structure.

1.1. Homeoidal expansion technique

The homeoidal expansion technique is a simple method to construct an exact flattened density-potential pair. When going one step beyond the spherical symmetry, we usually use the ellipsoidal symmetry: despite the difficulty to find the analytic form of the potential of a generic density distribution stratified over homeoids, the limit for small flattening, known as homeoidal expansion, is remarkably simpler.
Let us consider a density distribution stratified over homeoidal surfaces: $\rho_m(\mathbf{x}) = \rho_0\tilde{\rho}(m)$ with $\mathbf{x} = (x; y; z)$ and

$$m^2(x; y; z) = \frac{x^2}{a^2} + \frac{y^2}{b^2} + \frac{z^2}{c^2} = \frac{x^2}{a^2} + \frac{y^2}{a^2(1-\epsilon)^2} + \frac{z^2}{a^2(1-\eta)^2}, \tag{1.1}$$

where ϵ and η are sufficiently small dimensionless parameters ($0 < \epsilon, \eta \ll 1$) such that $b = a(1-\epsilon)$ and $c = a(1-\eta)$. ϵ and η are the ellipticities of the ellipses in the plane $z = 0$ and $y = 0$, respectively: they essentially parametrize the significance of flattening. The density distribution depends only on m: in *Eq.(1.1)* a, b and c are constant. η and ϵ as well as the axial ratios ($1-\epsilon$ or $1-\eta$) thus are constant for any m.
In general, any ellipsoidal distribution (prolate, oblate or triaxial) can be built via a homeoidal expansion, but in this project we focus only on

- **prolate ellipsoid** for $0 < \eta = \epsilon \ll 1$ (*i.e.* $b = c < a$), such that the equatorial plane is located at $x = 0$ and the symmetry axis is x;

- **oblate ellipsoid** for $\epsilon = 0$ and $0 < \eta \ll 1$ (*i.e.* $a = b > c$), such that the equatorial plane is located at $z = 0$ and the symmetry axis is z;

Any density distribution $\rho(\mathbf{x})$ produces a gravitational potential $\Phi(\mathbf{x})$, which satisfies the **Poisson Equation**

$$\nabla^2\Phi(\mathbf{x}) = 4\pi G\rho(\mathbf{x}). \tag{1.2}$$

Any solution of *Eq.(1.2)* with a positive $\rho(\mathbf{x})$ is called a density-potential pair. *Eq.(1.2)* allows us to infer the gravitational potential from any density distribution, but the solution is analytic only in special cases.
It is useful to work with dimensionless quantities:

$$\tilde{\rho}(\mathbf{x}) = \frac{\rho(\mathbf{x})}{\rho_0}, \tag{1.3}$$

$$\tilde{x} := \frac{x}{a},$$
$$\tilde{y} := \frac{y}{a},$$
$$\tilde{z} := \frac{z}{a}$$

and

$$\tilde{\Phi}(\tilde{\mathbf{x}}) := \frac{\Phi(\mathbf{x})}{4\pi G\rho_0 a^2}. \tag{1.4}$$

Any dimensionless density-potential pair ($\tilde{\rho}(\tilde{\mathbf{x}})$ and $\tilde{\Phi}(\tilde{\mathbf{x}})$) satisfies the dimensionless Poisson eq.

$$\tilde{\nabla}^2\tilde{\Phi} = \tilde{\rho}, \tag{1.5}$$

where $\tilde{\nabla} = a\nabla$.
Under the assumption of small flattenings ($0 < \epsilon, \eta \ll 1$), we expand the homeoidal density-potential pair ($\tilde{\rho}(m) = \rho(m)/\rho_0$ and $\tilde{\Phi}(m) = \Phi(m)/(4\pi G\rho_0 a^2)$) around the spherical term of $\epsilon = \eta = 0$ ($\tilde{\rho}(\tilde{r})$ and $\tilde{\Phi}_0(\tilde{r})$) up to the first significant order in ϵ and η (for details see *Ciotti & Bertin 2005*):

$$\tilde{\rho}(m) = \tilde{\rho}(\tilde{r}) + \frac{\epsilon\tilde{y}^2 + \eta\tilde{z}^2}{\tilde{r}}\rho'(\tilde{r}) + o(\epsilon^2 + \eta^2), \tag{1.6}$$

where $\tilde{r} := \frac{r}{a} = \sqrt{\tilde{x}^2 + \tilde{y}^2 + \tilde{z}^2}$ and $\rho'(\tilde{r}) := \frac{d\tilde{\rho}}{d\tilde{r}}$ with $\tilde{\rho} = \tilde{\rho}(\tilde{r})$;

$$\tilde{\Phi}(m) = \tilde{\Phi}_0(\tilde{r}) + (\epsilon + \eta)[\tilde{\Phi}_1(\tilde{r}) - \tilde{\Phi}_0(\tilde{r})] + (\epsilon\tilde{y}^2 + \eta\tilde{z}^2)\tilde{\Phi}_2(\tilde{r}) + o(\epsilon^2 + \eta^2), \tag{1.7}$$

where

$$\tilde{\Phi}_0(\tilde{r}) := -\frac{1}{\tilde{r}}\int_0^{\tilde{r}} \tilde{\rho}(m)m^2 dm - \int_{\tilde{r}}^{\infty} \tilde{\rho}(m)m dm, \tag{1.8}$$

$$\tilde{\Phi}_1(\tilde{r}) := -\frac{1}{3\tilde{r}^3}\int_0^{\tilde{r}} \tilde{\rho}(m)m^4 dm - \frac{1}{3}\int_{\tilde{r}}^{\infty} \tilde{\rho}(m)m dm \tag{1.9}$$

and

$$\tilde{\Phi}_2(\tilde{r}) := \frac{1}{\tilde{r}^5}\int_0^{\tilde{r}} \tilde{\rho}(m)m^4 dm. \tag{1.10}$$

The zero-order term of *Eq.(1.7)* $\tilde{\Phi}_0$ (given by *Eq.(1.8)*), representing the spherically symmetric potential, satisfies the spherically symmetric Poisson Equation

$$\frac{1}{\tilde{r}^2}\frac{d}{d\tilde{r}}\left(\tilde{r}^2\frac{d\tilde{\Phi}_0}{d\tilde{r}}\right) = \tilde{\rho}(\tilde{r}). \tag{1.11}$$

Ciotti & Bertin (2005) show that the dimensionless potential $\tilde{\Phi}_1(\tilde{r}) - \tilde{\Phi}_0(\tilde{r}) + \tilde{z}^2\tilde{\Phi}_2(\tilde{r})$ and the dimensionless density $\tilde{z}^2\tilde{\rho}'(\tilde{r})/\tilde{r}$ satisfy *Eq.(1.5)*. By the linearity of *Eq.(1.5)* it follows that $\tilde{\Phi}(m)$ and $\tilde{\rho}(m)$ to first-order in flattening are an exact flattened density-potential pair. The homeoidal expansion technique thus consists in finding an exact flattened density-potential pair from a homeoidal expansion of *Eq.s (1.6)* and *(1.7)*, in this case, up to the first significant order in flattening. This exact flattened density-potential pair has no ellipsoidal symmetry, even if it is generated from a homeoidal expansion. In short, a homeoidal expansion can be used not only to approximate a homeoidal density-potential pair for small flattenings, but also to produce **an exact aspherical density-potential pair** for finite (not necessarily small) ellipticities.
The homeoidal expansion of the dimensionless gravitational field is

$$\begin{aligned}\tilde{\mathbf{g}}(\tilde{\mathbf{x}}) := -\tilde{\nabla}\tilde{\Phi}(m) = &-\tilde{\nabla}\tilde{\Phi}_0(\tilde{r}) - (\epsilon + \eta)\tilde{\nabla}[\tilde{\Phi}_1(\tilde{r}) - \tilde{\Phi}_0(\tilde{r})] + \\ &- \tilde{\nabla}[(\epsilon\tilde{y}^2 + \eta\tilde{z}^2)\tilde{\Phi}_2(\tilde{r})] + o(\epsilon^2 + \eta^2),\end{aligned} \tag{1.12}$$

where

$$\tilde{\mathbf{g}}(\tilde{\mathbf{x}}) := \frac{\mathbf{g}(a\tilde{\mathbf{x}})}{4\pi G\rho_0 a}$$

and $\tilde{\mathbf{x}} := (\tilde{x}, \tilde{y}, \tilde{z})$.

1.2. A flattened density-potential pair from the homeoidal expansion of NFW profile

Let us take the NFW density-potential pair as zero-order term of a homeoidal expansion:

$$\rho(r) = \frac{\rho_r}{\left(\frac{r}{r_s}\right)\left(1+\frac{r}{r_s}\right)^2} \tag{1.13}$$

and

$$\Phi_0(r) = -4\pi\rho_r r_s^2 \frac{\ln\left(1+\frac{r}{r_s}\right)}{\frac{r}{r_s}}. \tag{1.14}$$

In dimensionless form, using *Eq.s (1.3)* and *(1.4)* with $a = r_s$ and $\rho_0 = \rho_r$, we have

$$\tilde{\rho}(\tilde{r}) = \frac{1}{\tilde{r}(1+\tilde{r})^2} \tag{1.15}$$

and

$$\tilde{\Phi}_0(r) = -\frac{\ln(1+\tilde{r})}{\tilde{r}}. \tag{1.16}$$

Before working with a homeoidal expansion, we report below in dimensionless units the proof that *Eq.(1.16)* is the potential produced by the density distribution in *Eq.(1.15)*. We begin with the innermost derivative of right-hand side (hereafter, RHS) of *Eq.(1.11)*:

$$\frac{\tilde{r}^2 d\tilde{\Phi}_0}{d\tilde{r}} = -\tilde{r}^2 \frac{\frac{\tilde{r}}{1+\tilde{r}} - \ln(1+\tilde{r})}{\tilde{r}^2} = \ln(1+\tilde{r}) - \frac{\tilde{r}}{1+\tilde{r}}.$$

Substituting the above expression in the Poisson eq. *(1.11)* and deriving again, we conclude our demonstration:

$$\frac{1}{\tilde{r}^2}\frac{d}{d\tilde{r}}\left(\tilde{r}^2\frac{d\tilde{\Phi}_0}{d\tilde{r}}\right) = \frac{1}{\tilde{r}^2}\left(\frac{1}{1+\tilde{r}} - \frac{1+\tilde{r}-\tilde{r}}{(1+\tilde{r})^2}\right) = \frac{1}{\tilde{r}(1+\tilde{r})^2}.$$

1.2.1. Flattened density distribution

The derivative of $\tilde{\rho}(\tilde{r})$ is

$$\frac{d\tilde{\rho}}{d\tilde{r}} = -(1+\tilde{r})^{-2}\tilde{r}^{-2} - 2\tilde{r}^{-1}(1+\tilde{r})^{-3} = -\tilde{r}^{-2}(1+\tilde{r})^{-3}(\tilde{r}+2\tilde{r}+1) = -\frac{1+3\tilde{r}}{\tilde{r}^2(1+\tilde{r})^3}. \tag{1.17}$$

Substituting *Eq.(1.17)* into *(1.6)*, we get the homeoidal expansion of NFW density profile

$$\tilde{\rho}(m) = \frac{1}{\tilde{r}(1+\tilde{r})^2} - \frac{\epsilon\tilde{y}^2+\eta\tilde{z}^2}{\tilde{r}}\frac{1+3\tilde{r}}{\tilde{r}^2(1+\tilde{r})^3} + o(\epsilon^2+\eta^2). \tag{1.18}$$

Eq.(1.18) shows the role of the term to first order in the ellipticities: the flattening of the distribution occurs by subtracting a part of the NFW density along the directions $\tilde{y}$ and $\tilde{z}$.

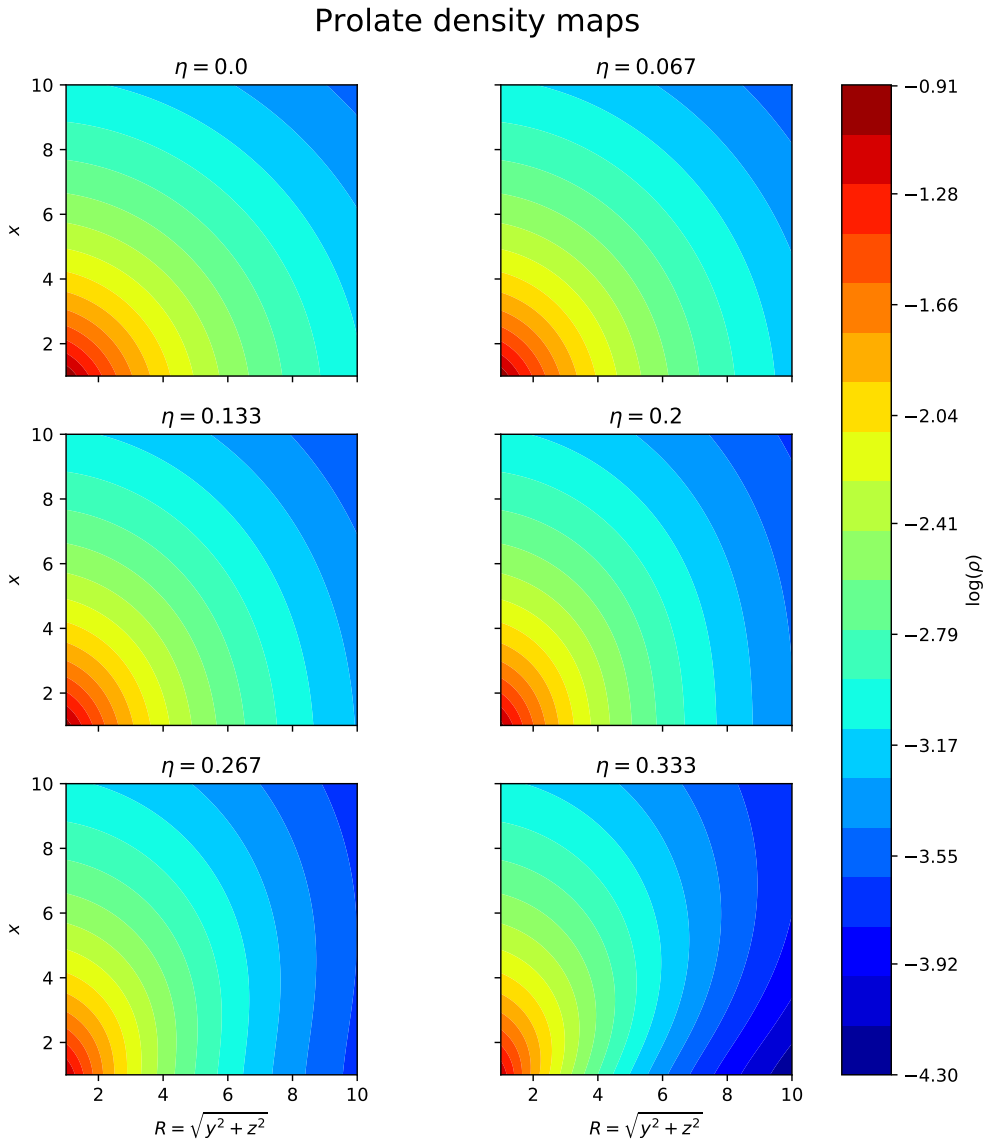

Figure 1.1.: Maps of dimensionless density $\rho(R/r_s; z/r_s)/\rho_r$ in the meridional plane for a selection of prolate NFW halos (see *Eq.(1.19)*). η spans the range $[0; 1/3]$ ($\eta = 0$ refers to the spherical NFW).

The absence of first-order term for $\tilde{y} = \tilde{z} = 0$ in *Eq.(1.18)* (*i.e.* along the $\tilde{x}$ axis) breaks the spherical symmetry of distribution, since no subtraction of NFW density occurs along the $\tilde{x}$ axis (hereafter, the unperturbed axis). In short, for declining density profile to zero-order, the first-order term drives a **directional subtraction** of a part of density of spherically symmetric distribution.

The dimensionless density distributions used in this work are

- when the subtraction of NFW density occurs in the equatorial plane (some examples in *Figure 1.1*),

$$\tilde{\rho}_{pro}(R; z) = \frac{1}{\tilde{r}(1+\tilde{r})^2} - \frac{\eta \tilde{R}^2}{\tilde{r}} \frac{1+3\tilde{r}}{\tilde{r}^2(1+\tilde{r})^3}, \tag{1.19}$$

  where $\tilde{R} = \sqrt{\tilde{y} + \tilde{z}}$ is the radius in the equatorial plane and $\tilde{r} = \sqrt{\tilde{R}^2 + \tilde{x}^2}$;

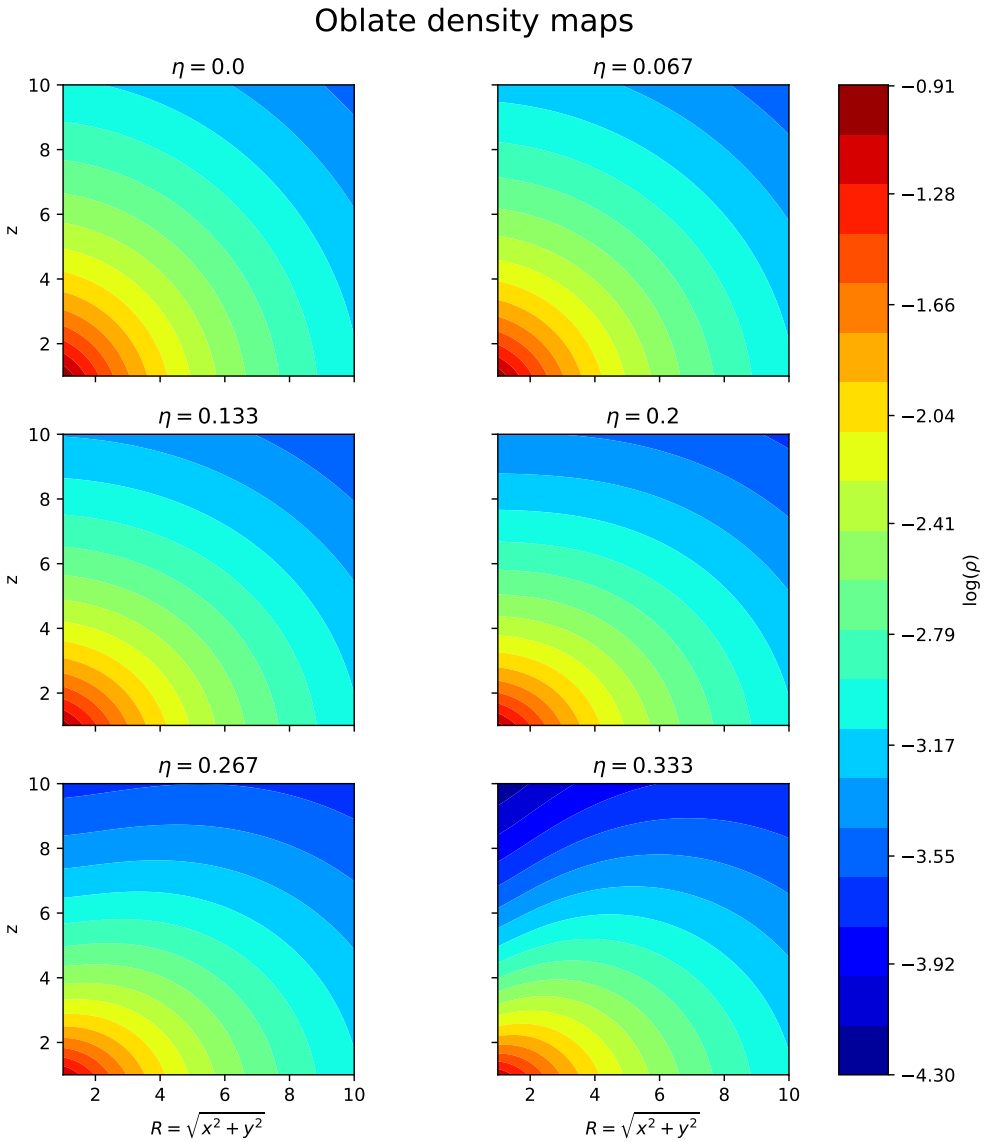

Figure 1.2.: Same as *Figure 1.1*, but for a selection of oblate NFW halos (see *Eq.(1.20)*).

- when the substraction of NFW density occurs along the vertical direction in the meridional plane (some examples in *Figure 1.2*),

$$\tilde{\rho}_{obla}(R;z) = \frac{1}{\tilde{r}(1+\tilde{r})^2} - \frac{\eta\tilde{z}^2}{\tilde{r}}\frac{1+3\tilde{r}}{\tilde{r}^2(1+\tilde{r})^3}, \tag{1.20}$$

  where $\tilde{z}$ is the symmetry axis and $\tilde{r} = \sqrt{\tilde{R}^2 + \tilde{z}^2}$.

We note that *Figure 1.1* differs from *1.2* only in the direction of flattening as well as *Eq.(1.19)* from *Eq.(1.20)*. Given that the first-oder terms of *Eq.s (1.19)* and *(1.20)* are $\propto \tilde{R}^2/\tilde{r}$ and $\propto \tilde{z}^2/\tilde{r}$, respectively, the subtraction of NFW density is more significant outwards. For high η it induces axial ratios of isodenses $< 1-\eta$ and a **peanut-shaped** distribution far from the center.
It is evident from *Eq.(1.18)* that the density distribution would assume negative values if the directional subtraction of density is sufficiently large: given that ϵ and η measure the density subtraction, the condition that the density is positive-defined at any point of space imposes upper limits on ϵ and η, derived in the next Section (*1.2.2*).

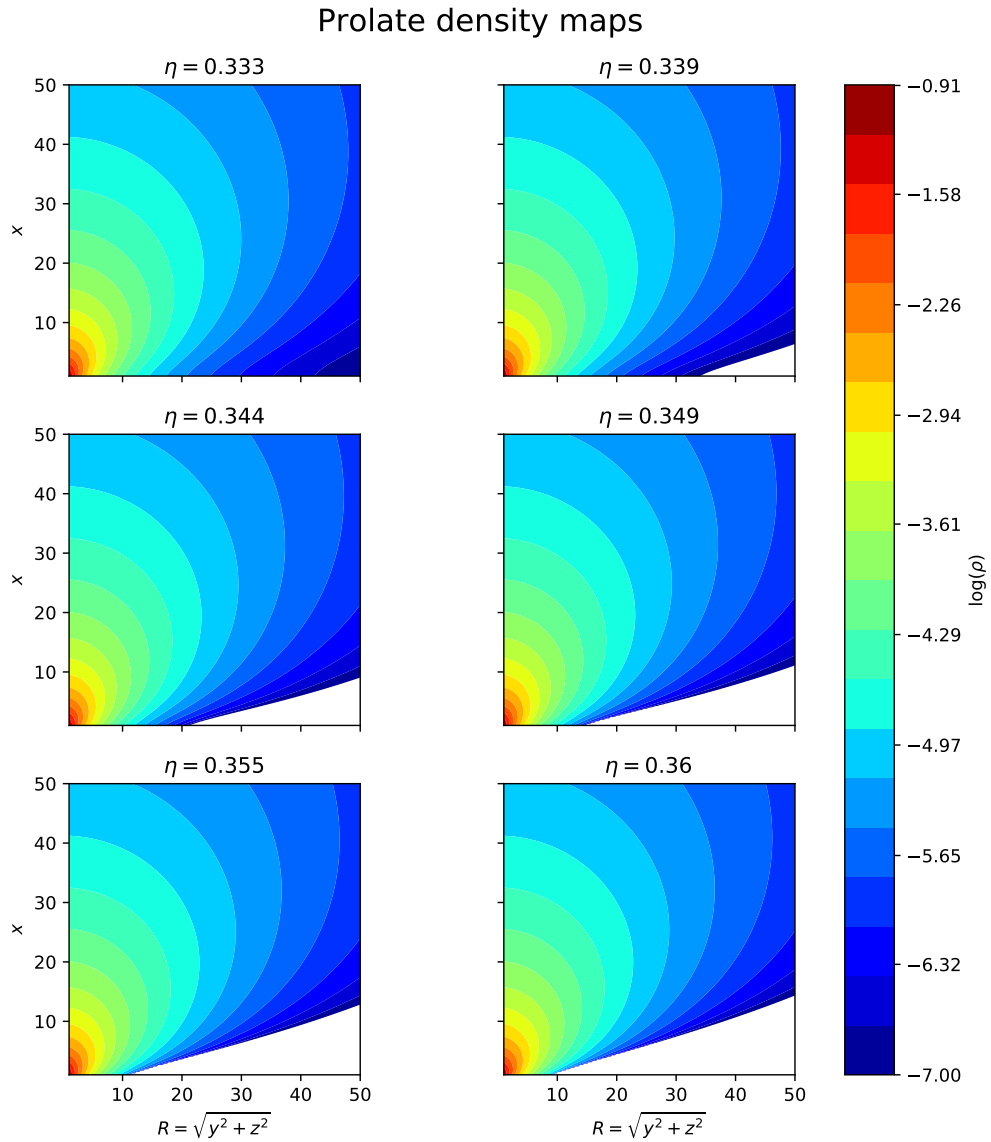

Figure 1.3.: Same as *Figure 1.1*, but for η spanning the range $[1/3; 0.36]$. In the *white* regions the density is negative and thus unphysical.

1.2.2. Analytic constraint on flattening

To avoid unphysical density distributions we limit the subtraction of density in the following way. We suppose $\epsilon \leq \eta$ without loss of generality, because thanks to the spherical symmetry of zero-order term we can select any perpedicular direction as a, b or c (of *Eq.(1.1)*). When $\frac{d\tilde{\rho}}{d\tilde{r}} \leq 0$ as it is usual, for sufficiently high η the density homeoidal expansion (RHS of *Eq.(1.6)*) assumes a negative value at least at a point of space. We rewrite the condition

$$\tilde{\rho}(\tilde{r}) + \frac{\epsilon\tilde{y}^2 + \eta\tilde{z}^2}{\tilde{r}} \frac{d\tilde{\rho}}{d\tilde{r}} \geq 0$$

as

$$1 - \frac{\epsilon\tilde{y}^2 + \eta\tilde{z}^2}{\tilde{r}^2} \left| \frac{d\ln\tilde{\rho}(\tilde{r})}{d\ln\tilde{r}} \right| \geq 0. \tag{1.21}$$

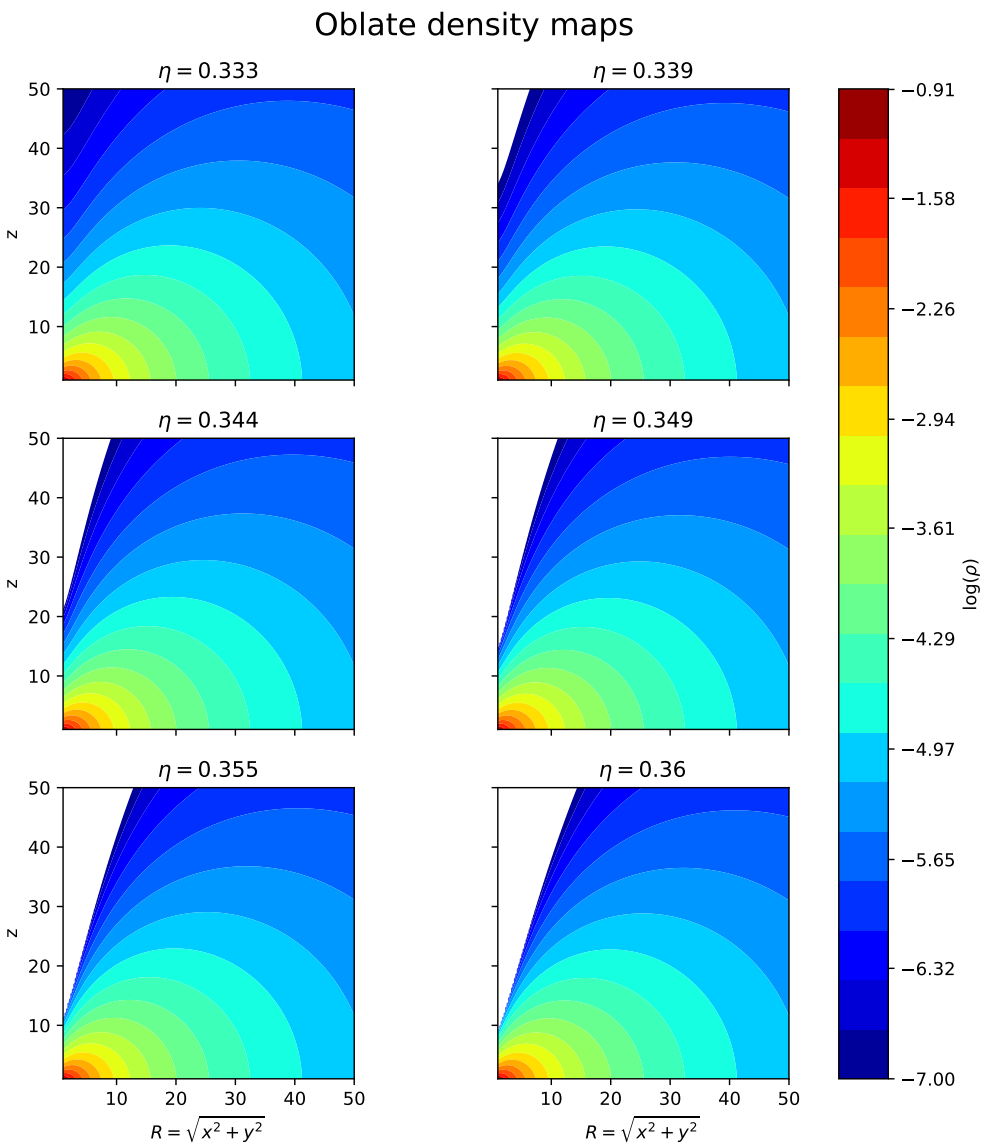

Figure 1.4.: Same as *Figure 1.2*, but for η spanning the range $[1/3; 0.36]$. In the *white* regions the density is negative and thus unphysical.

To find a constraint valid at any point of space on the subtraction of density, we substitute the following expression for the second term in the left-hand side (hereafter, LHS) of *Eq.(1.21)*:

$$\sup_{[0;\infty)} \left(\frac{\epsilon\tilde{y}^2 + \eta\tilde{z}^2}{\tilde{r}^2} \left| \frac{d\ln\tilde{\rho}(\tilde{r})}{d\ln\tilde{r}} \right| \right) = \eta \sup_{[0;\infty)} \left| \frac{d\ln\tilde{\rho}(\tilde{r})}{d\ln\tilde{r}} \right|,$$

where $\sup_{[0;\infty)} \frac{\tilde{y}^2+\tilde{z}^2}{\tilde{r}^2} = 1$ in the plane $\tilde{x} = 0$. The equation resulting from this substitution allows us to limit η:

$$\eta A_M \leq 1, \tag{1.22}$$

where

$$A_M := \sup_{[0;\infty)} \left| \frac{\ln(\tilde{\rho}(\tilde{r}))}{d\ln(\tilde{r})} \right| = \sup_{[0;\infty)} |\gamma(\tilde{r})| .$$

$\gamma(\tilde{r})$ is the logarithmic slope of density distribution

$$\gamma(\tilde{r}) := \frac{d\ln\tilde{\rho}}{d\ln\tilde{r}}, \tag{1.23}$$

for the NFW profile

$$\gamma(\tilde{r}) = \tilde{r}^2(1+\tilde{r})^2\left(-\frac{1+3\tilde{r}}{\tilde{r}^2(1+\tilde{r})^3}\right) = -\frac{1+3\tilde{r}}{1+\tilde{r}}. \tag{1.24}$$

To find A_M, we look for maxima and minima of $\gamma(\tilde{r})$ for $\tilde{r}$ in the range $[0;\infty)$. Given that the RHS of *Eq.(1.24)* is a monotonic function of $\tilde{r}$, we evaluate $\gamma(\tilde{r})$ only at extrema of this range:

$$\gamma(\tilde{r}\to 0) = -1 \tag{1.25}$$

and

$$\gamma(\tilde{r}\to \infty) = -3. \tag{1.26}$$

The maximun in absolute value between the RHSs of *Eq.s (1.25)* and *(1.26)* gives us A_M. When dealing with *Eq.(1.18)*, the limit on the ellipticities ϵ and η is from *Eq.(1.22)*

$$\epsilon \leq \eta < \frac{1}{A_M} = \frac{1}{3}. \tag{1.27}$$

In the prolate NFW density distribution $0 < \eta = \epsilon \leq 1/3$ and in the oblate NFW $\epsilon = 0$ and $0 < \eta \leq 1/3$. Given that *Eq.(1.6)* produces a peanut-shape distribution, the ellipticities of isodenses far from the center are $> 1/3$ (see *Figures 1.3* and *1.4* with $\eta = 1/3$ for some examples). We check numerically the limit on η in *Figures 1.3* and *1.4*: only for $\eta \leq 1/3$ there is no unphysical density, while for $\eta > 1/3$ there are unphysical densities along the direction of subtraction of density (as expected from *Eq.(1.18)*).

1.2.3. Flattened potential

In this Section, we construct the potential generated by *Eq.(1.18)* to first order in flattening from a homeoidal expansion of NFW potential. For the NFW density profile the integrals in *Eq.s (1.8), (1.9)* and *(1.10)* are

$$\int_{\tilde{r}}^{\infty}\tilde{\rho}(m)m dm = \int_{\tilde{r}}^{\infty}\frac{1}{(1+m)^2}dm = -\left[\frac{1}{1+m}\right]_{\tilde{r}}^{\infty} \tag{1.28}$$

and

$$\int_0^{\tilde{r}}\tilde{\rho}(m)m^4 dm = \int_0^{\tilde{r}}\frac{m^3}{(1+m)^2}dm. \tag{1.29}$$

It is useful to rewrite the numerator in the RHS of *Eq.(1.29)* as

$$m^3 = m(m+1)^2 - 2m^2 - m = m(m+1)^2 - 2(m+1)^2 + 3m + 2 = m(m+1)^2 - 2(m+1)^2 + 3(m+1) - 1.$$

We integrate the RHS of *Eq.(1.29)*, substituting the above expression for m^3:

$$\begin{aligned}\int_0^{\tilde{r}}\frac{m^3}{(1+m)^2}dm &= \int_0^{\tilde{r}}\left(m - 2 + \frac{3}{(1+m)} - \frac{1}{(m+1)^2}\right)dm = \\ &= \left[\frac{m^2}{2} - 2m + 3\ln(m+1) + \frac{1}{m+1}\right]_0^{\tilde{r}}.\end{aligned} \tag{1.30}$$

After substituting *Eq.s (1.29)* and *(1.30)* into *(1.9)* and *(1.10)*, respectively, the first-order terms are

$$\tilde{\Phi}_1(\tilde{r}) = -\frac{1}{6\tilde{r}} + \frac{2}{3\tilde{r}^2} - \frac{\ln(1+\tilde{r})}{\tilde{r}^3} - \frac{1}{3\tilde{r}^3(\tilde{r}+1)} + \frac{1}{3\tilde{r}^3} - \frac{1}{3(1+\tilde{r})} \tag{1.31}$$

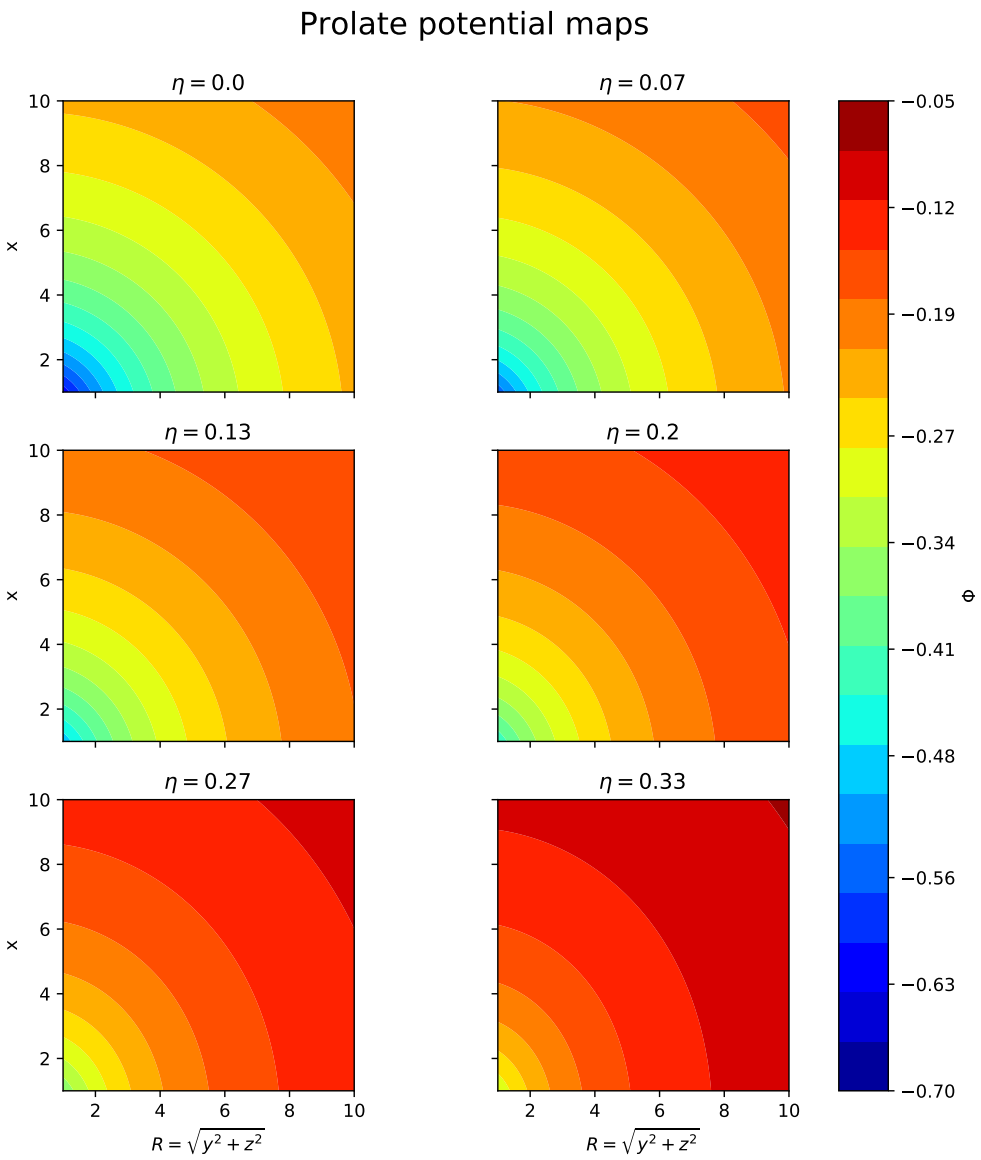

Figure 1.5.: Maps of dimensionless gravitational potential $\Phi(R/r_s; z/r_s)/(4\pi G\rho_r r_s^2)$ in the meridional plane, for the models shown in *Figure 1.1* (see *Eq.(1.33)*).

and

$$\tilde{\Phi}_2(\tilde{r}) = \frac{1}{2\tilde{r}^3} - \frac{2}{\tilde{r}^4} + \frac{3\ln(1+\tilde{r})}{\tilde{r}^5} + \frac{1}{\tilde{r}^5(\tilde{r}+1)} - \frac{1}{\tilde{r}^5}. \tag{1.32}$$

One can substitute these expressions for the two components of the first-order term in *Eq.(1.7)* to find the homeoidal expansion of NFW potential. Here, we present the potentials generated by the density distributions in *Eq.s (1.19)* and *(1.20)* (some examples of these flattened potentials are in *Figures 1.5* and *1.6*):

- when the subtraction of density occurs in the equatorial plane,

$$\begin{aligned}\tilde{\Phi}_{pro}(\tilde{R};\tilde{x}) = &-\frac{\ln(1+\tilde{r})}{\tilde{r}} + 2\eta[-\frac{1}{6\tilde{r}} + \frac{2}{3\tilde{r}^2} - \frac{\ln(1+\tilde{r})}{\tilde{r}^3} - \frac{1}{3\tilde{r}^3(\tilde{r}+1)} + \\ &+ \frac{1}{3\tilde{r}^3} - \frac{1}{3(1+\tilde{r})} + \frac{\ln(1+\tilde{r})}{\tilde{r}}] + \eta\tilde{R}^2[\frac{1}{2\tilde{r}^3} + \\ &- \frac{2}{\tilde{r}^4} + \frac{3\ln(1+\tilde{r})}{\tilde{r}^5} - + \frac{1}{\tilde{r}^5(\tilde{r}+1)} - \frac{1}{\tilde{r}^5}],\end{aligned} \tag{1.33}$$

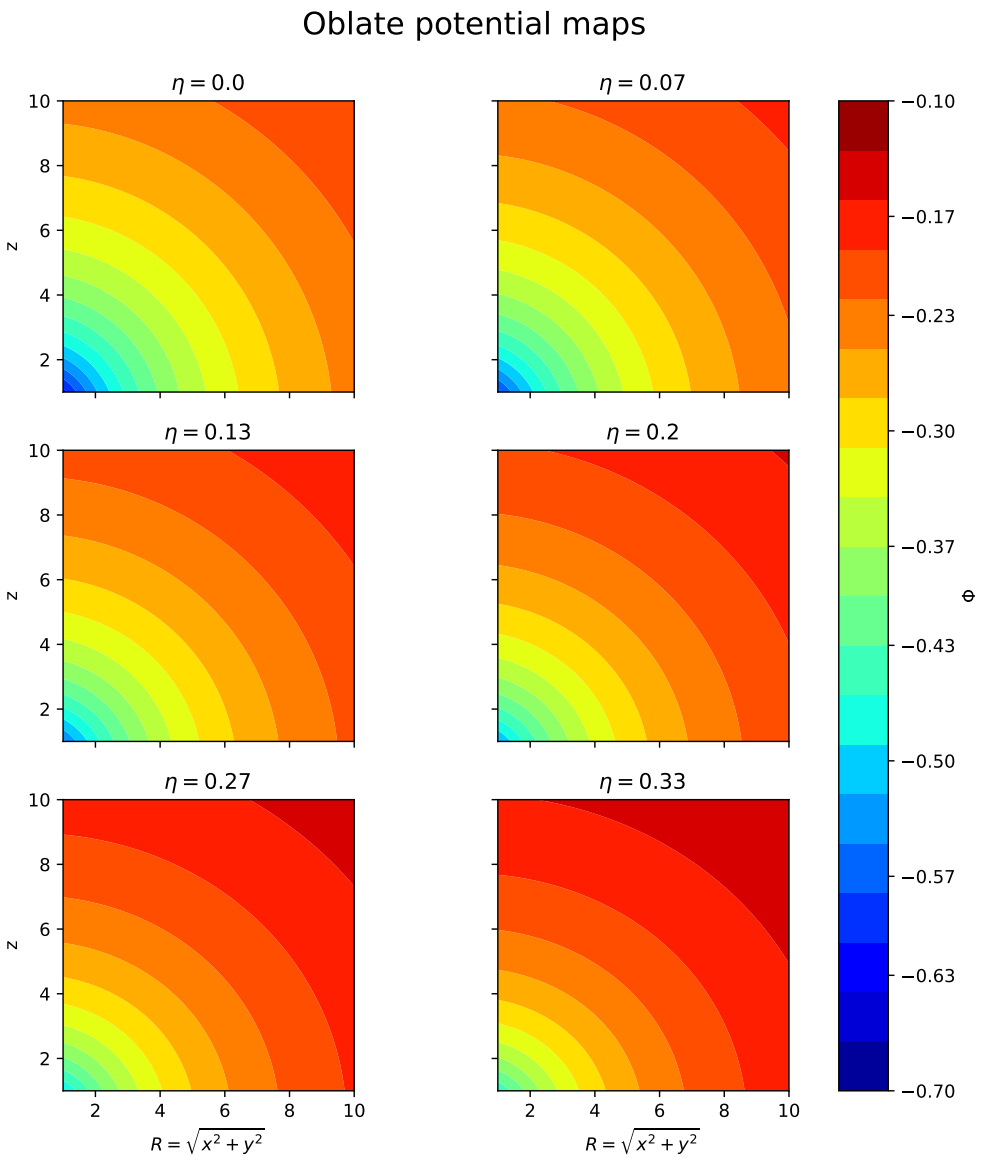

Figure 1.6.: Same as *Figure 1.6*, but for the models shown in *Figure 1.2* (see *Eq.(1.34)*).

where $\tilde{R} := \sqrt{\tilde{y}^2 + \tilde{z}^2}$ is the radius in the equatorial plane (defined as $\tilde{x} = 0$) and $\tilde{x}$ the symmetry axis;

- when the subtraction of density occurs along the symmetry axis,

$$\begin{aligned}\tilde{\Phi}_{obla}(\tilde{R};\tilde{z}) = &-\frac{\ln(1+\tilde{r})}{\tilde{r}} + \eta[-\frac{1}{6\tilde{r}} + \frac{2}{3\tilde{r}} - \frac{\ln(1+\tilde{r})}{\tilde{r}^3} - \frac{1}{3\tilde{r}^3(1+\tilde{r})} + \\ &+ \frac{1}{3\tilde{r}^3} - \frac{1}{3(1+\tilde{r})} + \frac{\ln(1+\tilde{r})}{\tilde{r}}] + \eta\tilde{z}^2[\frac{1}{2\tilde{r}^3} + \\ &- \frac{2}{\tilde{r}^4} + \frac{3\ln(1+\tilde{r})}{\tilde{r}^5} + \frac{1}{\tilde{r}^5(1+\tilde{r})} - \frac{1}{\tilde{r}^5}],\end{aligned} \tag{1.34}$$

where $\tilde{z}$ is the symmetry axis and $\tilde{R} = \sqrt{\tilde{x}^2 + \tilde{y}^2}$ the radius in the equatorial plane (defined as $\tilde{z} = 0$).

As we note in *Figures 1.5* and *1.6*, given that the gravitational potential depends on the entire distribution of density, there is everywhere a decrease of the gravitational potential for

increasing η due to the subtraction of density and an ellipticity of gravitational potential $< \eta$. If the subtraction of density follows no preferential direction, the density and the generated gravitational potential would be spherical; however, the directional subtraction of density breaks also the spherical symmetry of the gravitational potential. Indeed, in *Figures 1.5* and *1.6* we note the elongation of the gravitational potential along the unperturbed axis as well as in the density maps.

1.2.4. Profiles of the flattened gravitational field

We report some useful expressions for deriving the gravitational fields generated by the density distributions in *Eq.s (1.19)* and *(1.20)*, using s as the independent variable:

$$\frac{d}{ds}\frac{\ln(1+s)}{s} = \frac{1}{s(1+s)} - \frac{\ln(1+s)}{s^2},$$

$$\frac{d}{ds}\frac{1}{s^3(1+s)} = -\frac{3}{s^4(1+s)} - \frac{1}{s^3(1+s)^2}$$

and

$$\frac{d}{ds}\frac{\ln(1+s)}{s^3} = \frac{1}{(1+s)s^3} - 3\frac{\ln(1+s)}{s^4}.$$

The gravitational field of the spherical NFW is $\tilde{\mathbf{g}}_{NFW} = (\tilde{g}_{NFW,\tilde{r}}; \tilde{g}_{NFW,\phi}; \tilde{g}_{NFW,\theta})$ in spherical coordinates, where

$$\tilde{g}_{NFW,\tilde{r}}(\tilde{r}) = -\frac{d\tilde{\Phi}_0(\tilde{r})}{d\tilde{r}} = \frac{1}{(1+\tilde{r})\tilde{r}} - \frac{\ln(1+\tilde{r})}{\tilde{r}^2} \tag{1.35}$$

and $\tilde{g}_{NFW,\phi} = \tilde{g}_{NFW,\theta} = 0$.
The gravitational field that is a vector ($\tilde{\mathbf{g}} := (\tilde{g}_{\tilde{R}}; \tilde{g}_{\phi}; \tilde{g}_{\tilde{z}})$ in cylindrical coordinates) for an axisymmetric distribution is $\tilde{\mathbf{g}}(\tilde{R}; \tilde{z}) = (\tilde{g}_{\tilde{R}}; 0; \tilde{g}_{\tilde{z}})$. Hereafter, we rename the symmetry axis of the prolate model $\tilde{x}$ as $\tilde{z}$ (*i.e.* we substitue $\tilde{z}$ for $\tilde{x}$ in *Eq.s (1.19)* and *(1.33)*). The profiles of $\tilde{R}$- and $\tilde{z}$- components of the gravitational field in the meriodional plane are:
when the density subtraction occurs along the symmetry axis

$$\begin{aligned}\tilde{g}_{obla,\tilde{R}}(\tilde{R};0) = -\frac{d\tilde{\Phi}_{obla}(\tilde{R};0)}{d\tilde{R}} =& \frac{1}{(1+\tilde{R})\tilde{R}} - \frac{\ln(1+\tilde{R})}{\tilde{R}^2} - \eta\left[\frac{1}{6\tilde{R}^2} - \frac{4}{3\tilde{R}^3} - \frac{1}{(1+\tilde{R})\tilde{R}^3} + \right.\\ &+ 3\frac{\ln(1+\tilde{R})}{\tilde{R}^4} + \frac{1}{\tilde{R}^4(1+\tilde{R})} + \frac{1}{3\tilde{R}^3(1+\tilde{R})^2} - \frac{1}{\tilde{R}^4} + \\ &\left. + \frac{1}{3(1+\tilde{R})^2} + \frac{1}{(1+\tilde{R})\tilde{R}} - \frac{\ln(1+\tilde{R})}{\tilde{R}^2}\right]\end{aligned} \tag{1.36}$$

and

$$\begin{aligned}\tilde{g}_{obla,\tilde{z}}(0;\tilde{z}) = -\frac{d\tilde{\Phi}_{obla}(0;\tilde{z})}{d\tilde{z}} =& \frac{1}{(1+\tilde{z})\tilde{z}} - \frac{\ln(1+\tilde{z})}{\tilde{z}^2} - \eta\left[-\frac{1}{3\tilde{z}^2} + \frac{8}{3\tilde{z}^3} + \frac{2}{(1+\tilde{z})\tilde{z}^3} + \right.\\ &- 6\frac{\ln(1+\tilde{z})}{\tilde{z}^4} - \frac{2}{\tilde{z}^4(1+\tilde{z})} - \frac{2}{3\tilde{z}^3(1+\tilde{z})^2} + \frac{2}{\tilde{z}^4} + \\ &\left. + \frac{1}{3(1+\tilde{z})^2} + \frac{1}{(1+\tilde{z})\tilde{z}} - \frac{\ln(1+\tilde{z})}{\tilde{z}^2}\right];\end{aligned} \tag{1.37}$$

when the density subtraction occurs in the equatorial plane

$$\begin{aligned}\tilde{g}_{pro,\tilde{R}}(\tilde{R};0) = -\frac{d\tilde{\Phi}_{pro}(\tilde{R};0)}{d\tilde{R}} =& \frac{1}{(1+\tilde{R})\tilde{R}} - \frac{\ln(1+\tilde{R})}{\tilde{R}^2} - 2\eta\left[-\frac{1}{12\tilde{R}^2} + \frac{2}{3\tilde{R}^3} + \right.\\ &+ \frac{1}{2(1+\tilde{R})\tilde{R}^3} - 3\frac{\ln(1+\tilde{R})}{2\tilde{R}^4} - \frac{1}{2\tilde{R}^4(1+\tilde{R})} + \\ &- \frac{1}{6\tilde{R}^3(1+\tilde{R})^2} + \frac{1}{2\tilde{R}^4} + \frac{1}{3(1+\tilde{R})^2} + \frac{1}{(1+\tilde{R})\tilde{R}} + \\ &\left. - \frac{\ln(1+\tilde{R})}{\tilde{R}^2}\right]\end{aligned} \tag{1.38}$$

and

$$\begin{aligned}\tilde{g}_{pro,\tilde{z}}(0;\tilde{z}) = -\frac{d\tilde{\Phi}_{pro}(0;\tilde{z})}{d\tilde{z}} =& \frac{1}{(1+\tilde{z})\tilde{z}} - \frac{\ln(1+\tilde{z})}{\tilde{z}^2} - 2\eta\left[\frac{1}{6\tilde{z}^2} - \frac{4}{3\tilde{z}^3} - \frac{1}{(1+\tilde{z})\tilde{z}^3}\right.\\ &+ 3\frac{\ln(1+\tilde{z})}{\tilde{z}^4} + \frac{1}{\tilde{z}^4(1+\tilde{z})} + \frac{1}{3\tilde{z}^3(1+\tilde{z})^2} + \frac{1}{\tilde{z}^4} + \\ &\left. + \frac{1}{3(1+\tilde{z})^2} + \frac{1}{(1+\tilde{z})\tilde{z}} - \frac{\ln(1+\tilde{z})}{\tilde{z}^2}\right].\end{aligned} \tag{1.39}$$

As shown by some examples of flattened gravitational field in *Figure 1.7*, the subtraction of density drives the decrease of the magnitude of the gravitational field and the break of the spherical symmetry. However, *Figure 1.7* reveals a feature of non-spherically symmetric density subtraction, which is more significant in the center and for increasing η: a stronger gravitational field along the direction of subtraction of density than along the unperturbed axis.

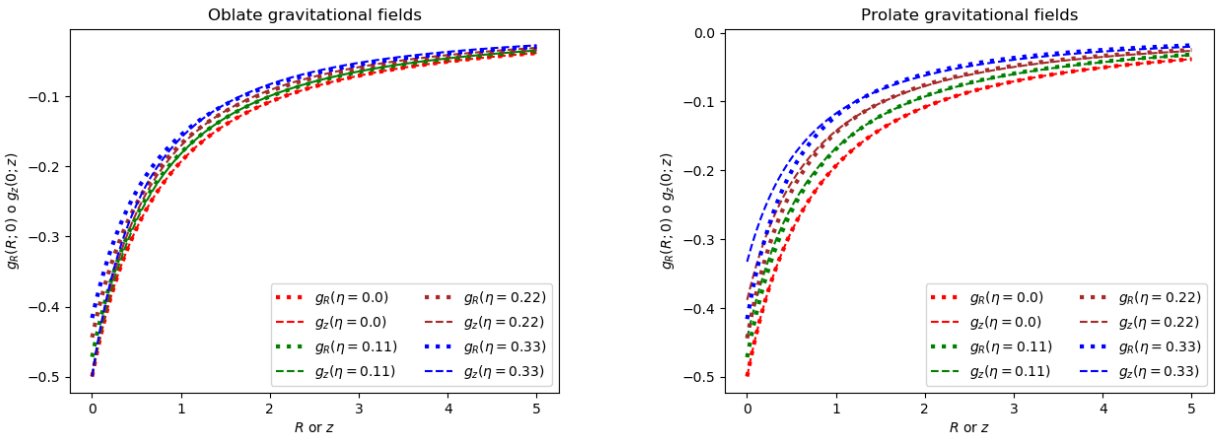

(a) (b)

Figure 1.7.: Profiles of the radial and vertical components of the gravitational field for oblate (left panel) and prolate (right panel) models. $g_R(R/r_s; z/r_s)/(4\pi G\rho_r r_s)$ evaluated at $z = 0$ and $g_z(R/r_s; z/r_s)/(4\pi G\rho_r r_s)$ at $R = 0$ are the dotted and dashed profiles, respectively. η, spanning the range [0;1/3], is associated with the same color in both panels.

1.3. From a generic density-potential pair to a model of halo

1.3.1. Predictions on the internal structure of halos

The depth and the shape of the potential wells that host the ICM are determined not only by the mass of DM halos, but also by their internal structure. Revealing the properties of halos requires to infer the gravitational potential and, consequently, the density profile from the X-ray observations of the ICM and of background lensed sources. However, the biases in the measurements of gravitational field from the X-ray observations (discussed in the Introduction) and the difficulty to recover it over three decades in radius ($\sim 10 - 10^3\,\mathrm{kpc}$) from lensing observations (*e.g. Meneghetti et al. 2010*) make the determinations of the internal structure of halos only from the observations unreliable. Moreover, the difficulty to reproduce the non-gravitational physics in cosmological N-body hydrodynamical simulations suggests us to rely primarily on cosmological DM-only simulations. When dealing with flattened halos, there is no uniquely accepted definition of their mass (see also *Appendix A*). In general, the paradigm used for the description of **statistical properties of halos** in the DM-only simulations measures their mass within spheres and is based on the following parameters.

- The radius r_{200} is usually interpreted as the boundary of a halo and defines the sphere which contains an average density of $200\rho_{crit}(z)$. The mass within the sphere of radius r_{200} is $M_{200} := (4/3)\pi r_{200}^3 200\rho_{crit}(z)$.

- r_{-2} is the radius where the logarithmic slope of spherically averaged density profile is $\gamma(r_{-2}) = -2$. r_{-2} is usually considered the scale radius of halo (in the spherical NFW model $r_s = r_{-2}$).

- The halo concentration is $c_{200} := r_{200}/r_{-2}$.

If the internal structure of halos is universal, we would expect these parameters to be correlated. From the observations (*e.g. Ettori et al. 2010*) and cosmological DM-only simulations there is evidence for a **mass-concentration relation**, which at $z = 0$ is well approximated by a power law (*Dutton & Macciò 2014*)

$$\log c_{200} = 0.905 - 0.101 \log \left(\frac{M_{200}}{10^{12} \times H_0/(100\,\mathrm{km/s/Mpc})\,\mathrm{M}_\odot} \right), \tag{1.40}$$

According to *Eq.(1.40)* c_{200} decreases for increasing mass: the halos over the scales of massive clusters result less concentrated than those of galaxies. The scatter of the mass-concentration relation is well reproduced by a **log-normal distribution** with dispersion $\sigma_{\log c} \simeq 0.11$

$$S(\log c_{200}) = \frac{1}{\sqrt{2\pi}\sigma_{\log c}} \exp \left[-\frac{(\log (c_{200}) - \log (c_{M-c}))^2}{2\sigma_{\log c}^2} \right], \tag{1.41}$$

where c_{M-c} is the centroid of mass-concentration relation and is given by *Eq.(1.40)*.
As well known, in the cosmological framework of bottom-up growth of primordial density perturbations most halos are aspherical. When approximating the halos as ellipsoids, even if the majority of them is triaxial, the fact that the axial ratio of two principal semi-axes measured

in a large sample of halos is close to 1 suggests us to use the spheroidal approximation for the description of these halos. Using the ellipsoidal approximation, in a DM-only simulation *Allgood et al. (2006)* investingate the dependence of the shapes of halos on their mass and measure at an intermediate radius an average **smallest-to-largest axial ratio** $\simeq 0.45$ of halos of $M_{200} \sim 10^{14} - 10^{15}\,\mathrm{M}_\odot$ at $z = 0$.
The predictions just discussed on the internal structure of halos are used in *Section 1.3.2* as constraints on the halo models.

1.3.2. Construction of spheroidal models of halos

In this work we use the spherical, oblate and prolate NFW profiles (derived in *Section 1.2*) to model at redshift $z_0 = 0.05$ typical halos of $M_{200} \simeq 10^{15}\,\mathrm{M}_\odot$ (the spherical model approximates a halo where the smallest-to-largest axial ratio is close to 1). The NFW profiles are parametrized by the density normalization ρ_r, the scale radius r_s and the ellipticity η (we recall that $\eta = 0$ in the spherical NFW). In our flattened models we take the largest possible flattening ($\eta = 1/3$) to be as far as possible consistent with the prediction of *Allgood et al. (2006)* on the shape of halos (see *Section 1.3.1*).

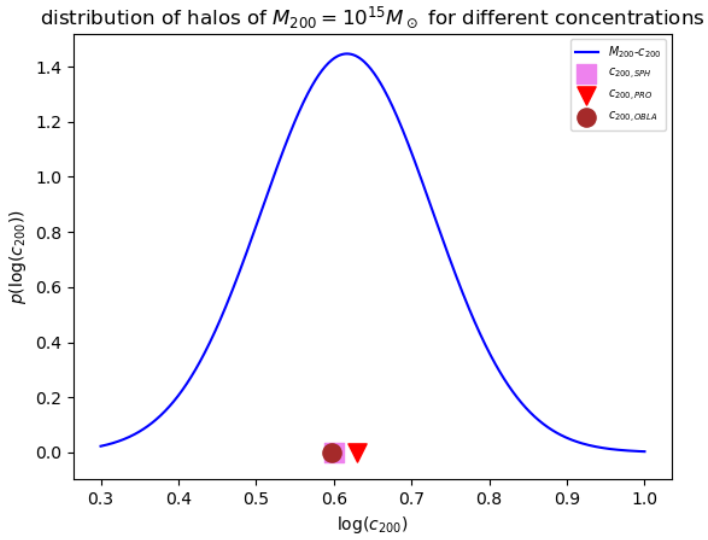

Figure 1.8.: Comparison of the concentrations of our spherical, oblate and prolate models (square, point and triangle, respectively) with the distribution of concentrations (blue curve) inferred from the mass-concentration relation (the combination of *Eq.s (1.40)* and *(1.41)*) for halos of $M_{200} = 10^{15} M_\odot$.

The method to construct a halo model based on the spherical NFW (in this work, called *DMN*) is analytic. We assume $M_{200} = 10^{15}\,\mathrm{M}_\odot$ and a concentration in agreement with the mass-concentration relation of *Dutton & Macciò (2014)* (see *Figure 1.8*; in the spherical model $c_{200} = 3.98$). Recalling that $r_s = r_{-2}$, we get $r_s = r_{200}/c_{200}$, where

$$r_{200} = \left[\frac{M_{200}}{(4/3)\pi 200 \rho_{crit}(z)}\right]^{1/3}, \tag{1.42}$$

and we infer ρ_r from $c_{200} = r_{200}/r_{-2}$ as

$$\rho_r = \frac{200}{3}\frac{\rho_{crit}(z) c_{200}^3}{\ln(1+c_{200}) - \frac{c_{200}}{1+c_{200}}}.$$

Despite conceptually equal to the spherical case, the method to construct spheroidal halo models based on the prolate and oblate NFWs is not exact: the difficulty is to find an analytic expression of the mass of the aspherical NFW in spherical coordinates. Indeed, the mass of an axisymmetric NFW within the sphere of radius r is

$$M(<r) := 4\pi \int_0^r \left(\int_0^{\sqrt{r^2-z^2}} \rho(R;z) R dR \right) dz, \tag{1.43}$$

where $\rho(R;z)$ is given by *Eq.s (1.19)* or *(1.20)* for the prolate and oblate NFWs, respectively (we recall that in *Eq.(1.19)* we substitute $\tilde{z}$ for $\tilde{x}$). We thus compute r_{200} and r_{-2} in the following way. The average density within the sphere of radius r is

$$\langle\rho\rangle(<r) := \frac{3M(<r)}{4\pi r^3}, \tag{1.44}$$

where $M(<r)$ is given by *Eq.(1.43)*. While, the spherically averaged density profile is

$$\rho_{shell}(r) := \frac{3[M(<r+\Delta r/2) - M(<r-\Delta r/2)]}{4\pi[(r+\Delta r/2)^3 - (r-\Delta r/2)^3]}, \tag{1.45}$$

where Δr is the thickness of the spherical shell centered on a radius r (see *Appendix A* for the departure of spherically averaged density profile from the NFW). We compute r_{200} as the radius r where $\langle\rho\rangle(<r) \simeq 200\rho_{crit}(z)$ (with $\langle\rho\rangle(<r)$ given by *Eq.(1.44)*) and r_{-2} as the radius r where

$$\frac{d\ln(\rho_{shell})}{d\ln r} \simeq -2, \tag{1.46}$$

and $\rho_{shell}(r)$ is given by *Eq.(1.45)*.
To build the flattened halo models based on oblate and prolate NFWs (called, in this work, *DMO* and *DMP*, respectively), we select a combination of ρ_r and r_s for which $M(<r_{200}) \simeq 10^{15}\,\mathrm{M}_\odot$, where $M(<r_{200})$ is given by *Eq.(1.43)* with $r = r_{200}$. Then, once computed r_{200} and r_{-2} (see above), we evaluate $c_{200} = r_{200}/r_{-2}$ and compare in *Figure 1.8* the concentrations of our flattened models ($3.5 < c_{200} < 4.5$) to the mass-concentration relation of *Dutton & Macciò (2014)*.
In *Figure 1.9* we plot the profiles of density and potential of our models of $M_{200} \simeq 10^{15}\,\mathrm{M}_\odot$, using *Eq.s (1.19)*, *(1.33)*, *(1.20)* and *(1.34)* with the parameters of *Table 1.1* (we recall that in *Eq.s (1.19)* and *(1.33)* we substitute $\tilde{z}$ for $\tilde{x}$).

Model	Density-potential pair	$\rho_r(\mathrm{g/cm^3})$	$r_s(\mathrm{kpc})$	$r_{-2}(\mathrm{kpc})$	$r_{200}(\mathrm{kpc})$
DMN	Spherical NFW	4.8×10^{-26}	519	519	2067
DMP	Prolate NFW with $\eta = 1/3$	4.8×10^{-26}	700	487	2077
DMO	Oblate NFW with $\eta = 1/3$	4.6×10^{-26}	600	522	2066

Table 1.1.: Parameters of DM halo models.

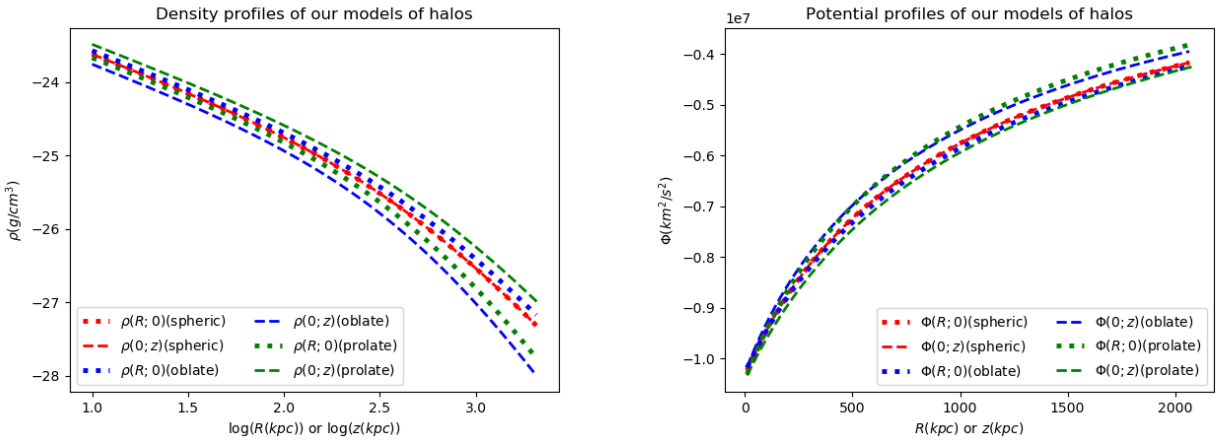

(a) (b)

Figure 1.9.: Profiles of the density (left panel) and of the gravitational potential (right panel) of our models of halos in the meridional plane. We plot $\rho(R; z)$ and $\Phi(R; z)$ evaluated both at $z = 0$ (dotted cruves) and at $R = 0$ (dashed cruves). The same color in both panels refers to the same model.

Chapter 2

Intrinsic properties of the ICM in cool-core cluster models

The ICM in cool-core clusters is believed to be largely in **hydrostatic equilibrium**, however a significant **rotation** is expected from the numerical hydrodynamical simulations (*e.g. Nagai et al. 2007b, Nagai et al. 2013*). It is possible that the tension between mass estimators (*i.e.* the problem of hydrostaic mass bias, discussed in the Introduction; *e.g. Meneghetti et al. 2010, Pratt et al. 2019*) is partly due to ICM rotation. In this Chapter, to explore different kinematic conditions of the ICM and/or different shapes of DM halos (built in *Chapter 1*), we construct six polytropic models of the ICM.
As usual, we describe the ICM as a **collisional inviscid perfect plasma**. Even though the mean free path of electrons of the unmagnetised ICM, known as **Spitzer's Value**, is $\sim$ 10-30 kpc (thus small, but not negligible), we expect that the magnetic fields suppress the mean free path of electrons of the ICM down nearly to **Larmor's radius** $\sim 10^3$-10^5 km. In this case, the mean free path is much smaller than the lengthscale of the system and the collisional approach to the study of the ICM is justified. Given that the length scale of the system is much larger than the **Debye's length** ($\sim$ 10-100 km), no electrostatic field of charges are able to influence the evolution of the ICM. Moreover, the magnetic fields are dynamically unimportant: the ratio between thermal and magnetic pressures is $\sim$ 10-100 for $B \sim 1\,\mu$G (a typical intensity of magnetic field measured in galaxy clusters; e.g. *Bruggen 2013*).

This Chapter is organised as follows. In *Section 2.1.2* we discuss the universal profiles of thermodynamic quantities of the ICM, in *Sections 2.2.3* and in *2.3.3* we present our static and rotating models of the ICM, respectively.

2.1. Predictable behavior of the thermodynamic properties of the ICM

The paradigm used for the description of the universal thermodynamic profiles of the ICM is based on the following quantities. r_Δ is the radius of the sphere which contains an average density of $\Delta\rho_{crit}(z)$ (where $\Delta \geq 200$), while $M_\Delta := (4\pi/3)r_\Delta^3\Delta\rho_{crit}(z)$ is the mass of halo within the sphere of radius r_Δ (for the definition of the mass of aspherical halo models, see

Section 1.3.2 and also *Appendix A*). In this paradigm, at fixed redshift z, r_Δ^3 thus is a proxy of M_Δ. Assuming the cosmic baryon fraction ($f_b = 0.16$) throughout the cluster, the average mass density of the ICM within the sphere of radius r_Δ depends only on $\Delta\rho_{crit}(z)$ and, consequently, the average electron number density of the (fully ionised) ICM within the sphere of radius r_Δ is $\langle n_e \rangle (< r_\Delta) \propto \Delta\rho_{crit}(z)$. Since this Eq. is valid at any $\Delta \geq 200$, the electron number density profile of the ICM in the shell of radius r_Δ can be thought as a function of $E^2(z)$ only:

$$n_e(r_\Delta) \propto E^2(z). \tag{2.1}$$

2.1.1. From a scaling relation to a functional form of the thermodynamic properties

The gas infalling into a massive DM halo is expected to be heated via **adiabatic strong shocks**. In an entirely pressure-supported massive cluster under the assumption of self-similarity, the **Virial Theorem** implies the following relation between the temperature of the ICM T_Δ and the virial mass of the cluster M_Δ (*e.g. Voit 2005*):

$$T_\Delta \propto M_\Delta^{2/3} E^{2/3}(z). \tag{2.2}$$

$T_\Delta := T(r_\Delta)$ is the temperature of the ICM in the spherical shell of radius r_Δ, even though the X-ray observations usually associate T_Δ with a global temperature of clusters (see *Section 3.2.3*).
Using *Eq.(2.1)*, for a perfect fully ionised gas we rewrite *Eq.(2.2)* as

$$p_\Delta \propto M_\Delta^{2/3} E^{8/3}(z), \tag{2.3}$$

where $p_\Delta := p(r = r_\Delta)$ is the pressure of the ICM in the shell of radius r_Δ.
From the observations there is a clear evidence that in massive cool-core clusters only in intermediate regions centred around r_{500} the ICM is fully in equilibrium: we expect the ICM dynamics to depend on the prominence of cool core in the center, while on the continuous interplay between cluster and its surroundings in the outskirts. In the spherical shell of radius r_{500} the predicted mass-temperature and mass-pressure relations are (*Ghirardini et al. 2019*)

$$T_{500} = 8.85\,\mathrm{keV} \left(\frac{M_{500}}{10^{15}\,\mathrm{M}_\odot} E(z) \right)^{2/3} \tag{2.4}$$

and

$$p_{500} = 3.426 \times 10^{-3}\,\mathrm{keV} \times \mathrm{cm}^{-3} \left(\frac{M_{500}}{10^{15}\,\mathrm{M}_\odot} \right)^{2/3} E(z)^{8/3}, \tag{2.5}$$

respectively.
In real clusters a scaling relation is found between M_{500} and T_{500} closely resembling *Eq.(2.4)* (see *Section 3.2.3*). In this Chapter we ignore the observed deviation from *Eq.(2.4)*. At fixed z, T_{500} or p_{500} depend only on M_{500}, so T_{500} and p_{500} are known as mass proxies. However, the presence of a non-thermal support (due to the rotation or to the turbulence) causes an underestimate of mass recovered for a given T_{500} or p_{500} by means of *Eq.s (2.4)* or *(2.5)*, respectively, because T_{500} and p_{500} refer only to the thermal support.
If a mass-temperature relation or a mass-pressure relation are observed at any radius r_Δ, the thermodynamic profiles of the ICM would be tightly universal throughout the cluster. In the

next Section (*2.1.2*) we present the **functional form** $f_Q(x)$ able to reproduce any profile $Q(x)$ of the thermodynamic quantity Q of the ICM in the form of

$$Q(x) = Q_{500} f_Q(x), \tag{2.6}$$

where $x := r/r_{500}$ and Q_{500} is the thermodynamic quantity computed from the *relations (2.4)* or *(2.5)* for $Q = T$ and $Q = p$, respectively. Moreover, the predicted mass-entropy relation, that gives the expected dimensionless entropy (see *Section 2.2.1*) in the shell of radius r_{500}, is reported, *e.g.*, by *Ghirardini et al. 2019*, while Q_{500} for the electron number density is $E(z)^2$ from *Eq.(2.1)*. However, we expect the bulk motions to generate a departure from the universal profiles as well as from the scaling relations. To reconstruct the universal profiles of the thermodynamic quantities of the ICM (see the next Section), *Ghirardini et al. (2019)* thus selected a sample of clusters with low mass biases, *i.e.* a sample where the measurements of mass from the X-ray observations (under the assumption of hydrostatic equilibrium) match those from gravitational lensing to $< 10\%$.

2.1.2. Universal thermodynamic profiles

While *Vikhlinin et al. (2006)* performed one of the first reconstructions of the universal profiles of the thermodynamic quantities of the ICM in real clusters, *Nagai et al. (2007a)* test the reliability of the reconstruction method employed in *Vikhlinin et al. (2006)* via mock observations of clusters from a high-resolution numerical simulation. This analysis demonstrated that the thermodynamic profiles are reconstructed within a few percent. In the last decades several works confirmed the regularity of the thermodynamic profiles of the ICM found by *Vikhlinin et al. (2006)* in real clusters, even if the outermost region of cluster ($r \gtrsim r_{500}$) were remained unexplored. The combination of high quality data of SZE and of X-ray emission provided by PLANCK (`https://www.nasa.gov/mission_pages/planck`) and by XMM-NEWTON, respectively, allowed *Ghirardini et al. (2019)* to reconstruct the universal thermodynamic profiles up to $2r_{500}$ with an unprecedented accuracy. Indeed, *Ghirardini et al. (2019)* combine the X-ray and SZE data in the outskirts of clusters to increase the precision of their measurements while keeping a good control of systematic errors. The sample of clusters used for this reconstruction is the X-COP sample (*Eckert et al. 2017*) that consists of 4 cool-core clusters selected on the basis of signal-to-noise ratio in the PLANCK Sunyaev-Zel'dovich survey (*Planck Collaboration et al. 2014*). In the theoretical studies of the thermodynamic behavior of the palsma, the pressure and the dimensionless entropy (see *Section 2.2.1*) can be thought as the combination of density and temperature. Indeed, even though the thermodynamic quantities are four (density, temperature, pressure and dimensionless entropy), the seed (*i.e.* independent) thermodynamic properties are density and temperature. In this work, we thus use only the functional forms of seed thermodynamic properties of the ICM, even if *Ghirardini et al. (2019)* trace the functional forms of all the thermodynamic quantities. To infer the thermodynamic profiles of the ICM from the observations of cool-core clusters, two of the most reliable observable are the Compton Parameter (see below) related to the SZE and the Emission Measure (see below), which are probes for the pressure and number density of the electrons of the ICM, respectively. Since we observe directly only density and pressure, we perform the reconstruction of the functional forms of density and temperature in the following way.
The **emission measure** ($E.M.$) inferred from the X-ray surface brightness is a probe of density (*e.g. Vikhlinin et al. 2006*):

$$E.M. := \int_{l.o.s.} n_e n_p dl,$$

where n_e and n_p are the number densities of electrons and of protons, respectively, and dl is an infinitesimal length along the line of sight (*l.o.s.*) of the observation. *Ghirardini et al. (2019)* split the X-ray images of clusters into circular concentric annuli, where they evaluated the median of the emission measure to be insensitive to the gas clumps. Then, under the assumption of spherical symmetry they deprojected the $E.M.$ to extract the profile of electron number density. To trace back to the universal profile of density of the ICM in the form of *Eq.(2.6)*, they rescaled by $E(z)^2$ and r_{500} the number density of electrons (n_e) and the deprojection radius r, respectively. The observed profiles of density of the ICM are usually fit by an isothermal β-model (*Cavaliere & Fusco-Femiano 1978*), which, however, misses two well-distinguished signatures: a central cusp and a strongly decreasing slope in the outskirts. The functional form of density, which fits these features, is (see *Vikhlinin et al. 2006* for the complete derivation)

$$f_n(x) = \frac{n_e^2(x)}{E(z)^4} = n_c^2 \frac{\left(\frac{x}{r_c}\right)^{-\alpha}}{\left(1+\frac{x^2}{r_c^2}\right)^{3\beta-\alpha/2}} \frac{1}{\left[1+\left(\frac{x}{r_{ss}}\right)^{\delta}\right]^{\xi/\delta}}, \tag{2.7}$$

where $x := r/r_{500}$ and r_{500} is the radius of the sphere which contains an average density of $500\rho_{crit}(z)$, while the fitting dimensionless parameters n_c, r_c, r_{ss}, β, α and ξ are quoted in *Table 2.1* (*Ghirardini et al. 2019* fix $\delta = 3$ when fitting).
The SZE is a probe of the content of thermal energy residing in the ICM (see the Introduction; *e.g. Nagai et al. 2007a*): in absence of line of sight speed of the ICM (in the CMB rest-frame), the **Compton Parameter** y accounts for the electron pressure (p_e) integrated along the *l.o.s.*, indeed (*Mroczkowski et al. 2019*)

$$y := \frac{\sigma_{Thom}}{m_e c^2} \int_{l.o.s.} p_e dl,$$

where σ_{Thom}, m_e and c are the Thomson cross section, the electron mass and the light speed, respectively.
The spherically averaged pressure profile was thus inferred from the SZE via the deprojection of y in spherical shells of radius r. To trace back to the universal profile of pressure in the form of *Eq.(2.6)*, *Ghirardini et al. (2019)* rescaled r and the pressure p by r_{500} and p_{500} in *Eq.(2.5)*, respectively. *Nagai et al. (2007a)* on the basis of mock observations in a sample of clusters from a high-resolution hydrodynamic simulation concluded that the generalized NFW profile allowed them to closely match the observed profiles of pressure with the results of simulation. The functional form of the pressure based on the generalized NFW is (*Nagai et al. 2007a*)

$$f_p(x) = \frac{p(x)}{p_{500}} = \frac{p_c}{(c_{500}x)^{\chi}[1+(c_{500}x)^{\psi}]^{\frac{\upsilon-\chi}{\psi}}}, \tag{2.8}$$

where $x = r/r_{500}$, p_{500} is given by *Eq.(2.5)* and the fitting dimensionless parameters p_0, c_{500}, χ, ψ and υ are quoted in *Table 2.1*.
To reconstruct the universal profile of temperature in the form of *Eq.(2.6)*, we use

$$T(x) = \frac{p(x)}{n_e(x)}, \tag{2.9}$$

where $x = r/r_{500}$, while $p(x)$ and $n_e(x)$ are given by *Eq.s (2.7)* and *(2.8)*, respectively.

Ghirardini et al. (2019) observed a **scatter** in the universal thermodynamic profiles of the ICM, which reflects the fact that the history of formation of present-day clusters is not unique.

Parameter	CC
n_c	$\exp(-3.9)$
r_c	$\exp(-3.2)$
r_{ss}	$\exp(0.17)$
α	0.80
β	0.49
ξ	4.67
p_0	6.03
c_{500}	1.68
χ	0.51
ψ	1.33
υ	4.37

Table 2.1.: Dimensionless parameters of the functional forms of electron number density (*Eq.(2.7)*) and of pressure (*Eq.(2.8)*) for X-COP sample of cool-core (CC) clusters, taken from *Ghirardini et al. (2019)*.

Parameter	f_n	f_p
σ_1	0.09	0.03
σ_0	0.13	0.00
x_0	0.88	1.52

Table 2.2.: Dimensionless parameters of the intrinsic scatter for X-COP sample of cool-core clusters, taken from *Ghirardini et al. (2019)*. f_n and f_p refer to the functional forms of density and temperature in *Eq.s (2.7)* and *(2.8)*, respectively.

If the non-radiative processes drive the evolution of the ICM, in clusters with low mass biases this scatter is substantially reduced. In the center of clusters where the radiative processes determine the prominence of the cool cores we expect an increase of the scatter, even though the ICM is in equilibrium in time-averaged sense.
Ghirardini et al. (2019) estimate the upper (+) and lower (−) profiles of scatter of the functional form $f_Q(x)$ in the form of

$$S_Q^{\pm}(x) = f_Q(x) \exp[\pm\sigma_{int,Q}(x)], \tag{2.10}$$

where $x = r/r_{500}$ and $Q = p, n_e$. The intrinsic scatter $\sigma_{int,Q}(x)$ follows a **log-parabola**

$$\sigma_{int,Q}(x) = \sigma_1 \log^2\left(\frac{x}{x_0}\right) + \sigma_0, \tag{2.11}$$

where $x = r/r_{500}$, $Q = p, n_e$ and the fitting dimensionless parameters σ_1, σ_0 and x_0 are listed in *Table 2.2*.

The intrinsic scatter that is related to the relative scatter $\sim |S_Q^+(x) - S_Q^-(x)|/f_Q(x)$ (with $Q = n_e, p$) is

- low at $r \simeq r_{500}$ ($\sim 1300\,\mathrm{kpc}$ in *Figure 2.1*) where the radiative processes tend to be unimportant, as predicted in *Section 2.1.1*;
- high in the core (*i.e.* at $r < 400\,\mathrm{kpc}$ in *Figure 2.1*) where the energetic budget of the ICM, which undergoes efficient radiative processes, regulates the decrease of the profile of temperature.

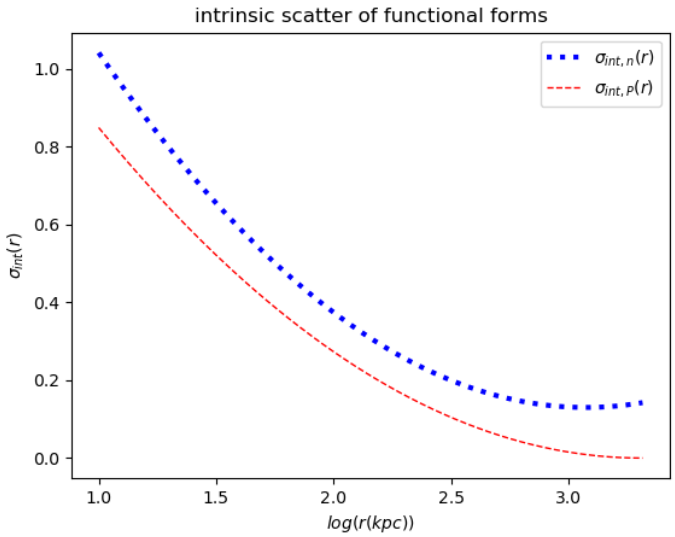

Figure 2.1.: Profile of the intrinsic scatter of the functional forms of the pressure (red dashed curve) and of the density (blue dotted curve) throughout the cluster. We use the parameters of *Table 2.2*, taken from *Ghirardini et al. (2019)*.

Note in *Figure 2.1* that the profile of intrinsic scatter of density and pressure have the same behavior, even though the pressure profile is less scattered throughout the cluster. Furthermore, note that the equilibrium of the ICM (in time-averaged sense) is a necessary, but not sufficient condition for the regularity of its thermodynamic behavior. For the sake of completeness, we report that *Ghirardini et al. (2019)* noted an increase of the intrinsic scatter of the functional forms in the region centred around $2r_{500}$ and they interpreted it as due to the variety of accretion rates.
To estimate the scatter of the universal profile of temperature, we use the scatter propagation

$$\frac{\sigma_T(x)}{T(x)} = \sqrt{\left(\frac{\sigma_p(x)}{p(x)}\right)^2 + \left(\frac{\sigma_n(x)}{n_e(x)}\right)^2}, \tag{2.12}$$

where $x = r/r_{500}$, $\sigma_Q(x) := S_Q^+(x) - S_Q^-(x)$ (with $Q = p, n_e$ and $S_Q^\pm$ given by *Eq.(2.10)*), while $T(x)$, $p(x)$ and $n_e(x)$ are given by *Eq.s (2.9)*, *(2.8)* and *(2.7)*, respectively.

2.2. Hydrostatic equilibrium models of the ICM

2.2.1. The polytropic solution of hydrostatic equilibrium equation

Let us take the equations of the dynamics of an unmagnetised inviscid perfect plasma

$$\frac{\partial \rho}{\partial t} + \nabla \cdot (\rho \mathbf{u}) = 0, \tag{2.13}$$

$$\rho \frac{\partial \mathbf{u}}{\partial t} + (\mathbf{u} \cdot \nabla)\mathbf{u} = -\nabla p - \rho \nabla \Phi_{DM} \tag{2.14}$$

and

$$\frac{p}{\gamma-1}\left[\frac{\partial}{\partial t}+(\mathbf{u}\cdot\nabla)\right]\sigma=-\rho\Gamma-\nabla\cdot\mathbf{Q}. \tag{2.15}$$

ρ rapresents the ICM density (hereafter, the mass density of ICM is called ρ), $\mathbf{u}$ the velocity vector of any fluid element, p its pressure, Φ_{DM} the gravitational potential of cluster and σ the dimensionless entropy (for a perfect gas $\sigma := \ln(p\rho^{-\gamma})$, where γ is the adiabatic index). Moreover, $\mathbf{Q}$ is the **heat conduction flux** and Γ, known as **net energy loss function**, is the net cooling rate of fluid element for unit mass:

$$\Gamma := C - H,$$

where C and H are the cooling and heating rate for unit mass, respectively.
In a typical massive cool-core cluster, to avoid the thermal catastrophe and to maintain the balance between the cooling and heating of the ICM for ~ 10 Gyr as expected from the multiwavelength observations (see the Introduction; *e.g. McDonald et al. 2013* and references therein), we assume Γ such that at any point of cluster $-\rho\Gamma - \nabla\cdot\mathbf{Q} = 0$ if averaged over a sufficiently long time scale. As well known, the thermal conduction cannot be entirely responsibile for maintaining the ICM nearly to the halo virial temperature: the resulting thermal balance of the ICM is necessarily sustained by an additional physical engine (likely the AGN feedback). In order to avoid the description of the complex interplay between heating and cooling, the observed conditions of the ICM (discussed in the Introduction; see *McNamara & Nulsen 2012* for a review) suggest a phenomenological model, where H is a **fixed position-dependent function** (*e.g. Nipoti et al. 2015*; see *McCourt et al. 2012* for a complete description of H), while $\mathbf{Q}$ and C depend on the thermodynamic properties of the ICM.
In our toy model, in absence of efficient net cooling or heating and of significant bulk motions ($\mathbf{u} = 0$) the plasma is in **hydrostatic equilibrium**: the set of fluid dynamic equations (*Eq.s (2.13), (2.14)* and *(2.15)*) is reduced to

$$\frac{1}{\rho}\nabla p = -\nabla\Phi_{DM}. \tag{2.16}$$

Eq.(2.16) describes the balance between the pressure force ∇p and the gravitational force $-\rho\nabla\Phi_{DM}$ per unit volume: the thermal motion of particles (quantified by p) allows the plasma to be in equilibrium into a given potential well.
Solving *Eq.(2.16)* means to find a profile of pressure of the plasma in equilibrium, known as a **distribution**, able to balance a given gravitational potential Φ_{DM}. Given that the pressure is the combination of temperature and of density, the LHS of *Eq.(2.16)* depends on two thermodynamic quantities: T and ρ. Nevertheless, a generic solution of *Eq.(2.16)* is a **barotropic distribution**, where the pressure depends only on the density at any point of space (*e.g. Tassoul 1978*). The temperature and density thus are statified over the gravitational potential.
Let us take a **polytropic distribution**

$$p = p_0\left(\frac{\rho}{\rho_0}\right)^{\gamma'}, \tag{2.17}$$

where γ' is called **polytropic index** (taken positive), while $p_0 := p(\mathbf{x}=\mathbf{x_0})$ and $\rho_0 := \rho(\mathbf{x}=\mathbf{x_0})$ are the pressure and density at a reference point of space $\mathbf{x_0}$, respectively. As a particular case of barotropic distribution, where the pressure depends on ρ as a power law, a polytrope is a solution of *Eq.(2.16)*. From the substitution of *Eq.(2.17)* into *(2.16)*, we get

$$\frac{\gamma' p_0\rho^{\gamma'-1}}{\rho_0^{\gamma'}}d\rho = -\rho d\Phi_{DM}.$$

Eq.(2.16) is vectorial: the direction of ∇p and $-\nabla\Phi_{DM}$ is the same. We thus substitute the differentials instead of gradients to find the above equation. Defining a new variable $a := \rho/\rho_0$, we integrate both sides of this equation:

$$\gamma' \frac{p_0}{\rho_0} \int_1^{\rho(\mathbf{x})/\rho_0} a^{\gamma'-2} da = -\int_{\Phi_0}^{\Phi(\mathbf{x})} d\Phi'.$$

After some algebraic steps, we find for $\gamma' \neq 1$ the expression of the density in a polytropic distribution (in cylindrical coordinates)

$$\rho(R;z) = \rho(\Phi_{DM}(R;z)) = \rho_0 \left[1 - \frac{\gamma'-1}{\gamma'} \frac{\mu m_p}{k_B T_0} (\Phi_{DM}(R;z) - \Phi_{DM,0})\right]^{\frac{1}{\gamma'-1}} \tag{2.18}$$

where $\Phi_{DM,0} = \Phi_{DM}(\mathbf{x} = \mathbf{x_0})$, $T_0 = T(\mathbf{x} = \mathbf{x_0})$, μ is the mean molecular weight and m_p the mass of a proton.
The profile of the temperature of a perfect gas in a polytropic distribution is

$$T = T_0 \left(\frac{\rho}{\rho_0}\right)^{\gamma'-1}. \tag{2.19}$$

As it is clear from *Eq.(2.19)*, the distribution with $\gamma' = 1$ is isothermal (*i.e.* $T(\mathbf{x}) = T_0$ at any point of space $\mathbf{x}$). However, the universal profile of temperature of the ICM suggests that $\gamma' = 1$ is not the best assumption (see, for example, *Figure 2.2*). Limiting ourselves to $\gamma' > 0$, for a declining density distribution of the plasma we distinguish the following solutions:

- for $\gamma' > 1$ the temperature increases inwards;
- for $\gamma' < 1$ the temperature decreases inwards.

For a given gravitational potential Φ_{DM}, a solution of *Eq.(2.18)* with $\gamma' < 1$ has a steeper density profile than with $\gamma' > 1$. For a given Φ_{DM}, the only initial condition of *Eq.(2.18)* is ρ_0: the logarithmic slope of density profile of the plasma is independent of ρ_0, while T_0 and γ' affect this logarithmic slope (see also *Section 2.2.2*).

2.2.2. A simple method to model the cool cores

The energetic budget of the ICM regulates the prominence of a cool core. However, given the difficulty to describe the complex interplay between cooling and heating of the ICM (even via hydrodynamical simulations), we rely on a phenomenological model. From the reconstruction of the thermodynamic profiles of the ICM in cool-core clusters (see the profiles in *Figure 2.2*, for examples), there is a clear evidence that the thermodynamic behavior of the ICM depends on the distance from the center of the cluster: for example, in the cool core the temperature decreases inwards and in the remaining cluster (known as outer region) the temperature decreases outwards. We thus introduce a **break radius** R_{break} to separate the cool core from the outer region. A way to model the ICM in a cool-core cluster is a **two-component composite polytrope** (*e.g. Nipoti et al. 2015*, *Bianconi et al. 2013*), where we take for a spherically symmetric model

- at $r > R_{break}$, $\gamma'_{OUT} > 1$, known as the outer polytropic index;

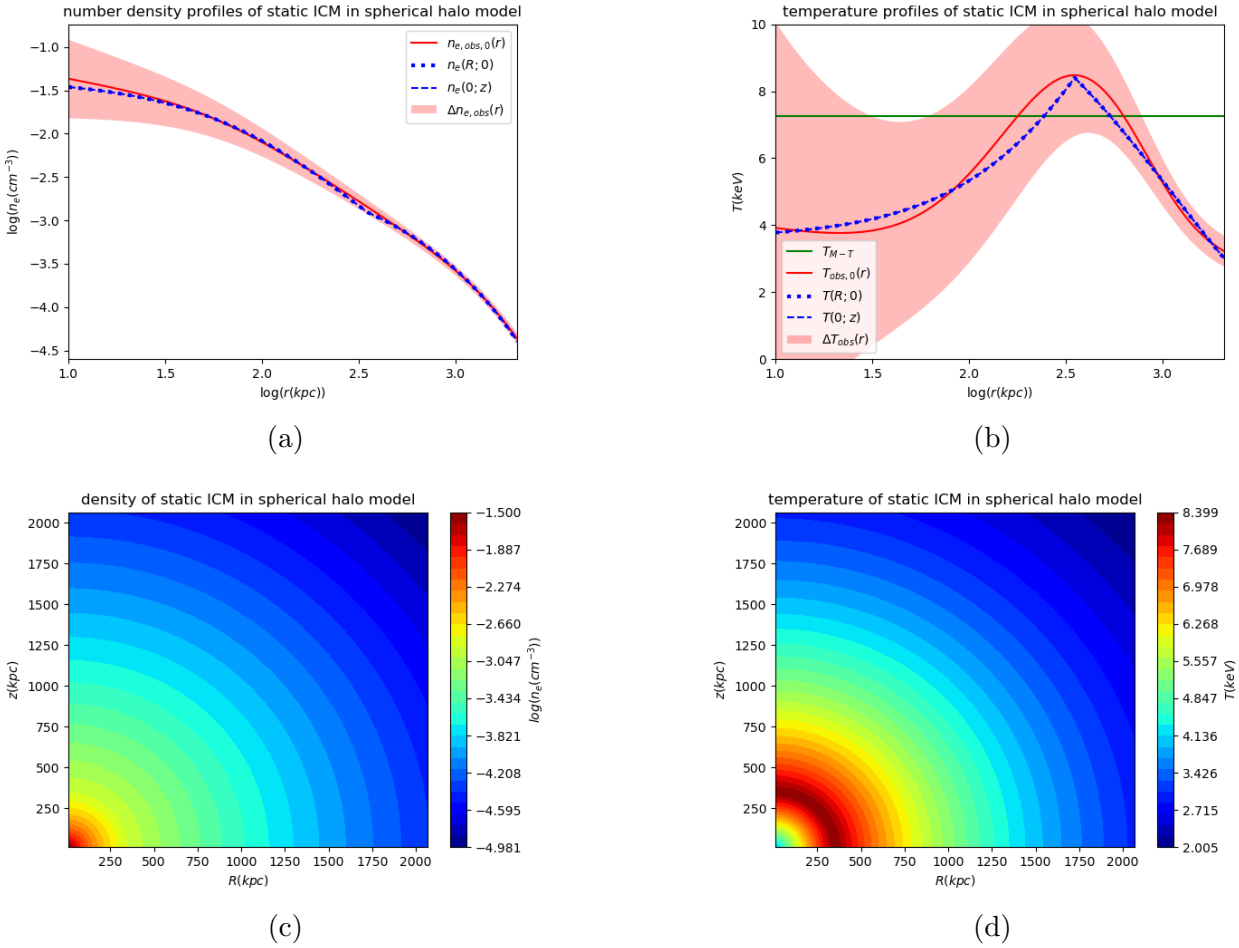

Figure 2.2.: Profiles (upper panels, blue curves) and maps (lower panels) of electron number density (left) and temperature (right) for *NRN* model. In upper panels we plot the average observed profiles (in red; *Ghirardini et al. 2019*) with their scatter (red shaded strip) and the profiles of the model along the vertical (dashed) and radial (dotted) coordinate in the meridional plane. In the upper right panel the green solid line is the global temperature (see *Section 3.2.3* for the discussion of it).

- at $r \leq R_{break}$, $\gamma'_{IN} < 1$, known as the cool-core polytropic index.

R_{break} essentially defines the position of the break in the temperature distribution of the ICM and, consequently, is assumed on the basis of the universal thermodynamic profiles of the ICM (see *Figures 2.3* and, for example, *2.2*).
In *Figure 2.3* the comparison between the logarithmic slopes of the theoretical profiles of model *NRN* (see *Section 2.2.3*) and of the functional forms (in *Section 2.1.2*) representative of the thermodynamic profiles of the ICM in observed clusters shows that this simplified description captures the essential signatures of the ICM in the cool core and in the outer region, such as the positive logarithmic slope of temperature profile in the core (see *Section 2.2.3* for the discussion of logarithmic slopes in the outskirts of clusters). However, the break of the distribution at $r = R_{break}$ implies a departure of the composite polytrope model close to R_{break} from the observed thermodynamic profiles (see, for example, *Figure 2.2*) due to the discontinuity of its logarithmic slope (see *Figure 2.3*).
It is useful to define $\mathbf{x}_0 = (R_{break}; 0)$ in the meridional plane. In absence of spherical symmetry, we trace the break of the distribution of the ICM using the potential difference $\Delta\Phi_{DM}(R; z) := \Phi_{DM}(R; z) - \Phi_{DM}(R_{break}; 0)$. For a gravitational potential increasing outwards (as usual),

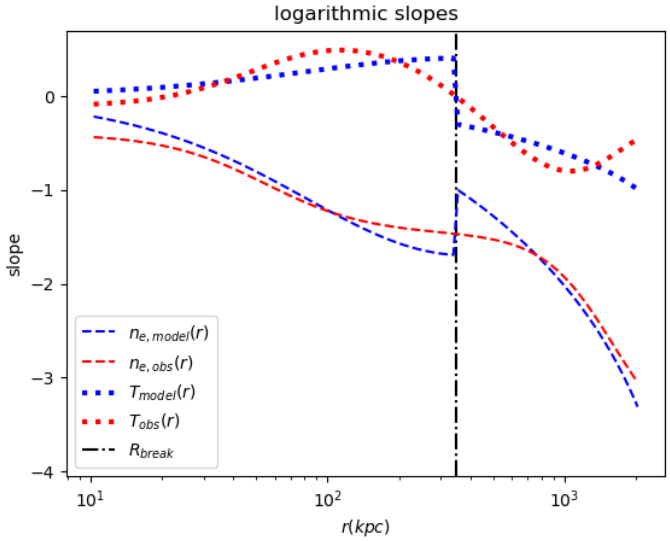

Figure 2.3.: Profiles of logarithmic slopes of ICM density (dashed) and temperature (dotted) for model and observed clusters. The red curves refer to the functional forms representative of observed clusters (see *Section 2.1.2*), while the blue curve to one of our models (in particular to *NRN*; see *Section 2.2.3*). The vertical black dashed line separates the core ($r \leq R_{break}$) from outer region ($r > R_{break}$).

$\Delta\Phi_{DM}(R;z) > 0$ and $\Delta\Phi_{DM}(R;z) \leq 0$ define the outer region and the cool core, respectively. In the meridional plane, the equations giving the density distribution of a two-component composite polytrope model are

- if $\Delta\Phi_{DM}(R;z) > 0$,

$$n(R;z) = n_0 \left[1 - \frac{\gamma'_{OUT} - 1}{\gamma'_{OUT}} \frac{\mu m_p}{k_B T_0} \Delta\Phi_{DM}(R;z)\right]^{\frac{1}{\gamma'_{OUT}-1}} \tag{2.20}$$

  and

$$T(R;z) = T_0 \left(\frac{n(R;z)}{n_0}\right)^{\gamma'_{OUT}-1} \tag{2.21}$$

  where $n(R;z) := \rho(R;z)/(\mu m_p)$ and $n_0 := \rho_0/(\mu m_p)$;

- if $\Delta\Phi_{DM}(R;z) \leq 0$,

$$n(R;z) = n_0 \left[1 - \frac{\gamma'_{IN} - 1}{\gamma'_{IN}} \frac{\mu m_p}{k_B T_0} \Delta\Phi_{DM}(R;z)\right]^{\frac{1}{\gamma'_{IN}-1}} \tag{2.22}$$

  and

$$T(R;z) = T_0 \left(\frac{n(R;z)}{n_0}\right)^{\gamma'_{IN}-1}. \tag{2.23}$$

In a given gravitational potential, T_0, γ'_{OUT} and γ'_{IN} determine the logarithmic slopes of the thermodynamic profiles of ICM models:

- a lower γ'_{OUT} and a higher γ'_{IN} give a lower absolute value of the logarithmic slopes of density and temperature outside and inside the core, respectively;

- even though T_0 represents the normalization of temperature profile, increasing T_0 means to decrease the absolute value of the logarithmic slope of density of the ICM throughout the cluster.

Indeed, for sufficiently low T_0, γ'_{IN} and high γ'_{OUT} the two-component composite polytrope model has a cut-off of density in the outskirts and an infinite slope of density in the center of the cluster. Given that the ICM covers the entire cluster from the center up to r_{200}, we avoid these peculiar behaviors taking for fixed γ'_{OUT} and γ'_{IN}, at any $\Delta\Phi_{DM}(R;z) > 0$,

$$T_0 > \frac{\gamma'_{OUT} - 1}{\gamma'_{OUT}} \frac{\mu m_p \Delta\Phi_{DM}(R;z)}{k_B}$$

and, at any $\Delta\Phi_{DM}(R;z) \leq 0$,

$$T_0 > \frac{|\gamma'_{IN} - 1|}{\gamma'_{IN}} \frac{\mu m_p |\Delta\Phi_{DM}(R;z)|}{k_B}.$$

At the same time, we can interpreted these Eq.s as limits on γ'_{OUT} and γ'_{IN} for a fixed T_0. As we note in *Eq.s (2.20)* and *(2.22)* (see also the above Eq.s), the physical engine that shapes the ICM in our static models is the gravitational potential.

Model	DM halo	$n_0(\mathrm{cm}^{-3})$	T_0(keV)	R_{break}(kpc)	γ'_{IN}	γ'_{OUT}
NRN	DMN	2.4×10^{-3}	8.4	350	0.76	1.30
NRP	DMP	2.5×10^{-3}	9.5	330	0.73	1.42
NRO	DMO	2.3×10^{-3}	9.3	370	0.73	1.35

Table 2.3.: Parameters of static models of ICM. The models of DM halos (second column) refer to *Table 1.1* (*Chapter 1*).

2.2.3. Realistic models of cool-core clusters with static ICM

Given that this work does not focus on a particular cluster, but models the distribution of the ICM in a typical cool-core cluster of $M_{200} \simeq 10^{15}\,\mathrm{M}_\odot$, we assume a typical metallicity observed in the ICM: $Z = 0.3\,\mathrm{Z}_\odot$, where $\mathrm{Z}_\odot$ is the solar metallicity (*Anders & Grevesse 1989*). For a fully ionised gas the corresponding mean molecular weight is $\mu = 0.60$ and the corresponding ratio between the number density of electrons (n_e) and of gas ($n_{gas} := n_e + n_t$, where n_t is the number density of ions) is $n_{gas}/n_e = 1.94$. The universal profiles in *Section 2.1.2* are such that the baryon fraction is $f_b \simeq 0.16$, that is the cosmic value. If the models of the ICM presented below follow the average observed profiles, no additional control over the baryon fraction is necessary here. Using the model of cool-core cluster proposed in *Sections 2.2.1* and *2.2.2* (in particular, using *Eq.s (2.20), (2.21), (2.22)* and *(2.23)*) and assuming the parameters of *Table 2.3*, we build the following distributions of static ICM in cool-core clusters of $M_{200} \simeq 10^{15}\,\mathrm{M}_\odot$: *NRN, NRO* and *NRP* shown in *Figures 2.2, 2.4* and *2.5*, respectively. We note that, even though in this Table R_{break} is different for halos of different shape, the radii of the peak of temperature in all these Figures are similar.
As shown by *Figure 2.3*, in the cluster outskirts the logarithmic slope of the universal profile of temperature increases (and the average observed profiles of temperature tends to be more isothermal than the two-component composite polytrope model; see, for example, *Figure 2.2*). This could be a signature of the matter accretion, even though the intrinsic scatter seemingly does not increase in *Figure 2.1*.

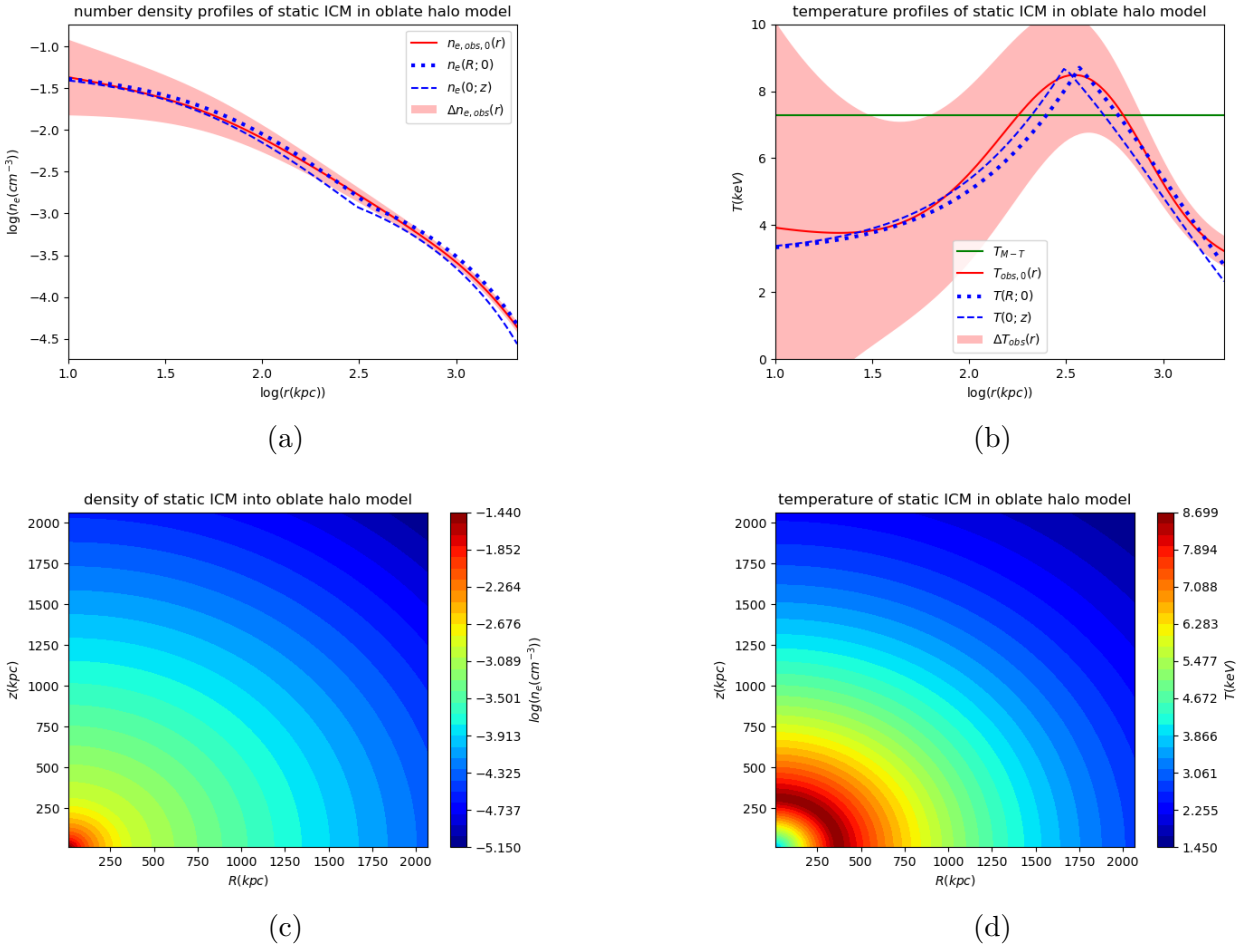

Figure 2.4.: Same as *Figure 2.2*, but for model *NRO*.

Figures 2.2, 2.4 and *2.5* show a good agreement with the average observed profiles of *Ghirardini et al. (2019)*. As discussed in *Ghirardini et al. (2019)*, there is a good agreement among the universal thermodynamic profiles reconstructed by independent groups: it reveals at the same time the regularity of the profiles of the thermodynamic quantities of the ICM and the success of the functional forms of *Ghirardini et al. (2019)* for the description of the thermodynamic properties of the ICM. Consequently, in this work we propose physical models of the ICM, which, being consistent with these functional forms, are expected to be representative of the population of cool-core clusters of $M_{200} \simeq 10^{15}\,M_{\odot}$. Previous works exploited the thermodynamic profiles of *Ghirardini et al. (2019)* assuming spherical symmetry and in the absence of rotation (*e.g. Ettori et al. 2020*). The fact that *NRN*'s model in *Figure 2.2* shows a good agreement with the functional forms of *Ghirardini et al. (2019)* confirms the goodness of these assumptions in the context of the study of the ICM. At the same time, since these assumptions are not always justified, the proposed models with a flattened shape provide an alternative view: a way to shape the distribution of the ICM without spherical symmetry of DM halo. Indeed, even if the aspherical potentials used for these models of the ICM have a more negative slope along the direction of flattening (see *Section 1.2.4* and *Figure 1.7*), we are able to reproduce with a good agreement the average observed profiles of the ICM in cool-core clusters using these spheroidal potentials (with ellipticity of DM isodenses $\simeq 0.3$). On the basis of the results shown by *Figures 2.4* and *2.5* we confirm the possibility that most halos in real galaxy clusters are flattened.

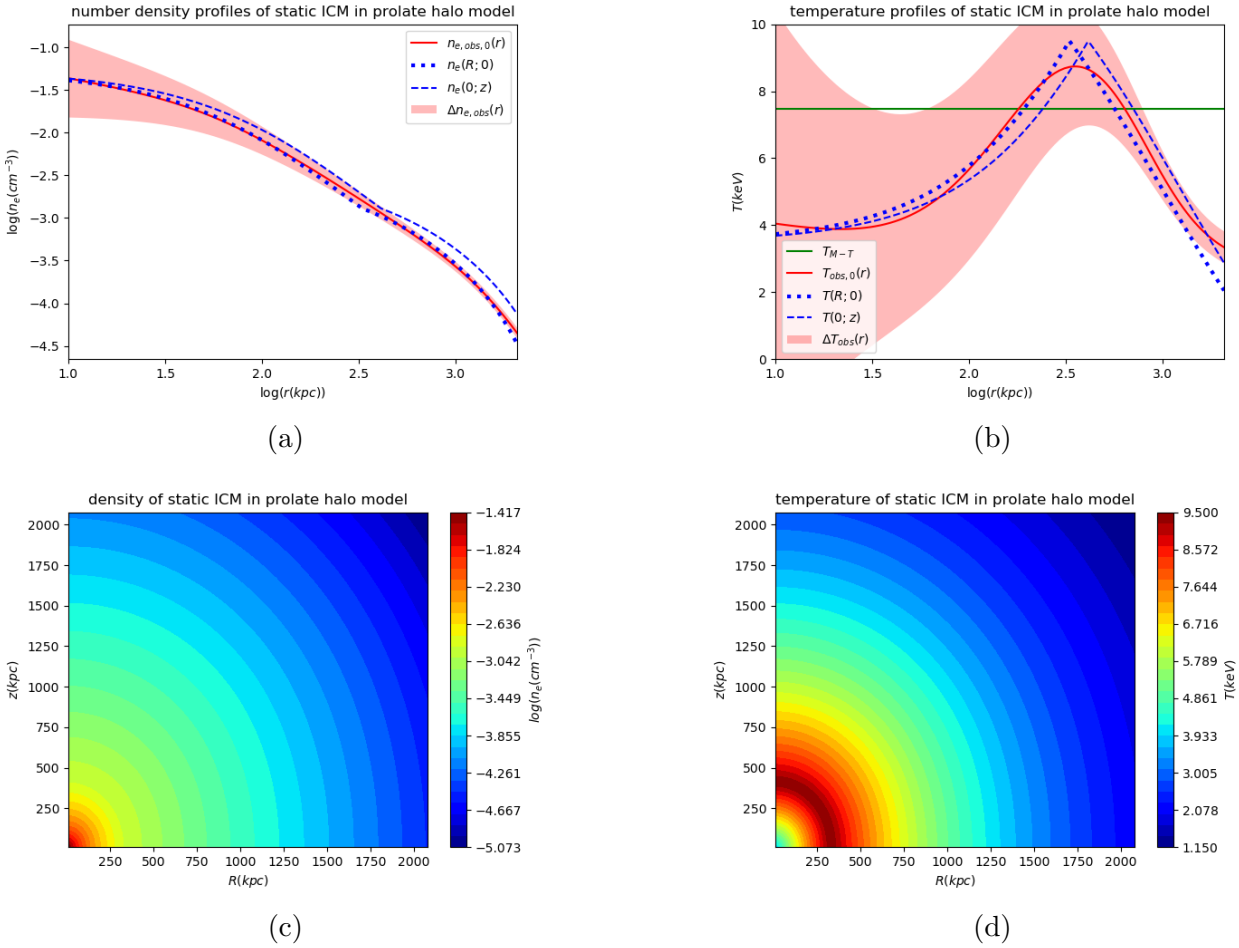

(a) (b)

(c) (d)

Figure 2.5.: Same as *Figure 2.2*, but for model *NRP*.

2.3. Rotating equilibrium models of ICM

2.3.1. The equilibrium of a rotating plasma

Let us take the three components of *Euler's Equation (2.14)* in cylindrical coordinates

$$\frac{\partial u_R}{\partial t} + (\mathbf{u}\cdot\nabla)u_R - \frac{u_R^2}{R} = -\frac{1}{\rho}\frac{\partial p}{\partial R} - \frac{\partial \Phi_{DM}}{\partial R}, \tag{2.24}$$

$$\frac{\partial u_\phi}{\partial t} + (\mathbf{u}\cdot\nabla)u_\phi + \frac{u_R u_\phi}{R} = -\frac{1}{\rho}\frac{1}{R}\frac{\partial p}{\partial \phi} - \frac{1}{R}\frac{\partial \Phi_{DM}}{\partial \phi} \tag{2.25}$$

and

$$\frac{\partial u_z}{\partial t} + (\mathbf{u}\cdot\nabla)u_z = -\frac{1}{\rho}\frac{\partial p}{\partial z} - \frac{\partial \Phi_{DM}}{\partial z}. \tag{2.26}$$

The set of Equations of fluid dynamics for an unmagnetised inviscid perfect plasma is completed by *Eq.s (2.13)* and *(2.15)*.
In a static plasma, even though the particles of any fluid element are in a microscopic random motion that produces the pressure able to maintain this plasma in hydrostatic equilibrium, there is no displacement of a fluid element. In galaxy clusters the numerical simulations predict a bulk velocity field (in cylindrical coordinates) $\mathbf{u} = (u_R; u_\phi; u_z) \neq 0$. In non-relaxed clusters

there are bulk motions with $u_R \neq 0$ and/or $u_z \neq 0$: they involve a transport of mass, linear momentum and energy inwards or outwards, such that the ICM cannot be in equilibrium within the potential well. Moreover, there is no equilibrium of the plasma even in presence of a significant net heating or cooling: for instance, the presence of an important cooling flow implies $u_R, u_z \neq 0$. The clusters where the intensities of u_R and u_z are negligible are called **relaxed**. However, given that from the multiwavelength observations (*e.g. McDonald et al. 2013* and references therein) there is a clear evidence for the equilibrium of the ICM in time-averaged sense in relaxed cool-core clusters (see also *Section 2.2.1* and Introduction), the tension among the mass estimators (*e.g. Pratt et al. 2019*) suggests a departure from the hydrostatic equilibrium induced by additional supports to the thermal pressure of the ICM. A way to account for the departure from the hydrostatic equilibrium is to introduce a significant rotation ($u_\phi = \Omega R \neq 0$ with $\partial/\partial\phi = u_R = u_z = 0$, where $\Omega(R; z)$ is the angular speed; predicted on the basis of hydrodynamic simulations by, *e.g.*, *Nagai et al. 2007a* and *Nagai et al. 2013*) able to balance partly the gravitational potential. The rotating ICM in equilibrium into the potential well of cluster follows a stationary (only $\partial/\partial t = 0$), but not static ($\mathbf{u} = 0$) configuration.
Under the conditions $\partial/\partial t = \partial/\partial\phi = u_z = u_R = 0$, a rotating plasma is in equilibrium into a gravitational potential $\Phi_{DM}(R; z)$ and satisfies

$$\frac{\partial p}{\partial R} = \rho\frac{u_\phi^2(R; z)}{R} - \rho\frac{\partial \Phi_{DM}}{\partial R}, \tag{2.27}$$

$$\frac{\partial p}{\partial \phi} = 0 \tag{2.28}$$

and

$$\frac{\partial p}{\partial z} = -\rho\frac{\partial \Phi_{DM}}{\partial z}. \tag{2.29}$$

A generic rotating fluid in equilibrium into a potential well follows

- a **barotropic distribution**, if the pressure is stratified over density, *i.e.* $p(\mathbf{x}) = p(\rho(\mathbf{x}))$ at any point of space $\mathbf{x}$;

- a **baroclinic distribution**, if the pressure is not stratified over the ICM density.

Starting from *Eq.s (2.27), (2.28)* and *(2.29)*, the **Poincarè-Wavrè Theorem** (*e.g. Tassoul 1978*) states that a gas in a barotropic distribution rotates along cylinders, *i.e.* has $\Omega = \Omega(R)$ (the hydrostatic equilibrium represents a limiting case, where $\Omega(R) = 0$).
Under the assumption of barotropic distribution, the RHS of *Eq.(2.27)* is the combination of the centrifugal acceleration ($= u_\phi(R)^2/R$) and of the R-component of DM gravitational field ($= -\partial\Phi_{DM}/\partial R$). We thus define a vectorial field, known as the **effective gravitational field**, $\mathbf{g_{eff}}(R; z) = (g_{eff,R}; g_{eff,\phi}; g_{eff,z})$ as

$$g_{eff,R} := \frac{u_\phi^2(R)}{R} - \frac{\partial \Phi_{DM}}{\partial R}, \tag{2.30}$$

$$g_{eff,\phi} := 0$$

and

$$g_{eff,z} := -\frac{\partial \Phi_{DM}}{\partial z}. \tag{2.31}$$

Thanks to the definition of $\mathbf{g_{eff}}$, we rewrite the three components of *Euler's Equations (2.27),(2.28)* and *(2.29)* in a vectorial Eq.

$$\nabla p = \rho \mathbf{g_{eff}}, \tag{2.32}$$

where the effective gravitational field plays the same role of DM gravitational field ($= -\nabla\Phi_{DM}$) in *Eq.(2.16)*. The effective gravitational field is usually rewritten as a gradient of a scalar field $\Phi_{eff}(R, z)$:

$$\mathbf{g_{eff}} = -\nabla\Phi_{eff}.$$

Φ_{eff}, known as **effective potential**, represents the combination of axisymmteric gravitational potential $\Phi_{DM}(R, z)$ and of cylindrical rotation: combining the above Equation with *Eq.s (2.30)* and *(2.32)* we get

$$\Phi_{eff}(R, z) = [\Phi_{DM}(R, z) - \Phi_{DM}(R_\star; z_\star)] - \int_{R_\star}^{R} \frac{u_\phi^2(R')}{R'} dR', \tag{2.33}$$

where $(R_\star; z_\star)$ is a reference point.
Note the opposite signs among the two terms in RHSs of *Eq.s (2.33)* and *(2.30)*: the cylindrical rotation balances partly the R-component of the DM gravitational field. When the mass of a galaxy cluster is estimated by assuming the hydrostatic equilibrium (see *Eq.(2.16)*), the presence of a significant rotation in principle causes an underestimate of gravitational potential and, consequently, of the mass of this cluster (see *Eq.(2.33)*; *e.g. Fang et al. 2009*).
Eq.s (2.32) and *(2.16)* are identical, if we substitute Φ_{eff} for Φ_{DM}, so *Eq.(2.18)* with $\Phi_{eff}(R; z)$ instead of $\Phi_{DM}(R; z)$ is a solution also for a rotating plasma in equilibrium into a potential well.

2.3.2. An analytic effective potential

Let us take the rotation law (*Bianconi et al. 2013*)

$$u_\phi^2(S) = u_0^2 \frac{S^2}{(1+S)^4}, \tag{2.34}$$

where $S := R/R_0$, R_0 is a reference radius, u_0 a reference speed and R the radial coordinate in the meridional plane. The features of *Eq.(2.34)* are (see also *Figure 2.6a*)

- a fall in the center, such that $u_\phi(S) \to 0$ when $S \to 0$;
- a peak at intermediate radii ($S \simeq 1$);
- a decrease at large radii, such that $u_\phi(S) \to 0$ when $S \to \infty$.

The free parameters u_0 and R_0 define the tangential speed of the peak of *rotation law (2.34)* and its radius in the equatorial plane, respectively.
We find the analytic solution of the effective potential for the *rotation law (2.34)* in the following way. The integral in the RHS of *Eq.(2.33)* for the *rotation law (2.34)* is

$$\int_{R_\star}^{R} \frac{u_\phi^2(R')}{R'} dR' = \int_{R_\star/R_0}^{S} \frac{S'}{(1+S')^4} dS'. \tag{2.35}$$

Substituting $S' + 1 - 1$ for S' in the numerator of RHS of *Eq.(2.35)* and integrating, we get

$$\int \frac{S+1-1}{(1+S)^4} dS = \int \left(\frac{1}{(1+S)^3} - \frac{1}{(1+S)^4} \right) dS = \frac{1}{3(1+S)^3} - \frac{1}{2(1+S)^2}.$$

Considering $(R_\star; z_\star) = (\infty; 0)$ and $\Phi_{eff}(\infty; 0) = 0$, the effective potential associated with this rotation law is

$$\Phi_{eff}(R; z) = \Phi_{DM}(R; z) - \left[\frac{u_0^2}{3\left(1 + \frac{R}{R_0}\right)^3} - \frac{u_0^2}{2\left(1 + \frac{R}{R_0}\right)^2} \right], \tag{2.36}$$

where $\Phi_{DM}(R; z)$ can be any axisymmetric gravitational potential (for which $\Phi_{DM}(\infty; 0) = 0$).

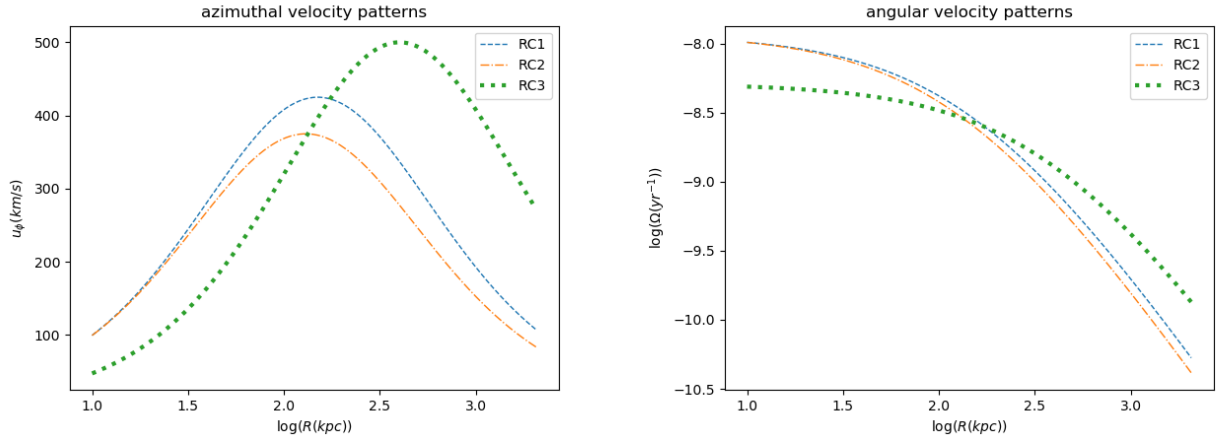

(a) (b)

Figure 2.6.: Profiles of azimuthal speed (left panel) and of angular speed (right panel) of the rotation patterns in *Table 2.4*.

Rotation pattern	u_0(km/s)	R_0(kpc)
RC1	1700	150
RC2	1500	130
RC3	2000	400

Table 2.4.: Parameters of the rotation patterns, associated with *Eq.(2.34)* and used to build the rotating models of the ICM in *Table 2.5*.

2.3.3. Realistic models of cool-core clusters with rotating ICM

Model	DM halo	Rotation pattern	n_0(cm^{-3})	T_0(keV)	R_{break}(kpc)	γ'_{IN}	γ'_{OUT}
RMN	DMN	RC1	2.3×10^{-3}	8.9	350	0.67	1.35
RMO	DMO	RC2	3.0×10^{-3}	8.7	330	0.66	1.33
RMP	DMP	RC3	2.5×10^{-3}	9.0	320	0.70	1.39

Table 2.5.: Same as *Table 2.3*, but for our rotating models of the ICM. The rotation patterns refer to *Table 2.4*.

Assuming the *rotation law (2.34)* and the parameters of *Table 2.4*, we build the rotation patterns *RC1, RC2* and *RC3*, whose azimuthal and angular speeds are plotted in *Figure 2.6*. Note in *Figure 2.6a* that the peak of azimuthal speed of these rotation patterns is $\lesssim 500$ km/s and the peak radius in the equatorial plane is between $\simeq 100$ kpc and $\simeq 400$ kpc. These rotation

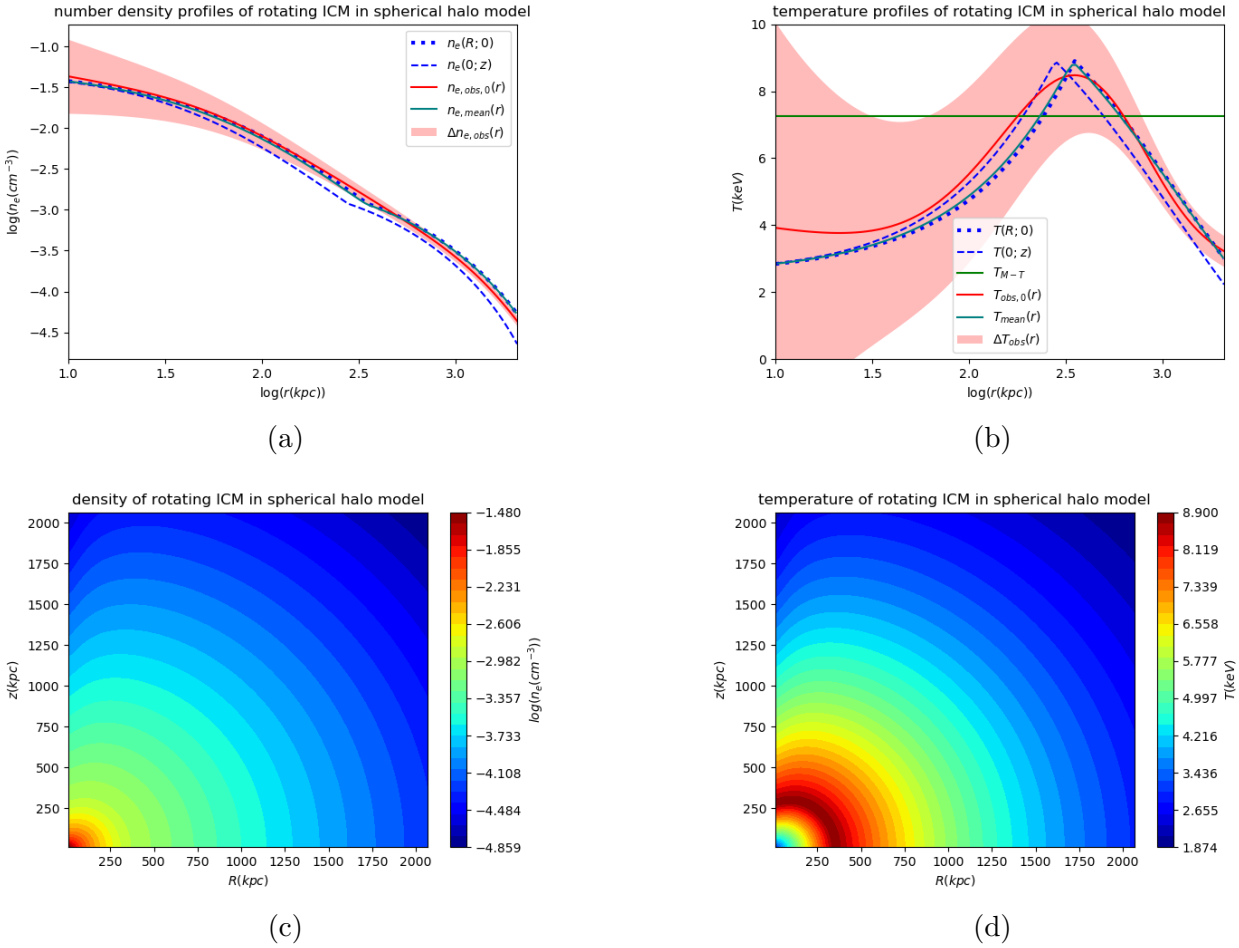

Figure 2.7.: Same as *Figure 2.2*, but for model *RMN*. In the upper panels, using *Eq.(2.37)* with $Q = n_e, T$, we plot the teal solid curves that refer to $n_{e,mean}(r)$ and $T_{mean}(r)$, respectively.

patterns thus are consistent with the spectroscopic results of *Liu & Tozzi (2019)* and the upper limit provided by the measurement of a merger speed (see the Introduction). On the basis of the model of cool-core cluster proposed in *Section 2.2.2* (in particular, *Eq.s (2.20), (2.21), (2.22)* and *(2.23)*) with Φ_{eff} (in this work, *Eq.(2.36)*) instead of Φ_{DM}, using these rotation patterns and assuming the parameters of *Table 2.5*, we build the following polytropic models of rotating ICM in a typical cool-core cluster of $M_{200} \simeq 10^{15}\,\mathrm{M}_\odot$: *RMN, RMO* and *RMP* shown in *Figures 2.7, 2.8* and *2.9*, respectively.
To consistently compare our models of the ICM to the average observed thermodynamic profiles of *Ghirardini et al. (2019)* (see *Section 2.1.2* for the description of the method used by *Ghirardini et al. 2019*) we split the distribution of the ICM into spherical shells. In any shell of volume $V_s := 4/3\pi[(r + \Delta r/2)^3 - (r - \Delta r/2)^3]$ (where r and Δr are the radius and the thickness of the shell, respectively) we compute the average of any thermodynamic quantity $Q(R; z)$ as

$$Q_{mean}(r) := \frac{\int_{V_s} Q(R; z) dV}{V_s}, \tag{2.37}$$

where $Q = n_e, T$.
We recall that the thermodynamic quantities of the plasma are stratified over the effective potential, when the rotation speed is constant on cylinders. Given that this rotation balances partly the R-component of the gravitational field, the distribution of the ICM tends to be peanut-shaped (see *Figures 2.7* and *2.8*) with a depletion of the plasma close to the symmetry

axis. However, for model *RMO* (see *Figure 2.8*), where the rotation speed is lower (see pattern *RC2* in *Figure 2.6a*), also the oblate halo contributes to the elongation of the distribution in the equatorial plane. Actually, the morphology of the ICM is round in the center and peanut-shaped at $r \gtrsim R_0$ (*i.e.* at larger radii than the peak of tangential speed; see *Section 2.3.2* for the definition of R_0). *Figure 2.9* shows a rounder morphology of the ICM, since the rotation on cylinders tends to counteract the depletion of the plasma close to the equatorial plane due to a prolate halo. Even if our models of the ICM are particularly peanut-shaped, we expect the presence of a vertical gradient of azimuthal speed to mitigate this effect in real galaxy clusters.

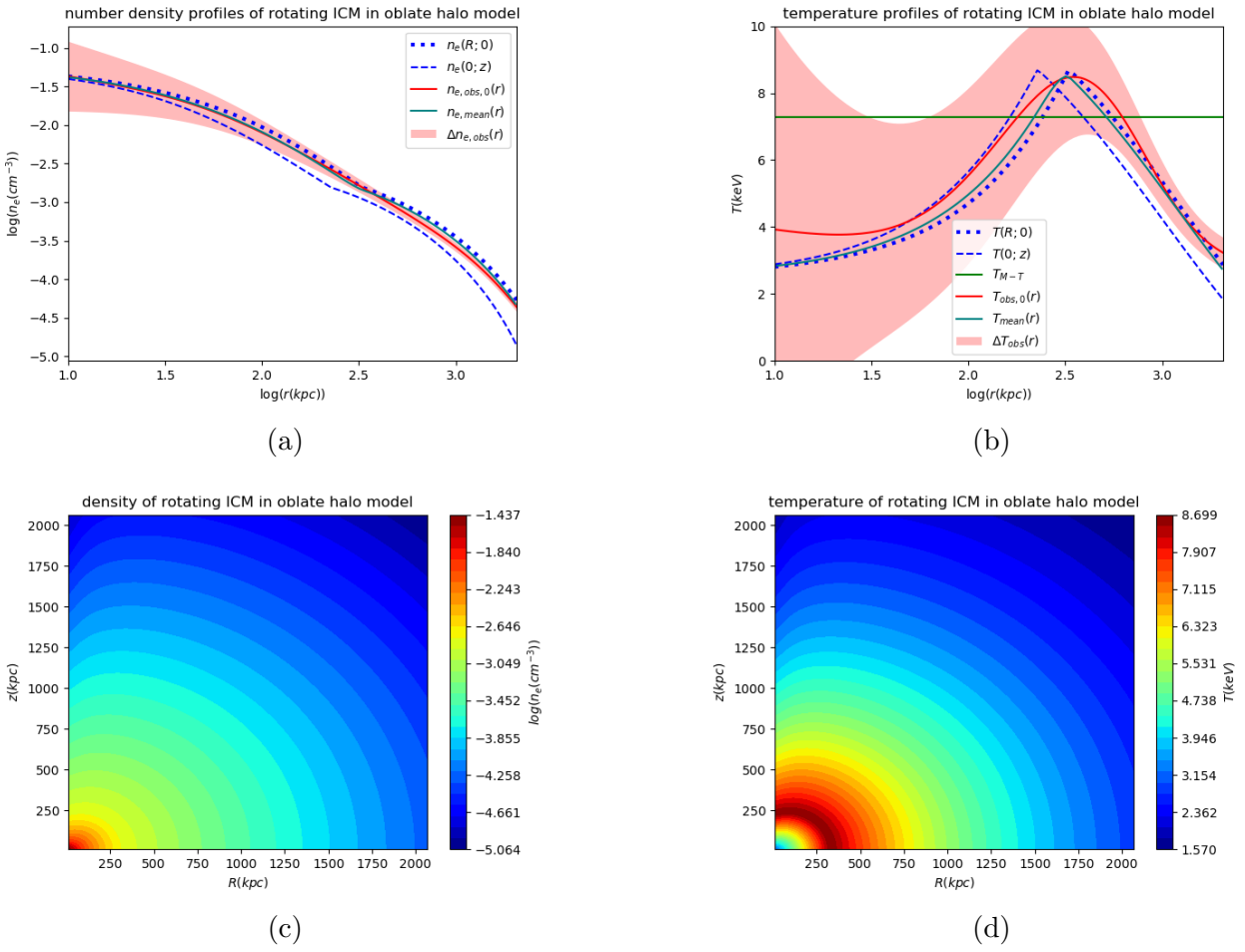

Figure 2.8.: Same as *Figure 2.7*, but for model *RMO*.

Here we use the functional forms of *Ghirardini et al. (2019)* as constraints on the azimuthal speed: the rotation patterns are such that we find an acceptable agreement between our models of the ICM and the average observed profiles. Given that *Ghirardini et al. (2019)* selected a sample of clusters with low mass biases (see *Section 2.1.1*), we expect a modest rotational suppport for the models of the ICM that reproduce fairly well the average observed profiles of *Ghirardini et al. (2019)* (in *Section 2.1.2*). From this comparison, we conclude that there is room for a rotation of $\lesssim 500\,\mathrm{km/s}$ in presence or in absence of DM halo flattening in real clusters. Furthermore, these rotating models of the ICM provide a way to interpret in presence of rotation and, if present, of DM halo flattening the average observed profiles of the ICM representative of the population of cool-core clusters of $M_{200} \simeq 10^{15}\,\mathrm{M}_\odot$.

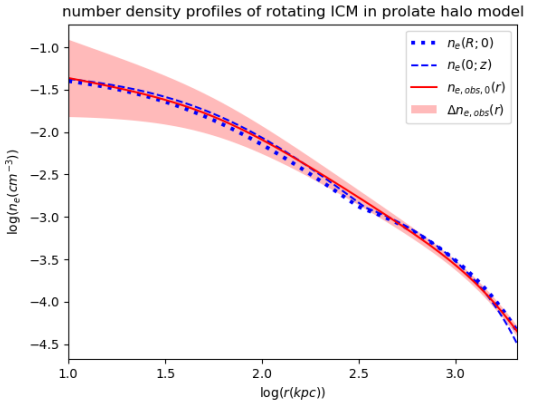

(a)

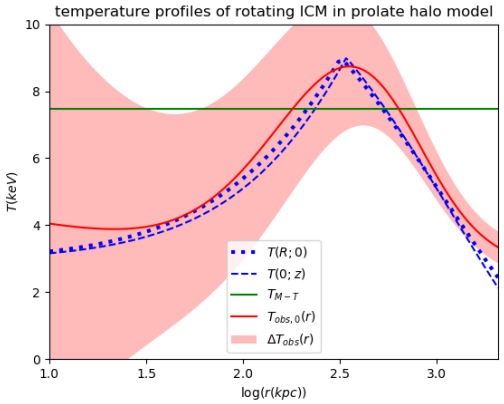

(b)

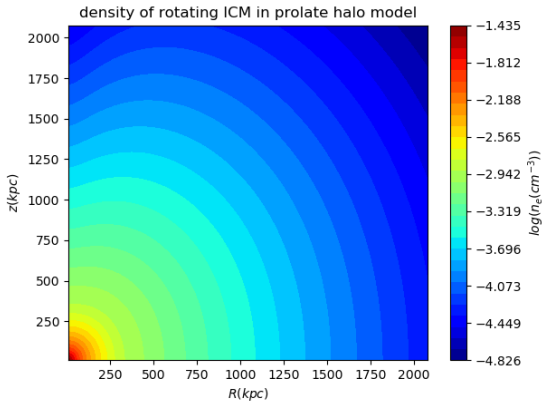

(c)

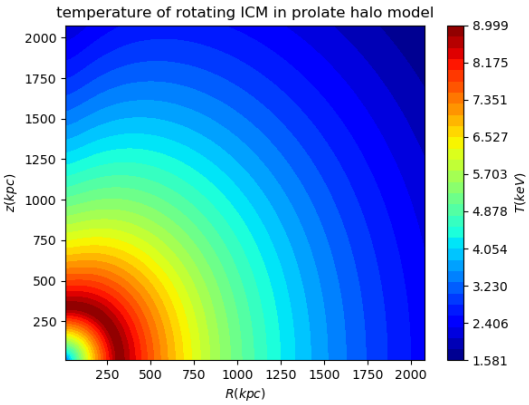

(d)

Figure 2.9.: Same as *Figure 2.2*, but for *RMP*.

Chapter 3

Observables reconstructed from models of the ICM

The high-quality of data and the improvement of computer performance allow us to get the following important milestones in the framework of the **thermal emission of galaxy clusters**. Over the last decade X-ray surveys accurately measured the flattening of isophotes (e.g. *Campitiello et al. 2022*) and the deviation of scaling relations (see, e.g., *Reichert et al. 2011*) from the virial behavior (see *Section 2.1.1*). The last decade simulations and observations showed that the ICM is subject to continuous perturbations (such as feedback from stars and AGN, mergers and matter accretion) able to trigger the **bulk motions of the ICM** (*e.g. Nagai et al. 2013, Vazza et al. 2017* and references therein; see also the Introduction), even if there was thus far an only one detection of a line of sight speed (in the X-ray spectrum of the core of Perseus cluster; *Hitomi Collaboration et al. 2016*). In this Chapter, we use these milestones to test the current photometric limits on the rotation speed of the ICM under different shapes of the halos (*Section 3.1*) and to probe via mock observations with the new generation facilities the future spectroscopic perspectives in the X-rays on the detectability of the kinematic signatures of the ICM: in particular, on the Doppler shift of emission line centroids (*Section 3.2*).
The ICM is usually approximated as an **optically thin plasma** (because the mean free path of photons is $\gtrsim 100\,\mathrm{Mpc}$ and thus much larger than the length scale of cluster) in **Collisional Ionisation Equilibrium** (CIE), where the rates of collisional ionisation and of radiative recombination are equal, the ions always are in the ground state and there is immediate emission of photon after collisional excitation. The temperature of each model of the ICM (see *Chapter 2*), in agreement with the average observed temperature profile of *Ghirardini et al. (2019)*, is $\gtrsim 5\,\mathrm{keV}$ throughout the cluster, so the X-rays are the ideal wavelengths for observing the thermal emission reconstructed from our models of the ICM. The ICM in our distributions thus emits in continuum via thermal Breemstrahlung, two photon decay and recombination of free electrons and in line via the radiative emission from collisional excitation of inner-shell electrons of heavy metals.

3.1. Photometric proxies

The X-ray photometry in the framework of galaxy clusters is a powerful tool to test our knowledge of the dynamics of the ICM: we expect the dynamical processes that involve the ICM to leave a trace in the morphology of X-ray surface brightness (*e.g. Schuecker et al. 2004, Zhuravleva et al. 2022* and references therein). The X-ray isophotes of clusters in the sky present a wide variety of shapes, primarily depending on the dynamical state of cluster (relaxed or disturbed). Given that the X-ray isophotes usually are noisy, we usually rely on the global shape parameters (for example, the average axial ratio) to perform a **photometric classification** of clusters. However, this photometric classification does not show an evident bimodality between relaxed and disturbed clusters (*e.g. Campitiello et al. 2022* and references therein). Indeed, even in relaxed clusters there are several physical phenomena, which contribute to an aspherical morphology of X-ray surface brightness, such as the DM halo flattening (see, e.g., *Buote & Canizares 1992*), the presence of subhalos and gas substructures, an anisotropic turbulence [expected from numerical hydrodynamical simulations (*e.g. Lau et al. 2009*)], the gas clumpiness (*e.g. Towler et al. 2023* and references therein), a significant rotation of the ICM (see, e.g., *Fang et al. 2009, Bianconi et al. 2013* and references therein). However, it is hard to separate these effects only on the basis of the X-ray photometric information and, consequently, the morphological parameters encode the combination of these effects.
The shape of X-ray surface brightness reconstructed from our models of the ICM departs from the spherical symmetry as due to the DM halo flattening and/or the rotation of the ICM. We thus interpret the observed flattening of X-ray isophotes only on the basis of these phenomena to put upper limits on the rotation patterns and/or on DM halo shapes.

3.1.1. Morphology of the X-ray surface brightness distributions

The dominant radiative process in continuum down to a temperature $\sim 10^6\,\mathrm{K}$ is the thermal **Breemstrahlung**, so the bolometric emission of the ICM increases with the temperature. In this Chapter, to account for the X-ray bolometric emission of a high-energy plasma in CIE, we use the **Cooling Function** (*Figure 3.1*;*Tozzi & Norman 2001*)

$$\Lambda(T) = C_1(T(\mathrm{keV}))^{\alpha} + C_2(T(\mathrm{keV}))^{\beta} + C_3, \tag{3.1}$$

where the parameters C_1, C_2, C_3, α and β are listed in *Table 3.1.*

Parameter	Value
C_1	$8.6 \times 10^{-3}\,\mathrm{erg/s \cdot cm^3 \cdot keV^{-\alpha}}$
C_2	$5.8 \times 10^{-2}\,\mathrm{erg/s \cdot cm^3 \cdot keV^{-\beta}}$
C_3	$6.3 \times 10^{-2}\,\mathrm{erg/s \cdot cm^3}$
α	-1.7
β	0.5

Table 3.1.: Parameters of *Cooling Function (3.1)*. We quote these parameters for a plasma of $Z = 0.3\,\mathrm{Z_\odot}$.

In the plane of the sky, the integration of bolometric emissivity of each fluid element residing in a optically thin plasma along the *l.o.s.* is known as the **surface brightness**

$$\Sigma := \int_{l.o.s.} n_t n_e \Lambda(T) dl,$$

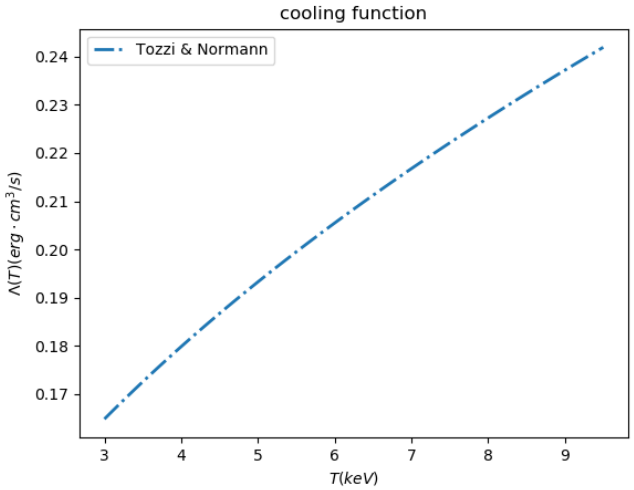

Figure 3.1.: Profile of Cooling Function $\Lambda(T)$ of *Tozzi & Norman (2001)* for a high-energy plasma of metallicity $Z = 0.3\,Z_{\odot}$ in CIE.

where dl is an infinitesimal length of $l.o.s.$, $n_t = n_N + n_p \simeq n_p$ is the number density of positive charges (at such temperatures there is no fully neutral charge), with n_p and n_N the number density of free protons and of positive nuclei, respectively. In order to see the maximum flattening of X-ray isophotes, we assume to observe edge-on our distributions of the ICM: the surface brightness as a function of the coordinates R and z in the plane of the sky is

$$\Sigma(R;z) = 2\int_R^{\infty} \frac{n_t(\tilde{r};z)n_e(\tilde{r};z)\Lambda(\tilde{r};z)\tilde{r}d\tilde{r}}{\sqrt{\tilde{r}^2 - R^2}}, \tag{3.2}$$

where $\tilde{r}$ represents the radius in the plane, parallel to the equatorial plane, crossed by $l.o.s.$

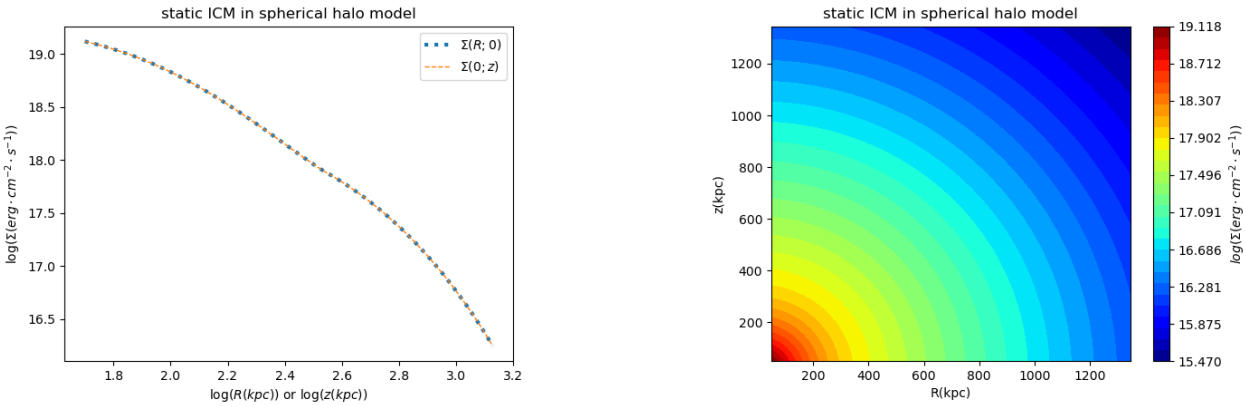

(a) (b)

Figure 3.2.: Profile (left panel) and map (right panel) of surface brightness (Σ) of *NRN* model spanning the range $[50\,\mathrm{kpc}; r_{500}]$ (see *Section 2.1.1* for the definition of r_{500}). Here the plane of the sky is parallel to the meridional plane: the orange dashed and blue dotted profiles refer to $\Sigma(0;z)$ and $\Sigma(R;0)$, respectively.

As we note from the morphologies of surface brightness distributions reconstructed through *Eq.(3.2)* from our static models in *Figures 3.2, 3.3* and *3.4*, despite the projection in the plane of the sky, *Eq.(3.2)* preserves the ellipsoidal symmetry of the density distribution of the ICM.

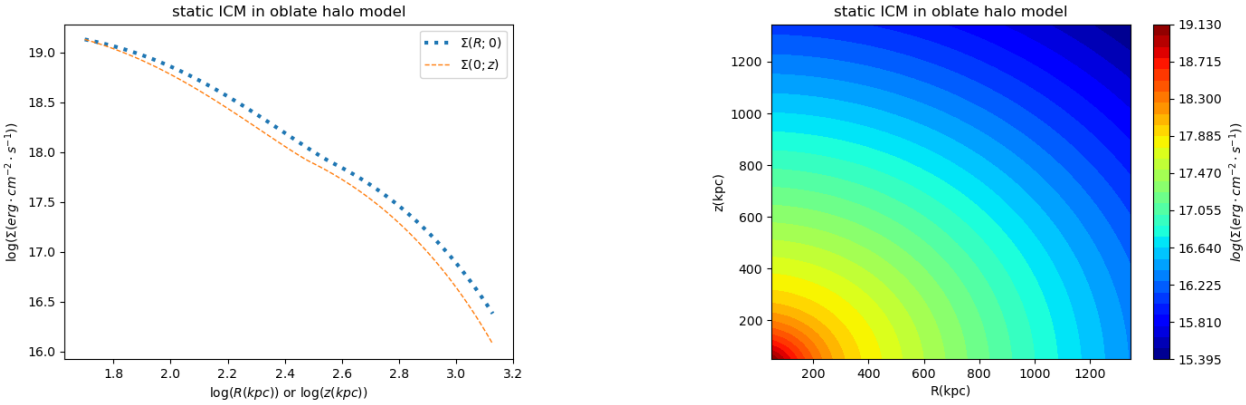

(a) (b)

Figure 3.3.: Same as *Figure 3.2*, but for *NRO* model.

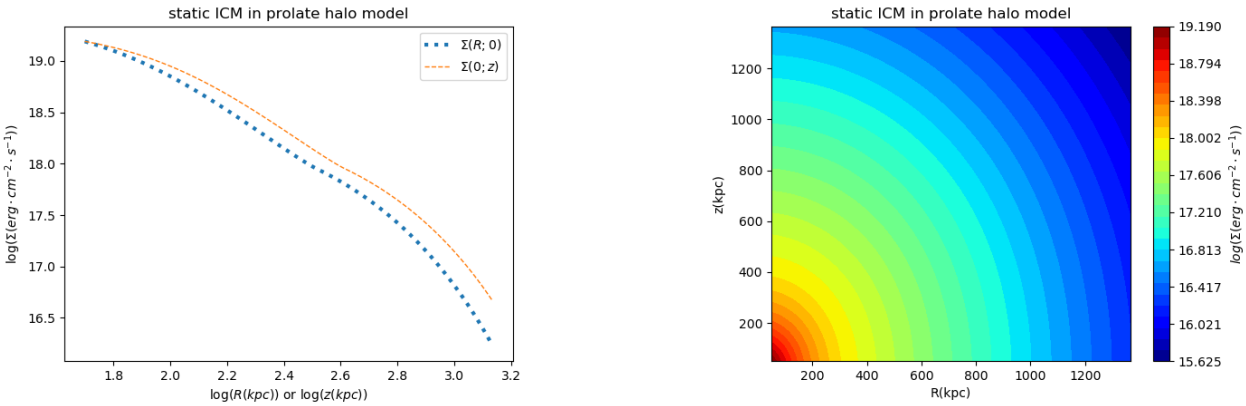

(a) (b)

Figure 3.4.: Same as *Figure 3.2*, but for *NRP* model.

The morphology of surface brightness distributions in *Figures 3.5, 3.6* and *3.7* (reconstructed from rotating ICM models through *Eq.(3.2)*) is rounder than the density distributions of the ICM (see *Figures 2.7, 2.9* and *2.8*), since the integration along the *l.o.s.* "softens" the peanut-shape of density distribution (we recall that the temperature is stratified over the density here). When comparing to the X-ray observations (see *Campitiello et al. 2022* and references therein for some examples of X-ray images of real clusters), we conclude that the shapes of surface brightness maps reconstructed from our models of the ICM are consistent with those observed. We note that the model maps are not noisy: a fully consistent work would require the convolution with instrument response before comparing them to the observations, but this work is left for the future.

3.1.2. Ellipticity of the X-ray isophotes

Since early X-ray observations of clusters there was a clear evidence for the departure of X-ray isophotes from the spherical symmetry, so a tool to convert the visual morphological classification into a quantitative form became immediately indispensable. *Buote & Canizares (1992)* proposed a method to classify the morphology of X-ray surface brightness distributions of galaxy

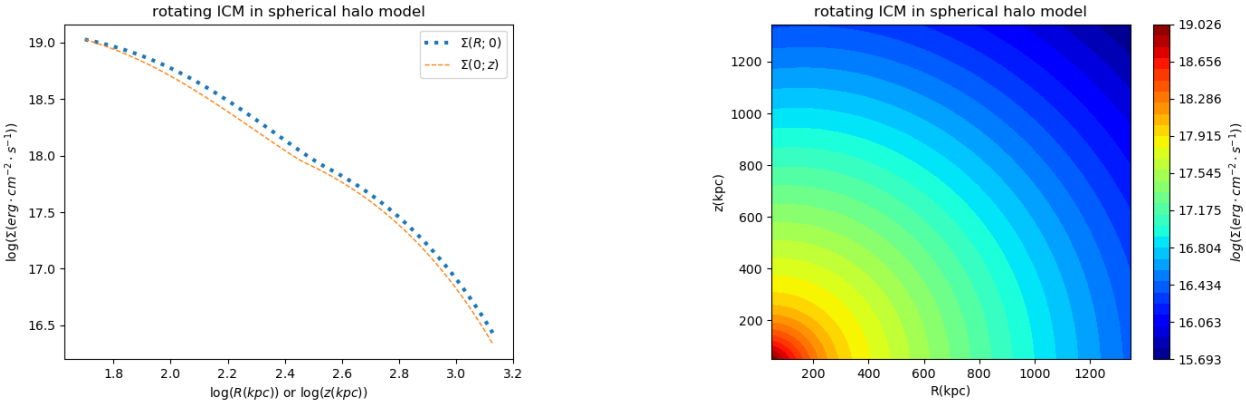

(a) (b)

Figure 3.5.: Same as *Figure 3.2*, but for *RMN* model.

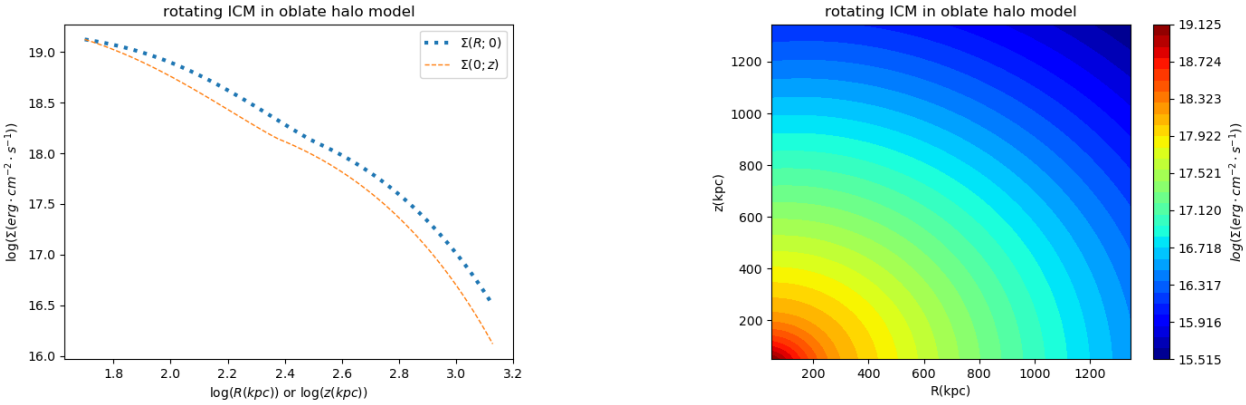

(a) (b)

Figure 3.6.: Same as *Figure 3.2*, but for *RMO* model.

clusters on the basis of an average axial ratio (see *Buote & Canizares 1994* for a complete description of this method). In a recent work *Campitiello et al. (2022)* used for the morphological classification of X-ray surface brightness distribution this average axial ratio, defined in the following way.
In the plane of the sky, the four components of inertia's tensor are

$$I_{hj} := \sum_{i=1}^{P} \Sigma_i (x_i - \langle x \rangle)^h (y_i - \langle y \rangle)^j, \tag{3.3}$$

where P is the number of points, x and y are the coordinates in the plane of the sky, Σ_i is the surface brightness evaluated at point i, while $\langle x \rangle$ and $\langle y \rangle$ define the centroid of cluster. h, j are two indices such that $0 \leq h, j \leq 2$ and $h + j = 2$.
The **average axial ratio weighted over surface brightness** (hereafter, axial ratio) is

$$\zeta := \frac{I_{min}}{I_{max}} \tag{3.4}$$

with $I_{max} := max\{I_{d1}, I_{d2}\}$ and $I_{min} := min\{I_{d1}, I_{d2}\}$, where I_{d1} and I_{d2} are the diagonal components of *inertia's tensor (3.3)* in diagonal form.
In the X-ray observations it is unusual to find the centroid of surface brightness in the center

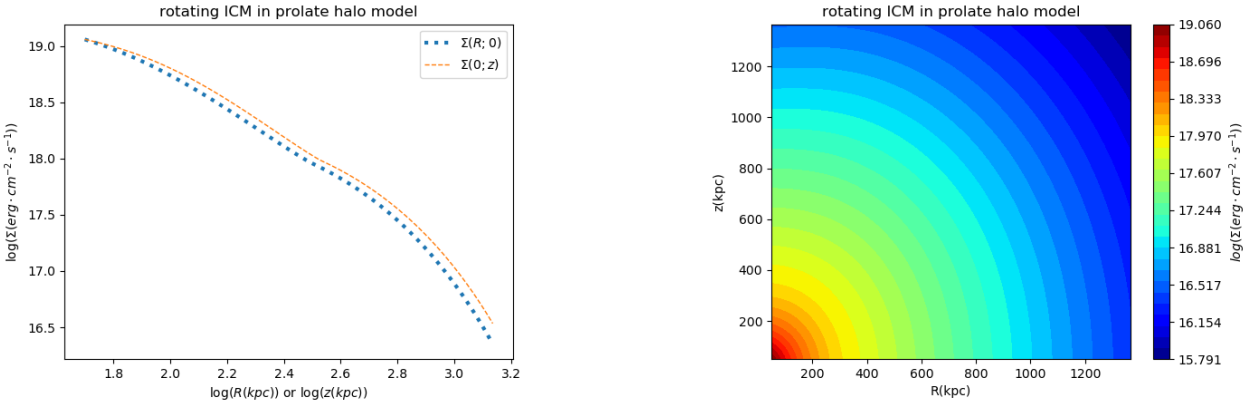

(a) (b)

Figure 3.7.: Same as *Figure 3.2*, but for *RMP* model.

of X-ray images, while in the maps of *Figures 3.2, 3.3, 3.4, 3.5, 3.6* and *3.7* $\langle x \rangle = \langle y \rangle = 0$ assuming the centre of mass as origin. If we observe the distribution of the ICM edge-on, x and y correspond to the coordinates in the meridional plane R and z, respectively, and the *inertia's tensor (3.3)* is diagonal thanks to the central symmetry of surface brightness of our models. In our maps of surface brightness $I_{d1} = 4I_{20}$ and $I_{d2} = 4I_{02}$, where I_{20} and I_{02} are given by *Eq.(3.3)* with $x = R$ and $y = z$.
In *Table 3.2* we present the axial ratios of the surface brightness distributions reconstructed from our models of the ICM by using *Eq.(3.4)*. Note that the axial ratios are close to 1 in all models: it is due to the definition of *inertia's tensor (3.3)*, where the central shape of X-ray surface brightness contributes for most. In *Figure 3.8* we compare these axial ratios to the morphological classification inferred by *Campitiello et al. (2022)* from the observations of real and simulated clusters (note that the simulated and observed distributions of ζ overlap): our morphologies correspond to highly popoluted axial ratios. It means that the assumed rotation patterns (see *Section 2.3.3*) and halo models (see *Section 1.3.2*) are consistent with the results of the X-ray observations and of hydrodynamical simulations. The **absence of a bimodal distribution** of axial ratios essentially prevents from imposing tight constraints on the shape of halos and/or on the rotation patterns of the ICM in relaxed clusters.

Model	ζ
NRN	1.00
NRO	0.90
NRP	0.86
RMN	0.97
RMO	0.88
RMP	0.93

Table 3.2.: Axial ratios (ζ) measured in the maps of surface brightness (see *Figures 3.2, 3.3, 3.4, 3.5, 3.6* and *3.7*) reconstructed from our models of the ICM.

Description of the samples used in Figure 3.8. The observed sample, used by *Campitiello et al. 2022* to measure the axial ratio of surface brightness, is the CHEX-MATE sample (*CHEX-MATE Collaboration et al. 2021*;`http://xmm-heritage.oas.inaf.it/`) that consists of 118

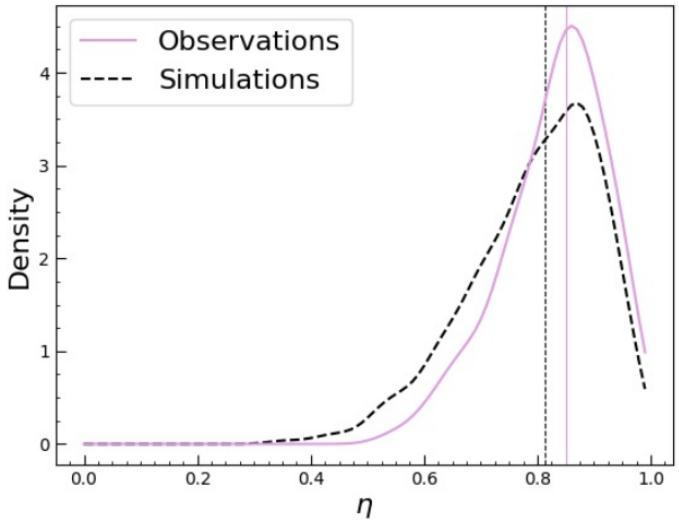

Figure 3.8.: The distribution of axial ratios (η) of the observed sample of clusters (violet solid curve) and of the simulated sample (black dashed curve) of *Campitiello et al. (2022)*. Here $\eta = \zeta$, where ζ is given by *Eq.(3.4)*. The black dashed and violet solid vertical lines are the medians of distribution of ζ in the simulated and observed samples, respectively. Figure taken from *Campitiello et al. (2022)*.

galaxy clusters, detected by Planck (`https://www.cosmos.esa.int/web/planck`) via thermal Sunyaev-Zel'dovich Effect and studied homogeneously with the X-ray observatory XMM-NEWTON (`https://www.cosmos.esa.int/web/xmm-newton`). This sample is composed of two different sub-samples:

- Tier-1 represents the population of clusters at the most recent time ($z < 0.2$);
- Tier-2 represents the population of the most massive clusters to have formed thus far in the history of the Universe (but with $z < 0.6$).

This sample contains together relaxed and disturbed clusters: *Campitiello et al. 2022* find approximately 19 relaxed, 37 disturbed and 62 mixed (which present morphological properties both of relaxed and of disturbed clusters). The simulated sample is provided by THE THREE HUNDRED collaboration (`https://www.nottingham.ac.uk/astronomy/The300/index.php`, *Cui et al. 2018*) and consists of 1564 clusters spanning a wide range of redshift ($0 < z < 0.59$) and mass ($M_{500} > 1.1 \times 10^{14} h^{-1}\,\mathrm{M}_\odot$, with $h := H_0/(100\,\mathrm{km/s/Mpc})$; see *Section 2.1.1* for the definition of M_{500}). For the sake of completeness, images associated with three different orientations of each simulated object are used to estimate the value of ζ whose distribution is shown in *Figure 3.8*. These samples take into account both non-cool-core and cool-core cluster, while our models of the ICM refer to the latter. As usual, *Campitiello et al. (2022)* consider a significantly flattened morphology of the surface brightness as a probe of an ongoing merger: *Table 3.2* is consistent with this result, given that no model of the ICM has a low axial ratio.

3.2. Spectroscopic proxies

In the near future the analysis of high quality X-ray spectra (observed by new generation facilities) will be a key tool to reveal the kinematic conditions of the ICM in relaxed clusters.

Even though this work is focused on the rotation of the ICM, we model together the prominent signatures of bulk motions expected in a X-ray spectrum (shift of centroids and broadening of the emission lines) as describes in the next Sections (consistently with previous works like, e.g., *Zhuravleva et al. 2012* and *Bianconi et al. 2013*).

3.2.1. From a model of the ICM to a X-ray spectrum

In order to detect the maximum shift of emission line centroids, we observe edge-on the rotating distributions of the ICM. Any fluid element of the ICM produces a single-temperature source spectrum, so the observed multi-temperature source spectrum of an optically thin plasma is the sum of the single-temperature source spectra of fluid elements residing along the *l.o.s.* *Mazzotta et al. (2004)* showed that for an optically thin high-temperature plasma ($T > 3\,\mathrm{keV}$ at any point of space) the fit to multi-temperature source spectrum with a **single-temperature thermal model** is acceptable regardless of the actual spread in temperature distribution. The X-ray emission of the ICM thus is recovered via a single-temperature thermal model in our mock spectra.
In the plane of the sky we associate with any quantity $Q(R;z)$ its average along the *l.o.s.* $Q_{los}(R;z)$ in the following way. For the sake of consistency, we use for all quantities of the spectrum an only one weight, that can be the bolometric emissivity

$$b := n_t n_e \Lambda(T), \tag{3.5}$$

where $\Lambda(T)$ is given by *Eq.(3.1)*, while n_e and n_t are the same as in *Eq.(3.2)*. However, in a sample of clusters from a high resolution simulation *Mazzotta et al. (2004)* demonstrate that the estimates of spectroscopic temperature with b are higher than the best-fits to the multi-temperature source spectra and derived a weight w able to provide a better approximation of **spectroscopic temperature**, once compared to the "best-fit" results of the spectral analysis. w essentially represents the **specific emissivity** of Breemstrahlung ($\propto n_t n_e T^{-1/2}$) corrected for the emissivity of the emission lines of inner-shell electrons of heavy metals:

$$w := \frac{n_t n_e}{T^{3/4}}. \tag{3.6}$$

The integral of weights of *Eq.(3.6)* along the *l.o.s.* is

$$W_{los}(R;z) = \int_{l.o.s.} w(R;z)dl = 2\int_R^\infty \frac{w(R;z)\tilde{r}}{\sqrt{\tilde{r}^2 - R^2}}d\tilde{r}, \tag{3.7}$$

where $\tilde{r}$ is the same as in *Eq.(3.2)*.
At any point in the plane of the sky the average quantity along the *l.o.s.* is

$$Q_{los}(R;z) = \frac{Q_W(R;z)}{W_{los}(R;z)}, \tag{3.8}$$

where

$$Q_W(R;z) = 2\int_R^\infty \frac{w(R;z)Q(R;z)\tilde{r}}{\sqrt{\tilde{r}^2 - R^2}}d\tilde{r}. \tag{3.9}$$

The component of azimuthal speed u_ϕ responsible for the Doppler shift of emission line centroids in each single-temperature source spectrum, which composes the X-ray emission of the ICM, is the *l.o.s.* speed $u_{los}(R) := u_\phi(R)\cos(\alpha)$, where α is the angle between the *l.o.s* and the direction

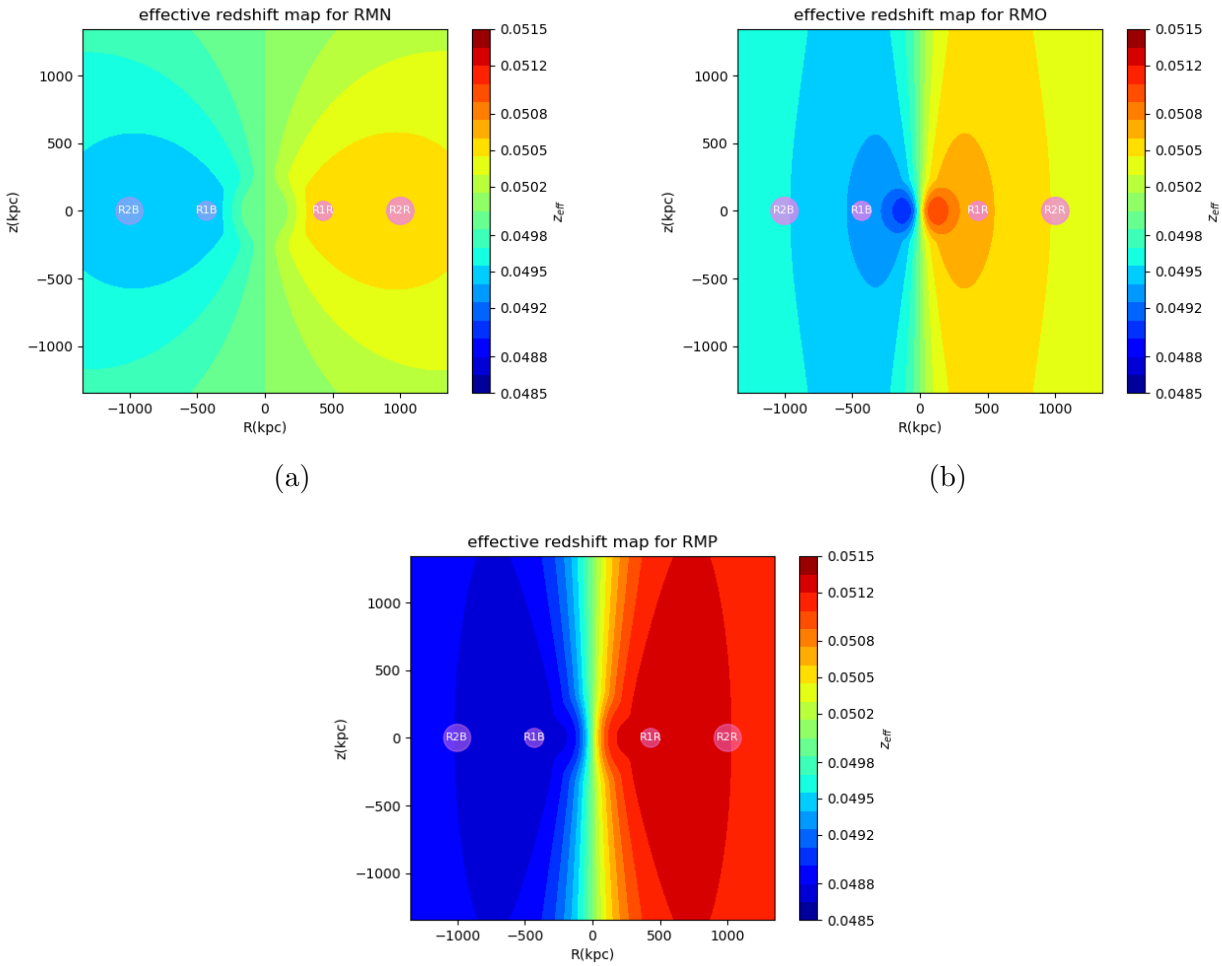

(a) (b)

(c)

Figure 3.9.: Maps of effective redshift (z_{eff}) in the plane of the sky, parallel to the meridional plane, for models *RMN* (upper left panel), *RMO* (upper right panel) and *RMP* (lower panel) models. z_{eff} is stratified over v_{los} (see *Eq.(3.12)* for the definition of z_{eff}). We focus on the circular regions *R1* and *R2* (in violet) when performing the mock observations.

of u_ϕ. For a cluster seen edge-on, $\cos(\alpha) = R/\tilde{r}$. *Eq.s (3.9)* and *(3.8)* with $Q(R;z) = u_{los}(R)$ allow us to estimate the average *l.o.s.* speed $v_{los}(R;z)$. Even though $u_{los}(R)$ respects the cylindrical symmetry, owing to the presence of $w(R;z)$ in *Eq.(3.9)* v_{los} depends also on z, as we note in *Figure 3.9*. Here, we note that good regions to measure a significant Doppler shift of emission line centroids are located around $z = 0$ in the plane of the sky. The regions that we select for the mock observations are larger than RESOLVE's half power diameter θ_H (the diameter within which half of the focused X-rays is enclosed): $\theta_H \simeq 1.6' \simeq 93\,\mathrm{kpc}$ at $z_0 = 0.05$. Let us take in the plane of the sky the circular regions (in violet in *Figure 3.9*)

- *R1* centered at the point $(430\,\mathrm{kpc}; 0\,\mathrm{kpc})$ with the radius of this region $\tilde{R} = 70\,\mathrm{kpc}$;
- *R2* centered at $(1000\,\mathrm{kpc}; 0\,\mathrm{kpc})$ with $\tilde{R} = 100\,\mathrm{kpc}$.

An usual condition to well fit to the mock X-ray spectra is to have relatively high counts, so the region *R2* is larger than *R1*.
To build a mock X-ray spectrum, we need to average $Q_{los}(R;z)$ in each circular region: the

average quantity $\langle Q \rangle$ is

$$\langle Q \rangle := \frac{\sum_{i=1}^{N} Q_{W,i}}{S_W}, \tag{3.10}$$

where

$$S_W := \sum_{i=1}^{N} W_i. \tag{3.11}$$

N is the total number of grid points within the selected region, W_i and $Q_{W,i}$ are computed at any point i in the meridional plane through *Eq.s (3.7)* and *(3.9)*, respectively.
The construction of the mock spectrum and the subsequent spectral analysis are performed with the help of the software Xspec (*Arnaud 1996*; `https://heasarc.gsfc.nasa.gov/xanadu/xspec/`). We model the X-ray thermal emission of the ICM via the velocity Broadened Astrophysical Plasma Emission Code (**BAPEC**) as the combination of the emission lines from the collisional excitation of inner shell electrons of heavy metals and of a continuum, that is the sum of the thermal Breemstrahlung, two photon decay and recombination of free electrons. The five parameters of the model BAPEC are

1. the spectroscopic temperature (measured in keV);

2. the metallicity of emitting plasma Z (evaluated with respect to a solar table; see *Anders & Grevesse 1989* for a reference table of solar elements), which regulates the prominence of the emission lines ($Z = 0.3\,\mathrm{Z}_\odot$ from *Section 2.2.3*);

3. the **effective redshift** z_{eff}, which accounts for the Doppler shift of the centroids of the emission lines from their rest-frame energy;

4. the **broadening velocity** σ_{broad} (in km/s), which measures the non-thermal broadening of the emission lines;

5. the parameter **norm**, which provides a measure of the normalization of the spectrum.

Assuming the weight in *Eq.(3.6)*, *Eq.s (3.9)* and *(3.10)* (with the substitution of T or u_{los} for Q and $\langle T_{los} \rangle$ or $\langle v_{los} \rangle$ for $\langle Q \rangle$, respectively) allow us to estimate both spectroscopic temperature and average *l.o.s.* velocity in each selected region. The difficulty to recover the exact spectroscopic temperature from a model of the ICM (*Mazzotta et al. 2004*) suggests us to call $\langle T_{los} \rangle$ as **spectroscopic-like temperature** $\langle T_{sl} \rangle$. For the sake of completeness, we estimate the spectroscopic temperature on the basis of the bolometric emissivity in the same way as $\langle T_{sl} \rangle$, with *Eq.(3.5)* instead of *Eq.(3.6)*. This temperature is called $\langle T_b \rangle$.
The Doppler shift of the centroids of the emission lines is the combination of receding velocity of galaxy clusters due to the expansion of the Universe and of a motion of the plasma along a preferential direction of the *l.o.s.* Considering $\langle v_{los} \rangle > 0$ for receding plasma (and $\langle v_{los} \rangle < 0$ for approaching), using the formula of relativistic Doppler effect we estimate the effective redshift (*Roncarelli et al. 2018*)

$$z_{eff} = (1 + z_0) \sqrt{\frac{1 + \frac{\langle v_{los} \rangle}{c}}{1 - \frac{\langle v_{los} \rangle}{c}}} - 1, \tag{3.12}$$

where c is the speed of light and $z_0 = 0.05$ is the rest-frame redshift of the cluster (from *Section 1.3*).

The definition of parameter *norm* is

$$norm := \frac{10^{-14}}{4\pi[D_A(1+z_0)]^2} \iiint_V n_H n_e dV, \tag{3.13}$$

where D_A represents the *angular distance* of galaxy cluster (in cm), n_e is the number density of electrons (in cm^{-3}) and $n_H = n_e/1.17$ in a fully ionised plasma (*Anders & Grevesse 1989*). V is the volume occupied by the ICM, which emits the radiation observed in the regions *R1* or *R2*: V represents the cylinder of basis equivalent to the region under consideration in the plane of the sky and height to $2r_{500}$. To compute *norm* we split the integral of *Eq.(3.13)* into two different integrals:

$$\iiint_V n_H n_e dR dz dl = \iint_{Area} \left(\int_{l.o.s.} n_H n_e dl \right) dR dz,$$

where $Area = \pi \tilde{R}^2$ and $\tilde{R}$ is the radius of circular region under consideration. The integration of the innermost integral gives us a function of coordinates R and z in the plane of the sky (parallel to the meridional plane)

$$A(R;z) := 2 \int_R^\infty \frac{n_H(R;z) n_e(R;z) \tilde{r}}{\sqrt{\tilde{r}^2 - R^2}} d\tilde{r}, \tag{3.14}$$

where $\tilde{r}$ is the same as in *Eq.(3.7)*. We then integrate the outermost integral in a consistent way with the derivation of other parameters of BAPEC: we use *Eq.(3.10)* with $Q_{W,i} = A_i$ and $S_W = N$ (= the number of grid points within the region under consideration), where A_i is the function in *Eq.(3.14)* evaluated at point i in the plane of the sky. The resulting value $\langle Q \rangle$ is multiplied for *Area* to find the parameter *norm*.

Model	region	$\langle T_{sl} \rangle$	norm	σ_T^{true}	$z_{eff,R}^{true}$	$z_{eff,B}^{true}$	$\langle T_b \rangle$
RMN	R1	7.54 keV	0.00075	44 km/s	0.0508	0.0492	7.72 keV
RMN	R2	6.82 keV	0.00069	41 km/s	0.0507	0.0493	7.17 keV
RMO	R1	6.87 keV	0.00110	43 km/s	0.0506	0.0494	7.47 keV
RMO	R2	6.27 keV	0.00097	35 km/s	0.0506	0.0494	6.99 keV
RMP	R1	7.27 keV	0.00076	46 km/s	0.0513	0.0487	7.49 keV
RMP	R2	6.51 keV	0.00068	42 km/s	0.0513	0.0487	6.92 keV

Table 3.3.: Input parameters of model BAPEC in our mock spectra. The colors red and blue of effective redshift (z_{eff}) allow us to distinguish immediately the receding and approaching regions, respectively, which, however, are both redshifted. We list both $\langle T_{sl} \rangle$ and $\langle T_b \rangle$, even if the input spectroscopic temperature is $\langle T_{sl} \rangle$.

A wide variety of physical phenomena contributes to the broadening of the emission lines. In a static isothermal plasma that produces a single-temperature source spectrum, the fact that the particles do not have the same kinetic energy induces a broadening of the emission lines with broadening velocity $\sigma_{th} \sim \sqrt{k_B T/(A m_p)}$, where A represents the *mass number* of atoms responsible for this line emission and k_B is Boltzmann's Constant. This contribution is called **thermal broadening** and the model BAPEC accounts for it while producing a single-temperature source spectrum. Even though the spectroscopic temperature of a multi-temperature source spectrum is recovered to good approximation by fitting with a single-temperature model (see above), the **inhomogeneity of temperature** of the ICM along the *l.o.s.* is the cause of an additional broadening. Indeed, the temperature dispersion with respect to the $\langle T_{sl} \rangle$ is

$$\vartheta_T^2(R;z) := [T(R;z) - \langle T_{sl} \rangle]^2, \tag{3.15}$$

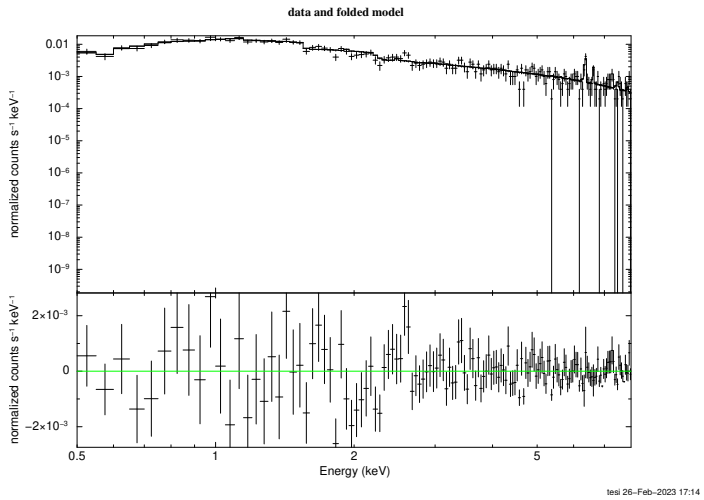

Figure 3.10.: Fit (upper panel) to the mock spectrum of model *RMP* in the region *R1* (with $\sigma_{turb} = 400\,\mathrm{km/s}$) and the residuals (lower panel). $FeXXV$ and $FeXXVI$ (with rest-frame energies close to 6.7 keV and 6.9 keV, respectively) are the prominent emission lines in the upper panel. The spectrum span the energy range 0.5-8 keV.

where $T(R; z)$ is the temperature of any fluid element residing in the volume V (see above). Substituting ϑ_T^2 for Q in *Eq.s (3.9)* and *(3.10)* and using the weight in *Eq.(3.6)*, we compute $\langle Q \rangle = \langle \vartheta_T^2 \rangle$. Then, we convert $\langle \vartheta_T^2 \rangle$ into the temperature inhomogeneity broadening velocity σ_T using

$$\sigma_T = \sqrt{\frac{k_B \sqrt{\langle \vartheta_T^2 \rangle}}{A m_p}}. \tag{3.16}$$

In the X-rays the most prominent emission lines of the ICM are $FeXXV$ and $FeXXVI$ (see *Figure 3.10*), so we assume $A = 56$. It is evident that σ_{th} and σ_T are low for $A = 56$ (see below for reference values of σ_{th} and σ_T) and, consequently, the chaotic motions of the ICM, if any, are expected to provide a non-negligible contribution to the broadening of the emission lines. On the basis of the works that over the last decades investigated the kinematic conditions of the ICM via hydrodynamical simulations and observations, the **turbulence** is believed to be an ubiquitous ingredient in galaxy clusters (*e.g. Schuecker et al. 2004, Vazza et al. 2017* and references therein). Indeed, the processes originating on the galactic scales (such as AGN feedback and bubbles; *e.g. Gaspari et al. 2012*), the MHD instability of the ICM (such as MRI and magnetothermal instability; *e.g. McCourt et al. 2011*) and mostly cluster-scale processes (such as mergers and motions on large-scale structure of the Universe; *e.g. Vazza et al. 2017*) trigger and sustain the turbulence of the ICM. At the same time, mock and real observations emphasized the prominent role which could play the turbulence in the future high-quality X-ray spectra: providing the dominant contribution to the broadening of the emission lines (*e.g. Sunyaev et al. 2003, Zhuravleva et al. 2012*). In general, we expect that a significant broadening of the emission lines alters the fitting Doppler shift of emission line centroids: at fixed signal-to-noise ratio there are lower chances to detect in presence of a significant turbulence of the ICM the exact energy of the emission line centroids and, consequently, their shift (see, e.g., *Bianconi et al. 2013*). In order to mimic an observation as far as possible realistic, we assume some values of turbulent speed of the ICM (σ_{turb}): in agreement with the main works in literature (*e.g. Zhuravleva et al. 2012*) and with the observed spectrum of Perseus (*Hitomi Collaboration et al. 2016*), we consider $\sigma_{turb} = 100, 200, 400\,\mathrm{km/s}$. We estimate the broadening velocity σ_{broad} as due to the combination of turbulent and temperature inhomogeneity velocity dispersions

using

$$\sigma_{broad} = \sqrt{\sigma_{turb}^2 + \sigma_T^2}, \tag{3.17}$$

where σ_T is given by *Eq.(3.16)*.
In order to mimic an observation as far as possible realistic, we introduce the absorption of Milky Way (MW) as due to an *equivalent hydrogen column density*, typical of MW, $N_H = 0.05 \times 10^{22}\,\mathrm{cm}^{-2}$ (*HI4PI Collaboration et al. 2016*) via the PHotoelectric ABSorption model (**PHABS**). We reconstruct the X-ray thermal emission of the ICM in any receding or approaching region under consideration and for any rotating model under different turbulent conditions of the ICM using a combination of PHABS and BAPEC (whose parameters are listed in *Table 3.3*). Here, *Eq.(3.6)* provides lower estimates of spectroscopic temperature than *Eq.(3.5)* (*i.e.* $\langle T_b \rangle > \langle T_{sl} \rangle$), since *Eq.(3.1)* is an increasing function of temperature, while *Eq.(3.6)* a decreasing one. We note that in *Table 3.3* $\sigma_T < 50\,\mathrm{km/s}$ and, for the sake of completeness, we report that in our models of the ICM $\sigma_{th} \simeq 110\,\mathrm{km/s}$ for $A = 56$. These values thus confirm that in regions *R1* and *R2* the turbulence of $\sigma_{turb} \geq 200\,\mathrm{km/s}$ provides the dominant contribution to the broadening of the emission lines $FeXXV$ and $FeXXVI$ (see also *Zhuravleva et al. 2012* and *Sunyaev et al. 2003*).

Reg.	σ_{turb}^{true}[km/s]	$z_{eff}^{fit}(\sigma_s)$	σ_{broad}^{fit}[km/s]	$Z^{fit}[Z_\odot](\sigma_Z)$	T_{spec}^{fit}[keV](σ_{SL})
R1R	0	$0.0506 \pm 0.0002(3.0)$	83 ± 83	$0.41 \pm 0.08(1.4)$	$7.17 \pm 0.58(0.6)$
R1R	100	$0.0506 \pm 0.0002(3.0)$	125 ± 68	$0.36 \pm 0.07(0.9)$	$7.50 \pm 0.56(0.1)$
R1R	200	$0.0510 \pm 0.0005(2.0)$	381 ± 145	$0.30 \pm 0.07(0.0)$	$6.93 \pm 0.60(1.0)$
R1R	400	$0.0501 \pm 0.0006(0.2)$	441 ± 194	$0.34 \pm 0.09(0.4)$	$8.35 \pm 0.82(1.0)$
R1B	0	$0.0495 \pm 0.0002(2.5)$	5 ± 81	$0.41 \pm 0.08(1.4)$	$7.69 \pm 0.66(0.2)$
R1B	100	$0.0493 \pm 0.0002(3.5)$	63 ± 95	$0.31 \pm 0.07(0.1)$	$7.90 \pm 0.76(0.5)$
R1B	200	$0.0493 \pm 0.0002(3.5)$	164 ± 62	$0.47 \pm 0.09(1.9)$	$7.62 \pm 0.59(0.1)$
R1B	400	$0.0502 \pm 0.0005(0.4)$	458 ± 137	$0.42 \pm 0.08(1.5)$	$7.12 \pm 0.61(0.7)$
R2R	0	$0.0510 \pm 0.0003(3.3)$	134 ± 90	$0.25 \pm 0.06(0.8)$	$6.53 \pm 0.58(0.5)$
R2R	100	$0.0506 \pm 0.0004(1.5)$	177 ± 116	$0.29 \pm 0.07(0.1)$	$7.22 \pm 0.61(0.7)$
R2R	200	$0.0512 \pm 0.0002(6.0)$	191 ± 102	$0.27 \pm 0.07(0.4)$	$6.42 \pm 0.56(0.7)$
R2R	400	$0.0502 \pm 0.0006(0.3)$	381 ± 97	$0.36 \pm 0.08(0.8)$	$7.09 \pm 0.63(0.4)$
R2B	0	$0.0493 \pm 0.0003(2.3)$	89 ± 161	$0.22 \pm 0.06(1.3)$	$7.14 \pm 0.64(0.5)$
R2B	100	$0.0492 \pm 0.0003(2.7)$	133 ± 95	$0.29 \pm 0.07(0.1)$	$7.21 \pm 0.63(0.6)$
R2B	200	$0.0494 \pm 0.0002(3.0)$	220 ± 105	$0.32 \pm 0.07(0.3)$	$6.70 \pm 0.55(0.2)$
R2B	400	$0.0494 \pm 0.0003(2.0)$	269 ± 97	$0.41 \pm 0.08(1.4)$	$7.07 \pm 0.58(0.4)$

Table 3.4.: Output parameters of the best-fit to the mock spectra reconstructed from the model *RMN* on the basis of the parameters of *Table 3.3* and, then, convolved with the response matrices of RESOLVE. The use of blue and red allows us to distinguish the spectral analyses for approaching and receding ICMs in cluster rest-frame, respectively. The apex "true" refers to a theoretical value, while "fit" to a measurement. σ_s, σ_Z and σ_{SL} are the significativities of rotation *l.o.s.* speed (*Eq.(3.18)*), of metallicity (*Eq.(3.19)* with $Q = Z$) and of spectroscopic temperature (*Eq.(3.19)* with $Q = T$), respectively.

3.2.2. Detectability of the shift of the centroids of the emission lines

In this Section, we update and extend the work of *Bianconi et al. (2013)*, mimicking the observation of the X-ray thermal emission of the ICM in the selected regions (see *Section 3.2.1*)

Reg.	σ^{true}_{turb}[km/s]	$z^{fit}_{eff}(\sigma_s)$	σ^{fit}_{broad}[km/s]	$Z^{fit}[Z_\odot](\sigma_Z)$	T^{fit}_{spec}[keV](σ_{SL})
R1R	0	$0.0507 \pm 0.0002(3.5)$	0 ± 90	$0.33 \pm 0.06(0.5)$	$7.20 \pm 0.48(0.7)$
R1R	100	$0.0508 \pm 0.0003(2.7)$	154 ± 82	$0.26 \pm 0.05(0.8)$	$7.11 \pm 0.50(0.5)$
R1R	200	$0.0509 \pm 0.0003(3.0)$	248 ± 93	$0.29 \pm 0.05(0.2)$	$6.94 \pm 0.48(0.1)$
R1R	400	$0.0508 \pm 0.0006(1.3)$	444 ± 140	$0.30 \pm 0.06(0.0)$	$6.53 \pm 0.44(0.8)$
R1B	0	$0.0492 \pm 0.0002(4.0)$	91 ± 88	$0.33 \pm 0.09(0.3)$	$7.36 \pm 0.52(0.9)$
R1B	100	$0.0494 \pm 0.0002(3.0)$	2 ± 105	$0.27 \pm 0.05(0.6)$	$6.83 \pm 0.47(0.1)$
R1B	200	$0.0495 \pm 0.0003(1.7)$	224 ± 98	$0.26 \pm 0.05(0.8)$	$6.45 \pm 0.82(0.5)$
R1B	400	$0.0494 \pm 0.0004(1.5)$	278 ± 102	$0.29 \pm 0.06(0.2)$	$7.24 \pm 0.55(0.7)$
R2R	0	$0.0506 \pm 0.0002(3.0)$	3 ± 115	$0.24 \pm 0.05(1.2)$	$5.97 \pm 0.40(0.7)$
R2R	100	$0.0503 \pm 0.00002(1.5)$	36 ± 148	$0.25 \pm 0.05(1.0)$	$6.49 \pm 0.48(0.5)$
R2R	200	$0.0502 \pm 0.0003(0.7)$	194 ± 88	$0.26 \pm 0.05(0.8)$	$6.33 \pm 0.43(0.1)$
R2R	400	$0.0503 \pm 0.0004(0.8)$	323 ± 125	$0.29 \pm 0.05(0.2)$	$5.92 \pm 0.39(0.9)$
R2B	0	$0.0494 \pm 0.0002(3.0)$	27 ± 121	$0.29 \pm 0.05(0.2)$	$6.43 \pm 0.45(0.4)$
R2B	100	$0.0495 \pm 0.0002(2.5)$	0 ± 98	$0.32 \pm 0.06(0.3)$	$6.76 \pm 0.47(1.0)$
R2B	200	$0.0500 \pm 0.0006(0.0)$	244 ± 115	$0.30 \pm 0.06(1.0)$	$6.19 \pm 0.43(0.2)$
R2B	400	$0.0497 \pm 0.0004(0.8)$	329 ± 135	$0.27 \pm 0.05(0.6)$	$5.87 \pm 0.40(1.0)$

Table 3.5.: Same as *Table 3.4*, but for *RMO*.

with an exposure time of 100 ksec. Once reconstructed the thermal emission of our rotating models of the ICM, we build the mock X-ray spectra in the range 0.5-8 keV convolving the data with an instrumental response function of RESOLVE (`https://heasarc.gsfc.nasa.gov/docs/xrism/proposals/`). Despite the symmetry of each model of the ICM (note also the symmetry of effective redshift around $z_0 = 0.05$ in *Table 3.3*), we convolve separately its data for approaching and receding ICMs to account for the different behavior of response matrices at different energies. Using the *C-statistics* of Xspec, we fit the model BAPEC plus the absorption PHABS to any mock spectrum with no "frozen" parameter (an example of these spectral fittings is *Figure 3.10*). As we note from *Figure 3.10*, the relatively high emissivity of the emission lines $FeXXV$ and $FeXXVI$ makes them particularily useful for measuring the Doppler shift via a spectral fitting. The mock spectrum at energies around 6-7 keV thus provides the most valuable informations for the spectral analysis to measure a *l.o.s.* speed.
In *Tables 3.4, 3.5* and *3.6* we report our results for the models *RMN, RMO* and *RMP*, respectively: in particular, the **significativity** of *l.o.s.* speed

$$\sigma_s := \frac{\left| z^{fit}_{eff} - z_0 \right|}{err_z}, \tag{3.18}$$

where z^{fit}_{eff} is the "best-fit" redshift and err_z the error of the fitting redshift to $\simeq 67\%$ of confidence. We recall that the Doppler shift of emission line centroids is due to the rotation of the ICM and to the expansion of the Universe (associated with z_0). σ_s thus measures the significance of the Doppler shift of the rotation: $\sigma_s < 1$ means no significant detection of a *l.o.s.* speed of the ICM. Most spectral analyses have $\sigma_s > 1$: the measurement of rotation thus is significant from these mock spectra. However, as discussed in *Section 3.2.1*, in presence of highly significant turbulence (*i.e.* $\sigma_{turb} \geq 200$ km/s) the Doppler shift fitting suffers from a higher error and preserves a good significativity only in the spectra of the model *RMP*, where the peak of the rotation speed is higher (see also *Figure 2.6a*). Indeed, the model *RMP* has everywhere higher $z_{eff} - z_0$ than other rotating models, as we note from *Figure 3.9*.
The results of σ_s in *Table 3.6* demonstrate the capability of RESOLVE to measure the Doppler shift of the centroids of the emission lines due to $\langle v_{los} \rangle \gtrsim 300$ km/s with a good significativity

Region	σ^{true}_{turb}[km/s]	$z^{fit}_{eff}(\sigma_s)$	σ^{fit}_{broad}[km/s]	$Z^{fit}[Z_\odot](\sigma_Z)$	T^{fit}_{spec}[keV](σ_{SL})
R1R	0	$0.0513 \pm 0.0002(6.5)$	0 ± 122	$0.30 \pm 0.07(0.0)$	$7.59 \pm 0.69(0.5)$
R1R	100	$0.0513 \pm 0.0002(6.5)$	11 ± 126	$0.30 \pm 0.07(0.0)$	$7.46 \pm 0.73(0.3)$
R1R	200	$0.0514 \pm 0.0002(7.0)$	191 ± 73	$0.36 \pm 0.07(0.9)$	$6.46 \pm 0.51(1.6)$
R1R	400	$0.0510 \pm 0.0006(1.7)$	360 ± 154	$0.31 \pm 0.08(0.1)$	$8.11 \pm 0.81(1.0)$
R1B	0	$0.0487 \pm 0.0002(6.5)$	1 ± 88	$0.29 \pm 0.07(0.1)$	$6.87 \pm 0.57(0.7)$
R1B	100	$0.0486 \pm 0.0003(4.7)$	136 ± 109	$0.28 \pm 0.07(0.3)$	$7.23 \pm 0.63(0.1)$
R1B	200	$0.0482 \pm 0.0004(4.5)$	263 ± 126	$0.21 \pm 0.06(1.5)$	$6.68 \pm 0.58(1.0)$
R1B	400	$0.0492 \pm 0.0006(1.3)$	395 ± 166	$0.32 \pm 0.08(0.3)$	$7.72 \pm 0.71(0.6)$
R2R	0	$0.0512 \pm 0.0003(4.0)$	1 ± 105	$0.23 \pm 0.08(0.9)$	$6.57 \pm 0.65(0.1)$
R2R	100	$0.0515 \pm 0.0002(7.5)$	47 ± 144	$0.32 \pm 0.08(0.3)$	$6.33 \pm 0.47(0.4)$
R2R	200	$0.0517 \pm 0.0002(8.5)$	10 ± 365	$0.31 \pm 0.07(0.1)$	$6.77 \pm 0.58(0.4)$
R2R	400	$0.0510 \pm 0.0003(3.3)$	171 ± 105	$0.33 \pm 0.08(0.4)$	$7.24 \pm 0.68(1.1)$
R2B	0	$0.0484 \pm 0.0002(8.0)$	46 ± 179	$0.30 \pm 0.06(0.0)$	$5.75 \pm 0.43(1.8)$
R2B	100	$0.0485 \pm 0.0003(5.0)$	0 ± 130	$0.21 \pm 0.06(1.5)$	$6.27 \pm 0.53(0.5)$
R2B	200	$0.0484 \pm 0.0003(5.3)$	122 ± 99	$0.28 \pm 0.06(0.3)$	$6.06 \pm 0.48(0.9)$
R2B	400	$0.0490 \pm 0.0004(2.5)$	413 ± 126	$0.29 \pm 0.07(0.1)$	$6.44 \pm 0.56(0.1)$

Table 3.6.: Same as *Table 3.4*, but for *RMP*.

even in presence of a non-thermal broadening of $200\,\mathrm{km/s} \lesssim \sigma_{broad} \lesssim 400\,\mathrm{km/s}$ (where σ_{broad} is given by *Eq.(3.17)*), when observing a partial region of a galaxy cluster at redshift $z_0 = 0.05$ with an exposure time of 100 ksec. It is allowed by the high energy resolution (ΔE) of RESOLVE: $\Delta E \simeq 7\,\mathrm{eV}$ FWHM at 6-7 keV allows us to measure with a good significativity the Doppler shift of $\simeq 10\,\mathrm{eV}$ FWHM of the iron lines.
In addition to the significativity of the *l.o.s.* speed, in *Tables 3.4, 3.5* and *3.6* we report the significativities of spectroscopic temperature T^{fit}_{spec} (called σ_{SL}) and of metallicity Z^{fit} (called σ_Z) to emphasize the capability and the limits of the spectral analysis to recover the input parameters of *Table 3.3*. The significativity associated with the "best-fit" quantity Q^{fit} (with $Q^{fit} = T^{fit}_{spec}, Z^{fit}$ in *Tables 3.4, 3.5* and *3.6*) is

$$\sigma_Q = \frac{\left|Q^{fit} - Q^{true}\right|}{err_Q}, \tag{3.19}$$

where Q^{true} and err_Q are the input parameters (of *Table 3.3*) and the error of Q^{fit} to $\simeq 67\%$ of confidence, respectively (the significativity of T^{fit} is called σ_{SL}). In *Eq.(3.19)*, σ_Q measures essentially at which level the recovered physical parameters match the input values: $\sigma_Q \leq 1$ means that the spectral analysis recovers the input parameter Q^{true} to $\simeq 67\%$ of confidence. Note that $\sigma_Z < 1$ and $\sigma_{SL} < 1$ in most spectral fittings where $\sigma_s > 2$: the "best-fit" parameters accurately match the input Z and T_{sl}, while keeping fairly low the errors of z_{eff} to $\simeq 67\%$ of confidence. It reinforces the robustness of our conclusions on the chance to detect with RESOLVE the *l.o.s.* speed in high-quality X-ray spectra of focusing partial regions of clusters. Note that the fitting relative error $\sim err_\sigma/\sigma^{fit}_{broad}$ in *Tables 3.4, 3.5* and *3.6* usually is very high for $\sigma^{true}_{turb} = 0$: the spectral fittings are essentially low sensitive to the contibution of temperature inhomogeneity along the *l.o.s.* to the broadening of the emission lines. It is due to low σ^{true}_T for any model and in any selected region in *Table 3.3*. From the comparison of *Tables 3.4, 3.5* and *3.6* with *Table 3.3*, $\langle T_b \rangle$ usually matches the "best-fit" spectroscopic temperature to $\simeq 67\%$ of confidence: our results do not appear to be strongly correlated to the weight used to estimate the spectroscopic temperature (see *Section 3.2.1*).
Since there is low scatter in the average observed thermodynamic profiles of the ICM outside the

core (see *Section 2.1.2*), we expect no significant differences in the results of mock observations with RESOLVE (with an exposure time of 100 ksec) in the regions *R1* and *R2* for a large sample of clusters of $M_{200} \simeq 10^{15}\,\mathrm{M}_{\odot}$ at redshift $z_0 = 0.05$ (see also *Section 3.2.3*). Nevertheless, in order to show that our mock X-ray spectra are representative of those of a large sample of massive clusters, we compare them to a direct observable in *Section 3.2.3*.

3.2.3. Comparison with the mass-luminosity relation

Even though in most spectral fittings the significativities of spectroscopic temperature and metallicity are < 1 (see *Section 3.2.2*), the mismatch between the "best-fit" results of our mock observations (see *Tables 3.4, 3.5* and *3.6*) and the input parameters (in *Table 3.3*) suggests that using realistic intrinsic properties of the ICM does not necessarily mean to produce mock X-ray spectra representative of those observed (see also *Section 3.2.1* and *Mazzotta et al. 2004*). We thus perform in this Section a comparison of our mock X-ray spectra with a direct observable: in general, a **mass-luminosity relation** provides a valuable test for cluster models and spectra. We recall the *relation (2.2)* with $\Delta = 500$: $M_{500} \propto T_{500}^{3/2} E^{3/2}(z)$ (the same relation can be also derived from the self-similar model of *Kaiser 1986*; see also *Kravtsov & Borgani 2012*). When dealing with X-ray observations, it is useful to substitute the bolometric X-ray luminosity $L_{X,bol}$ for T_{500}: in an entirely pressure-supported massive cluster the predicted mass-luminosity (hereafter, M-L) relation is (*Voit 2005*)

$$M_{500} \propto L_{X,bol}^{3/4} E(z)^{-7/4}, \tag{3.20}$$

where M_{500} is the mass within the sphere of radius r_{500} (here, we use the notation introduced in *Section 2.1*).
From the X-ray observations there is a clear evidence for a scaling relation between the bolometric X-ray luminosity and the dynamical mass of clusters: it means that the clusters are shaped by gravity to first approximation. However, the observed M-L relation is for a massive cluster (*Reichert et al. 2011*)

$$M_{500} \simeq 1.64 \left(\frac{L_{X,SR}}{10^{44}\,\mathrm{erg/s}} \right)^{0.52} E(z)^{-0.90} 10^{14}\,\mathrm{M}_{\odot}, \tag{3.21}$$

where $L_{X,SR}$ is the bolometric luminosity associated with the centroid of scaling relation, and thus departs from *Eq.(3.20)*. In *Eq.(3.21)*, M_{500} is usually interpreted as the dynamical mass of cluster, however in this work we consider M_{500} as the mass of the halo. The cause of deviation from *Eq.(3.20)* could be the interplay between cooling and heating and more likely the departure from the hydrostatic equilibrium (*e.g. Kravtsov & Borgani 2012*).
Reichert et al. (2011) observed in the M-L relation a scatter S, which for massive clusters is well fit by a **log-normal distribution** of bolometric luminosity $L_{X,bol}$ with dispersion $\sigma_{\log L} = 0.25$

$$S(\log(L_{X,bol})) = \frac{1}{\sqrt{2\pi}\sigma_{\log L}} \exp\left[-\frac{(\log(L_{X,bol}) - \log(L_{X,SR}))^2}{2\sigma_{\log L}^2} \right], \tag{3.22}$$

where $L_{X,SR}$ is given by *Eq.(3.21)*. The observed mass-temperature (hereafter, M-T) relation is for a massive cluster (*Reichert et al. 2011*)

$$M_{500} \simeq 0.291 (T_{M-T}(\mathrm{keV}))^{1.62} E(z)^{-1.04} 10^{14}\,\mathrm{M}_{\odot}, \tag{3.23}$$

and thus departs from *Eq.(2.2)*. From the X-ray observations *Reichert et al. (2011)* recover M_{500}, T_{M-T} and $L_{X,bol}$ in *Eq.s (3.21)* and *(3.23)* assuming spherical symmetry and isothermal

β-model (which is derived from the hydrostatic equilibrium of the ICM).
In *Figures 2.2, 2.4, 2.5, 2.7, 2.8* and *2.9* we compare the temperature T_{M-T}, computed through *Eq.(3.23)*, to the profiles of temperature in our models of the ICM. Note that T_{M-T} is the temperature associated with radii $< r_{500}$ ($\sim 1300\,\mathrm{kpc}$ in these profiles).
In general, the X-ray spectrometers are more accurate in the **soft-X band**, so we measure in the range 0.5-2 keV the fluxes of our mock spectra in *Section 3.2.2* via the task FLUX (of Xspec). We report the measurements of these fluxes in *Table 3.7*: they represent reference values in any region under consideration and for any model of the ICM.

Region	$\mathcal{F}^{spec}_{RMN}$	$\mathcal{F}^{spec}_{RMO}$	$\mathcal{F}^{spec}_{RMP}$	$\mathcal{F}^{M-L}_{soft-X}$
R1	$\simeq 4.6$	$\simeq 5.0$	$\simeq 3.6$	4.7
R2	$\simeq 5.3$	$\simeq 4.5$	$\simeq 3.3$	0.8

Table 3.7.: Comparison of fluxes measured in our mock spectra (second, third and fourth columns for models *RMN, RMO* and *RMP*, respectively) with the fluxes related to the centroid of M-L relation (last column) for $M_{500} = 6.9 \times 10^{14}\,\mathrm{M}_\odot$. We quote the fluxes in unit of $10^{-13}\,\mathrm{erg/s/cm^2}$.

We propose the following method to estimate the fluxes related to the M-L relation. We introduce a parameter $C_{bol,soft}$, which converts the X-ray bolometric luminosity ($L_{X,bol}$) into the soft-X luminosity (L_{soft-X}):

$$C_{bol,soft} := \frac{L_{soft-X}}{L_{X,bol}}. \tag{3.24}$$

In general, $C_{bol,soft}$ depends on the temperature of plasma that emits the observed radiation. We thus estimate $L_{X,bol}$ and L_{soft-X} using Xspec via the task LUM: in absence of any response matrix and of any absorption model, we model the emission of the ICM via the code APEC, where the spectroscopic temperature is T_{M-T} from *Eq.(3.23)* (for our spherical model of halo that has $M_{500} \simeq 6.9 \times 10^{14}\,\mathrm{M}_\odot$, $T_{M-T} \simeq 7.26\,\mathrm{keV}$), $Z = 0.3\,\mathrm{Z}_\odot$ and $z_{eff} = z_0 = 0.05$ (in APEC the broadening of the emission lines is only thermal). While, $C_{bol,soft}$ is independent of the assumed value of *norm*.
The emission of the ICM strongly varies with the radius of the cluster (see some examples in *Figures 3.2, 3.3, 3.4, 3.5, 3.6* and *3.7*). Indeed, the surface brightness profile usually is well reproduced by the isothermal β**-model** (*Cavaliere & Fusco-Femiano 1978*)

$$\Sigma_X(R_\bullet) = \frac{\Sigma_{X,0}}{\left[1 + \left(\frac{R_\bullet}{r_{scale}}\right)^2\right]^{3\beta-1/2}}, \tag{3.25}$$

where $R_\bullet := \sqrt{R^2 + z^2}$ is the radius in the plane of the sky (parallel to the meridional plane for an object seen edge-on), while r_{scale}, $\Sigma_{X,0}$ and β are the scale radius, the normalization and the slope parameter of β-model, respectively. *Mohr et al. (1999)* found good fits to the observed spherically averaged surface brightness profile in the outskirts of clusters for $\beta = 0.6$ and $r_{scale} = 0.15 r_{500}$.
The ratio between the emission in the entire cluster and that in the region under consideration is

$$R_{\mathcal{F}} := \frac{\iint_{Area} \Sigma_X(R_\bullet) dR dz}{2\pi \int_0^{r_{500}} \Sigma_X(R_\bullet) R_\bullet dR_\bullet}, \tag{3.26}$$

where $R_\bullet := \sqrt{R^2 + z^2}$, $\Sigma_X(R_\bullet)$ is given by *Eq.(3.25)* with $\beta = 0.6$ and $r_{scale} = 0.15 r_{500}$ (see above) and $Area = \pi \tilde{R}^2$ with $\tilde{R} = 70\,\mathrm{kpc}$ or $\tilde{R} = 100\,\mathrm{kpc}$ for *R1* or *R2*, respectively. Note that $R_{\mathcal{F}}$ is independent of $\Sigma_{X,0}$. To be consistent with the derivation of parameter *norm* (which

determines significantly the measured fluxes), we compute the numerator of *Eq.(3.26)* following the method to evaluate the outermost integral in *Eq.(3.13)* (note that *Area* in *Eq.(3.26)* is the same as in *(3.13)*).
The fluxes in the regions *R1* and *R2* derived from the M-L relation are estimated through

$$F^{M-L}_{soft-X} = C_{bol,soft} R_F \frac{L_{X,SR}}{4\pi D_L^2}, \tag{3.27}$$

where $L_{X,SR}$ is computed through *Eq.(3.21)* and D_L is the luminosity distance from the cluster at redshift $z_0 = 0.05$. In *Table 3.7* we report the fluxes estimated by using in *Eq.(3.21)* and in *Eq.(3.27)* the mass of spherical halo model presented in *Section 1.3* (*i.e.* $M_{500} \simeq 6.9 \times 10^{14}\,\mathrm{M}_\odot$).

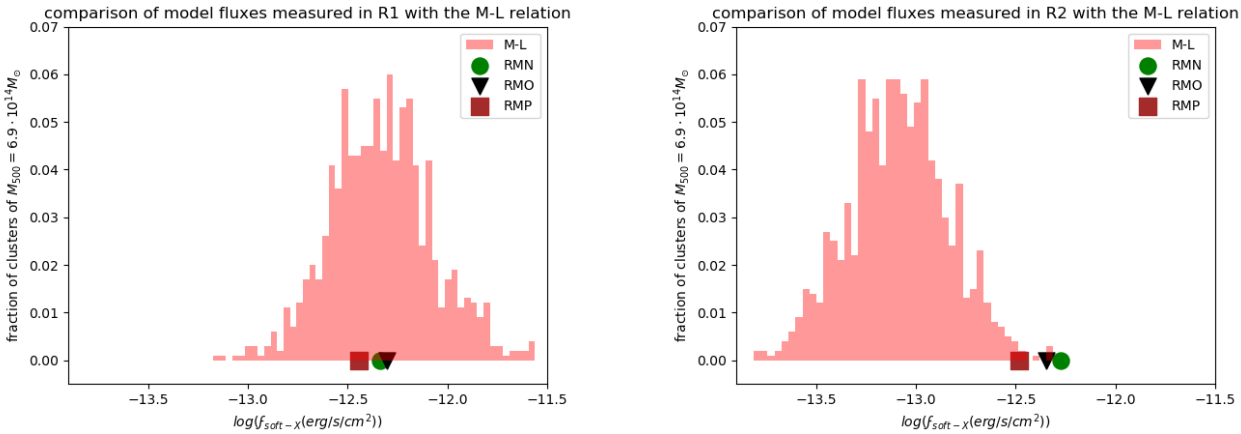

(a) (b)

Figure 3.11.: Comparison of the fluxes (listed in *Table 3.7*; circle, triangle and square), measured from our mock spectra in the regions *R1* (right panel) and *R2* (left panel), with the distributions (in red) of fluxes as expected from *Eq.s (3.27), (3.21)*and *(3.22)*.

In *Figure 3.11*, using *Eq.s (3.22)* and *(3.27)*, we mimic the distributions of F^{M-L}_{soft-X} in the regions *R1* and *R2* for 1000 clusters of $M_{500} = 6.9 \times 10^{14}\,\mathrm{M}_\odot$ and we compare them to the measurements of fluxes of our mock spectra in *Table 3.7*. Our fluxes closely match the relative distribution in the region *R1*, while this match is significantly lower in *R2*. We ascribe this difference to the use of a global temperature of the cluster (*i.e.* derived in the X-ray observations from the isothermal β-model) to estimate $C_{bol,soft}$: $T_{M-T} \simeq 7.26\,\mathrm{keV}$ differs significantly from the spectroscopic-like temperature of any model of the ICM in region *R2* (see *Table 3.3*). Nevertheless, in this work in *Eq.(3.21)* we use the "true" mass of halos and not the dynamical mass recovered under the assumption of hydrostatic equilibrium, which is smaller than the "true" mass in any rotating model.
On the basis of the comparison of our measured fluxes with the M-L relation, the mock X-ray spectra based on realistic intrinsic quantities of the ICM are fairly realistic: on one side it confirms the goodness of method used to reconstruct the mock spectra (see *Section 3.2.1*), on other side it reinforces the conclusions based on the spectral analyses in *Section 3.2.2*.

Chapter 4

Conclusions

In this work we propose, for different kinematic conditions of the ICM and for different shapes of halos in a typical cool-core cluster of $M_{500} \simeq 10^{15}\,\mathrm{M}_{\odot}$, six models of the ICM plus the DM, which respects the main predictions on the average internal structure of halos and the average observed thermodynamic behavior of the ICM. Then, comparing to the observations of real clusters we test in the X-rays the main photometric and spectroscopic signatures of our models (included the Doppler shift of the centroids of the emission lines via mock observations with the forthcoming X-ray spectrograph RESOLVE). In this Chapter we summarize the main results of this work and the future perspectives.

- We build, via a homeoidal expansion, exact flattened axisymmetric density-potential pairs. The models of DM halos based on these aspherical density-potential pairs (with ellipticities $\simeq 0.3$) respect for an opportune choice of scale radius and scale density the main predictions of DM-only simulations: the universal spherically averaged density profile and the mass-concentration relation (see *Chapter 1* and also *Appendix A* for a complete discussion of halo mass and the spherically averaged density profile of these aspherical models). These models of halos allow us to build realistic polytropic models of the ICM in cool-core clusters under different kinematic conditions of the plasma (see *Sections 2.2.3* and *2.3.3*).

- *Ghirardini et al. (2019)* construct the average observed profiles of the ICM throughout the cool-core cluster (from the center up to r_{200}). We demonstrate that within $\simeq r_{500}$ a two-component composite polytrope model captures both in the outer region and in the cool core the essential thermodynamic features of the average observed profiles of the ICM (see *Section 2.2.2*).

- We find for a given axisymmetric gravitational potential the analytic expression of *effective potential (2.36)* associated with *rotation law (2.34)* of *Bianconi et al. (2013)* (see *Section 2.3.2*). In this work, we show that the rotation patterns based on this rotation curve with peaks of azimuthal speed $\lesssim 500\,\mathrm{km/s}$ at $R \lesssim 400\,\mathrm{kpc}$ (see *Table 2.4* and *Figure 2.6a*) allow us to build realistic models of the ICM (see *Section 2.3.3*) under different assumptions of the shapes of halos (here, we note that the prolate halo model favour high rotation speeds of the ICM).

- We demonstrate that a model of a typical cool-core cluster of $M_{200} \simeq 10^{15}\,\mathrm{M}_{\odot}$ with a

polytropic distribution of the ICM can reproduce with a good agreement the universal profiles of the thermodynamic quantities of the ICM not only under the assumption of spherical symmetry and in absence of bulk motions, but also using halos of axial ratios $\simeq 0.7$ and/or in presence of rotation of $\lesssim 500\,\mathrm{km/s}$ (see *Sections 2.2.3* and *2.3.3*). At the same time, we provide, for different kinematic conditions of the plasma and different shapes of the halos, physical models of the ICM in a typical cool-cool clusters, which are expected to be representative of the population of relaxed cool-core clusters of $M_{200} \simeq 10^{15}\,\mathrm{M}_{\odot}$. These models of the ICM thus could be used for the interpretation of the future observations with the X-ray instruments on board of the observatories CHANDRA, XMM-NEWTON, XRISM and ATHENA and with the microwave instruments on PLANCK.

- We test the tightness of the following photometric constraints on the rotation patterns in relaxed clusters. The comparison with the universal profiles of the thermodynamic quantities of the ICM and their observed scatter is a useful tool to select the rotation law and its parameters (see *Section 2.3.3*), even if this test is currently limited to distributions of the ICM with low mass biases. It is a promising test for the near future, since ongoing observational campaigns aim to understand the relationship between the mass biases and the departure from the average observed profiles of *Ghirardini et al. (2019)* (*e.g.* CHEX-MATE Project; `http://xmm-heritage.oas.inaf.it/`). While, the difficulty to find an evident bimodality of the distribution of morphological parameters (in particular, of average axial ratio) of X-ray surface brightness between relaxed and disturbed clusters suggests that we are not able to constrain tightly the rotation patterns via the morphology of X-ray surface brightness for different shapes of halos (see *Section 3.1*). Indeed, our models of the ICM are widely consistent with the current upper limits on the average ellipticity of X-ray surface brightness (see *Section 3.1.2*). In this work, the indirect X-ray photometric observables are not very powerful tests for the rotation patterns and, consequently, the most promising probe for them is the Doppler shift and broadening of the centroids of the emission lines in high quality X-ray spectra.

- By convolving the data reconstructed with an exposure time of 100 ksec from our models of the ICM with the response matrices of RESOLVE, we present a collection of X-ray spectra representative of those observed in clusters of $M_{200} \simeq 10^{15}\,\mathrm{M}_{\odot}$ under different kinematic conditions of the ICM (see *Sections 3.2.1* and *3.2.3*). On the basis of the "best-fit" results of our spectral analyses, which in most cases closely match the input parameters (see *Section 3.2.2*), we demonstrate the chance to detect in a X-ray spectrum of either receding or approaching ICM the *l.o.s.* speed of $\gtrsim 250\,\mathrm{km/s}$ via the fitting Doppler shift of the centroids of the emission lines in presence of a non-thermal broadening of $\sigma_{broad} \lesssim 100\,\mathrm{km/s}$. However, since the introduction of turbulence damages significantly the spectral analyses, for $\sigma_{broad} \gtrsim 200\,\mathrm{km/s}$ this detection is possible only for *l.o.s.* speeds of $\gtrsim 300\,\mathrm{km/s}$ (see *Section 3.2.2*). This work strongly encourages future spectroscopic observations of relaxed galaxy clusters with RESOLVE and/or X-IFU (see also *Roncarelli et al. 2018*) to infer the *l.o.s.* speeds of the ICM from the shift of the centroids and from the broadening of the emission lines.

- In the near future, to conclude the study of these rotating models, we plan to compute their hydrostatic mass bias, following the method used by *Nipoti et al. (2015)*. A natural extension of this work explores smaller largest-to-smallest axial ratios of halos (as predicted by *Allgood et al. 2006*) and baroclinic distributions to reproduce the average observed profiles of *Ghirardini et al. (2019)*. In a future work focused on the detectability of gas rotation in multiwavelength observations, we could explore via mock observations

of the CMB signal, detectable at microwave wavelengths, the possibilities and limits to measure with a good significativity the distortion of the CMB spectrum induced by gas rotation from our models of cool-core clusters. Moreover, on the basis of the dispersion relation presented by *Nipoti & Posti (2013)* a future work could follow in presence of local perturbations the linear evolution of the ICM in our rotating models. According to *Nipoti et al. (2015)* in this regime we expect the presence of magnotorotational unstable modes, which could trigger an efficient turbulent heating in the non-linear regime and, consequently, contribute to halt the cooling flows in the cool cores of relaxed clusters.

In this work, we conclude that our models predict rotation of 400-500 km/s that do not violate the available observables in the X-rays (*i.e.* the average observed thermodynamic profiles and shape of iso-surface brightness contours), leaving some room in real clusters for possible rotation of $\lesssim 500$ km/s, which could be detected via the Doppler shift of the centroids of the X-ray emitting lines with the facilities on board of the observatories of new generation launched in the future (see also *Roncarelli et al. 2018* and *Bianconi et al. 2013*). The possibility that the rotation in real clusters is $\simeq 500$ km/s acquires a great interest not only to fully appreciate one of the phenomena which could shape the distribution of the ICM and regulate its energetic budget via magnotorotational instability, but also to control mass biases, which could affect the use of clusters as cosmological probes.

Appendix A

The equivalent mass: a useful concept of gravitational mass for aspherical clusters

When dealing with spherical halos, the gravitational field is a direct probe of the mass of a cluster (indeed, $M(< r) = r^2 g(r)/G$, where $g(r)$ is the intensity of the spherically symmetric gravitational field and r the spherical radius). If the predictions on the shape of halos based on the DM-only simulations are correct, the assumption of spherical symmetry usually exploited in the X-ray observations could cause overestimate or underestimate of the mass of aspherical clusters. When comparing a flattened halo model with the halo properties inferred from the X-ray observations, it is useful to introduce the concept of **equivalent mass**: the mass inferred from the average gravitational field of an aspherical halo under the assumption of spherical symmetry.
In this Appendix, it is interesting to quantify the difference between the "true" mass and the equivalent mass, essentially the mass bias introduced by the DM halo flattening, for the halo models in *Section 1.3*.

The equivalent mass of our flattened halo models. The equivalent mass of a halo within the sphere of radius r is

$$M_{eq}(< r) := \frac{r^2 g_{mean}(r)}{G}, \tag{A.1}$$

where $g_{mean}(r)$ is the intensity of the spherically averaged gravitational field. In this work we use two definitions of g_{mean} for spheroidal halo models:

$$g_{mean}(r) = \frac{2g_R(r;0) + g_z(0;r)}{3} \tag{A.2}$$

and

$$g_{mean}(r) = [g_R^2(r;0) g_z(0;r)]^{1/3}, \tag{A.3}$$

where g_R and g_z are the intensities of the R- and z- components of the gravitational field (in cylindrical coordinates), respectively. Note that for both definitions of g_{mean} $M_{eq}(< r)$ is the "true" mass of a spherically symmetric halo model, where $g_R(r;0) = g_z(0;r)$. In a generic spheroidal halo model there is a mismatch between $M_{eq}(< r)$ in *Eq.(A.1)* and $M(< r)$ in

Eq.(1.43), so we conclude that we cannot use $M(< r)$ when comparing to the results inferred under the assumption of spherical symmetry.
Using both definitions of g_{mean} in *Eq.s (A.2)* and *(A.3)*, the difference between $M(< r)$ in *Eq.(A.1)* and $M(< r)$ in *Eq.(1.43)* is negligible throughout the halo for each model in *Table 1.1.*

Departure of spherically averaged density profile of our flattened models from the spherical NFW profile. Here we use the notation of *Section 1.1.* In this work, to be as far as possible consistent with the predictions of DM-only simulations on the universal profile of halos, we assume the NFW as the zero-order term of homeoidal expansion (see *Chapter 1*). However, for a declining zero-order density distribution the directional subtraction of density imposes a departure of the spherically averaged density profile from the zero-order spherical term $\tilde{\rho}(\tilde{r})$. For the description of the spherically averaged density profile of aspherical NFW, given by the truncation of *Eq.(1.18)* to the first significant order in flattening ($\tilde{\rho}(\tilde{x};\tilde{y};\tilde{z})$), we use the analytic expression

$$\tilde{\rho}_{mean}(\tilde{r}) := \frac{\tilde{\rho}(\tilde{r};0;0)+\tilde{\rho}(0;\tilde{r};0)+\tilde{\rho}(0;0;\tilde{r})}{3} = \frac{1-(\epsilon+\eta)/3}{\tilde{r}(1+\tilde{r})^2} - \frac{2(\epsilon+\eta)}{3(1+\tilde{r})^3}. \tag{A.4}$$

We quantify the deviation of spherically averaged density profile of aspherical NFW from the spherical NFW by means of the ratio between the absolute value of two terms in RHS of *Eq.(A.4)*

$$D(\tilde{r}) = \frac{|-2/3(\eta+\epsilon)/(1+\tilde{r})^3|}{(1-(\eta+\epsilon)/3)/[\tilde{r}(1+\tilde{r})^2]} = \frac{2(\eta+\epsilon)}{3-(\eta+\epsilon)}\frac{\tilde{r}}{1+\tilde{r}}. \tag{A.5}$$

$D(\tilde{r})$, as well as the directional subtraction of mass, is significant only at $\tilde{r} \gg 1$ and for high η. For $\eta = 1/3$, when the subtraction of density occurs in the equatorial plane, $D(\tilde{r} \gg 1) \sim 4/7$ and, when along the symmetry axis, $D(\tilde{r} \gg 1) \sim 2/9$. Indeed, the request for a physical density (see *Section 1.2.2*) also provides $D(\tilde{r}) < 1$ everywhere.
Given that $D(\tilde{r})$ is a probe of the departure of our spheroidal halo models from the NFW profile, we conclude that it is significant only in the halo outskirts.

Bibliography

Allgood, B., Flores, R. A., Primack, J. R., et al. 2006, MNRAS, 367, 1781, doi: 10.1111/j.1365-2966.2006.10094.x

Altamura, E., Kay, S. T., Chluba, J., & Towler, I. 2023, arXiv e-prints, arXiv:2302.07936, doi: 10.48550/arXiv.2302.07936

Anders, E., & Grevesse, N. 1989, GCA, 53, 197, doi: 10.1016/0016-7037(89)90286-X

Arnaud, K. A. 1996, in Astronomical Society of the Pacific Conference Series, Vol. 101, Astronomical Data Analysis Software and Systems V, ed. G. H. Jacoby & J. Barnes, 17

Baldi, A. S., De Petris, M., Sembolini, F., et al. 2018, MNRAS, 479, 4028, doi: 10.1093/mnras/sty1722

Beers, T. C., Flynn, K., & Gebhardt, K. 1990, Aj, 100, 32, doi: 10.1086/115487

Bianconi, M., Ettori, S., & Nipoti, C. 2013, MNRAS, 434, 1565, doi: 10.1093/mnras/stt1112

Binney, J., Nipoti, C., & Fraternali, F. 2009, MNRAS, 397, 1804, doi: 10.1111/j.1365-2966.2009.15113.x

Bîrzan, L., McNamara, B. R., Nulsen, P. E. J., Carilli, C. L., & Wise, M. W. 2008, ApJ, 686, 859, doi: 10.1086/591416

Bruggen, M. 2013, Astronomische Nachrichten, 334, 543, doi: 10.1002/asna.201311895

Buote, D. A., & Canizares, C. R. 1992, ApJ, 400, 385, doi: 10.1086/172004

—. 1994, ApJ, 427, 86, doi: 10.1086/174123

Buote, D. A., & Tsai, J. C. 1995, ApJ, 452, 522, doi: 10.1086/176326

Campitiello, M. G., Ettori, S., Lovisari, L., & CHEX-MATE Collaboration. 2022, in European Physical Journal Web of Conferences, Vol. 257, European Physical Journal Web of Conferences, 00007, doi: 10.1051/epjconf/202225700007

Carilli, C. L., Perley, R. A., & Harris, D. E. 1994, MNRAS, 270, 173, doi: 10.1093/mnras/270.1.173

Cavaliere, A., & Fusco-Femiano, R. 1978, A&A, 70, 677

CHEX-MATE Collaboration, Arnaud, M., Ettori, S., et al. 2021, A&A, 650, A104, doi: 10.1051/0004-6361/202039632

Cimatti, A., Fraternali, F., & Nipoti, C. 2019, arXiv e-prints, arXiv:1912.06216, doi: 10.48550/arXiv.1912.06216

Ciotti, L., & Bertin, G. 2005, ApJ, 437, 419, doi: 10.1051/0004-6361:20042123

Cooray, A., & Chen, X. 2002, ApJ, 573, 43, doi: 10.1086/340582

Cui, W., Knebe, A., Yepes, G., et al. 2018, MNRAS, 480, 2898, doi: 10.1093/mnras/sty2111

Dutton, A. A., & Macciò, A. V. 2014, MNRAS, 441, 3359, doi: 10.1093/mnras/stu742

Eckert, D., Ettori, S., Pointecouteau, E., et al. 2017, Astronomische Nachrichten, 338, 293, doi: 10.1002/asna.201713345

Ettori, S., Donnarumma, A., Pointecouteau, E., et al. 2013, SSR, 177, 119, doi: 10.1007/s11214-013-9976-7

Ettori, S., Gastaldello, F., Leccardi, A., et al. 2010, Astronomy and Astrophysics, 524, A68, doi: 10.1051/0004-6361/201015271

Ettori, S., Lovisari, L., & Sereno, M. 2020, ApJ, 644, A111, doi: 10.1051/0004-6361/202038586

Fang, T., Humphrey, P., & Buote, D. 2009, ApJ, 691, 1648, doi: 10.1088/0004-637X/691/2/1648

Gaspari, M., Ruszkowski, M., & Sharma, P. 2012, ApJ, 746, 94, doi: 10.1088/0004-637X/746/1/94

Geller, M. J., & Beers, T. C. 1982, PASP, 94, 421, doi: 10.1086/131003

Ghirardini, V., Eckert, D., Ettori, S., et al. 2019, ApJ, 621, A41, doi: 10.1051/0004-6361/201833325

HI4PI Collaboration, Ben Bekhti, N., Flöer, L., et al. 2016, A&A, 594, A116, doi: 10.1051/0004-6361/201629178

Hitomi Collaboration, Aharonian, F., Akamatsu, H., et al. 2016, Nat, 535, 117, doi: 10.1038/nature18627

Hlavacek-Larrondo, J., Li, Y., & Churazov, E. 2022, arXiv e-prints, arXiv:2206.00098, doi: 10.48550/arXiv.2206.00098

Ho, I. T., Lim, J., & Dinh-V-Trung. 2009, ApJ, 698, 1191, doi: 10.1088/0004-637X/698/2/1191

Kaiser, N. 1986, MNRAS, 222, 323, doi: 10.1093/mnras/222.2.323

Kalinkov, M., Valchanov, T., Valtchanov, I., Kuneva, I., & Dissanska, M. 2005, MNRAS, 359, 1491, doi: 10.1111/j.1365-2966.2005.09008.x

Kravtsov, A. V., & Borgani, S. 2012, ARA&A, 50, 353, doi: 10.1146/annurev-astro-081811-125502

Lau, E. T., Kravtsov, A. V., & Nagai, D. 2009, ApJ, 705, 1129, doi: 10.1088/0004-637X/705/2/1129

Lau, E. T., Nagai, D., Kravtsov, A. V., & Zentner, A. R. 2011, ApJ, 734, 93, doi: 10.1088/0004-637X/734/2/93

Liu, A., & Tozzi, P. 2019, MNRAS, 485, 3909, doi: 10.1093/mnras/stz713

Mazzotta, P., Rasia, E., Moscardini, L., & Tormen, G. 2004, MNRAS, 354, 10, doi: 10.1111/j.1365-2966.2004.08167.x

McCourt, M., Parrish, I. J., Sharma, P., & Quataert, E. 2011, MNRAS, 413, 1295, doi: 10.1111/j.1365-2966.2011.18216.x

McCourt, M., Sharma, P., Quataert, E., & Parrish, I. J. 2012, MNRAS, 419, 3319, doi: 10.1111/j.1365-2966.2011.19972.x

McDonald, M., Veilleux, S., & Rupke, D. S. N. 2012, ApJ, 746, 153, doi: 10.1088/0004-637X/746/2/153

McDonald, M., Veilleux, S., Rupke, D. S. N., Mushotzky, R., & Reynolds, C. 2011, ApJ, 734, 95, doi: 10.1088/0004-637X/734/2/95

McDonald, M., Benson, B. A., Vikhlinin, A., et al. 2013, ApJ, 774, 23, doi: 10.1088/0004-637X/774/1/23

McNamara, B. R., & Nulsen, P. E. J. 2012, New Journal of Physics, 14, 055023, doi: 10.1088/1367-2630/14/5/055023

Meneghetti, M., Rasia, E., Merten, J., et al. 2010, Astronomy and Astrophysics, 514, A93, doi: 10.1051/0004-6361/200913222

Mohr, J. J., Mathiesen, B., & Evrard, A. E. 1999, ApJ, 517, 627, doi: 10.1086/307227

Mroczkowski, T., Nagai, D., Basu, K., et al. 2019, SSR, 215, 17, doi: 10.1007/s11214-019-0581-2

Nagai, D., Kravtsov, A. V., & Vikhlinin, A. 2007a, ApJ, 668, 1, doi: 10.1086/521328

Nagai, D., Lau, E. T., Avestruz, C., Nelson, K., & Rudd, D. H. 2013, ApJ, 777, 137, doi: 10.1088/0004-637X/777/2/137

Nagai, D., Vikhlinin, A., & Kravtsov, A. V. 2007b, ApJ, 655, 98, doi: 10.1086/509868

Navarro, J. F., Frenk, C. S., & White, S. D. M. 1996, ApJ, 462, 563, doi: 10.1086/177173

Nipoti, C., & Posti, L. 2013, MNRAS, 428, 815, doi: 10.1093/mnras/sts070

Nipoti, C., Posti, L., Ettori, S., & Bianconi, M. 2015, Journal of Plasma Physics, 81, 495810508, doi: 10.1017/S0022377815000781

O'Dea, C. P., Baum, S. A., Privon, G., et al. 2008, ApJ, 681, 1035, doi: 10.1086/588212

Planck Collaboration, Ade, P. A. R., Aghanim, N., et al. 2014, ApJ, 571, A29, doi: 10.1051/0004-6361/201321523

Pratt, G. W., Arnaud, M., Biviano, A., et al. 2019, SSR, 215, 25, doi: 10.1007/s11214-019-0591-0

Press, W. H., & Schechter, P. 1974, ApJ, 187, 425, doi: 10.1086/152650

Rafferty, D. A., McNamara, B. R., Nulsen, P. E. J., & Wise, M. W. 2006, ApJ, 652, 216, doi: 10.1086/507672

Rasia, E., Borgani, S., Murante, G., et al. 2015, ApJL, 813, L17, doi: 10.1088/2041-8205/813/1/L17

Rebusco, P., Churazov, E., Böhringer, H., & Forman, W. 2005, MNRAS, 359, 1041, doi: 10.1111/j.1365-2966.2005.08965.x

Reichert, A., Böhringer, H., Fassbender, R., & Mühlegger, M. 2011, ApJ, 535, A4, doi: 10.1051/0004-6361/201116861

Roncarelli, M., Gaspari, M., Ettori, S., et al. 2018, ApJ, 618, A39, doi: 10.1051/0004-6361/201833371

Sarazin, C. L., Burns, J. O., Roettiger, K., & McNamara, B. R. 1995, ApJ, 447, 559, doi: 10.1086/175899

Schuecker, P., Finoguenov, A., Miniati, F., Böhringer, H., & Briel, U. G. 2004, A&A, 426, 387, doi: 10.1051/0004-6361:20041039

Springel, V., & Farrar, G. R. 2007, MNRAS, 380, 911, doi: 10.1111/j.1365-2966.2007.12159.x

Sunyaev, R. A., Norman, M. L., & Bryan, G. L. 2003, Astronomy Letters, 29, 783, doi: 10.1134/1.1631411

Sunyaev, R. A., & Zeldovich, Y. B. 1972, Comments on Astrophysics and Space Physics, 4, 173

—. 1980, MNRAS, 190, 413, doi: 10.1093/mnras/190.3.413

Tassoul, J.-L. 1978, Theory of rotating stars

Towler, I., Kay, S. T., & Altamura, E. 2023, MNRAS, doi: 10.1093/mnras/stad453

Tozzi, P., & Norman, C. 2001, ApJ, 546, 63, doi: 10.1086/318237

Vazza, F., Jones, T. W., Brüggen, M., et al. 2017, MNRAS, 464, 210, doi: 10.1093/mnras/stw2351

Vikhlinin, A., Kravtsov, A., Forman, W., et al. 2006, ApJ, 640, 691, doi: 10.1086/500288

Voit, G. M. 2005, Reviews of Modern Physics, 77, 207, doi: 10.1103/RevModPhys.77.207

Zhuravleva, I., Chen, M. C., Churazov, E., et al. 2022, arXiv e-prints, arXiv:2210.11544. https://arxiv.org/abs/2210.11544

Zhuravleva, I., Churazov, E., Kravtsov, A., & Sunyaev, R. 2012, MNRAS, 422, 2712, doi: 10.1111/j.1365-2966.2012.20844.x